

# Lawrence Berkeley National Laboratory

## Recent Work

**Title**

Magnetic Metallic Multilayers

**Permalink**

<https://escholarship.org/uc/item/9h90g5rf>

**Author**

Hood, R.Q.

**Publication Date**

1994-04-01



# Lawrence Berkeley Laboratory

UNIVERSITY OF CALIFORNIA

## Materials Sciences Division

### Magnetic Metallic Multilayers

R.Q. Hood  
(Ph.D. Thesis)

April 1994



| LOAN COPY |  
| Circulates |  
| for 4 weeks |

Bldg. 50 Library.  
Copy 2

LBL-35491

## **DISCLAIMER**

This document was prepared as an account of work sponsored by the United States Government. While this document is believed to contain correct information, neither the United States Government nor any agency thereof, nor the Regents of the University of California, nor any of their employees, makes any warranty, express or implied, or assumes any legal responsibility for the accuracy, completeness, or usefulness of any information, apparatus, product, or process disclosed, or represents that its use would not infringe privately owned rights. Reference herein to any specific commercial product, process, or service by its trade name, trademark, manufacturer, or otherwise, does not necessarily constitute or imply its endorsement, recommendation, or favoring by the United States Government or any agency thereof, or the Regents of the University of California. The views and opinions of authors expressed herein do not necessarily state or reflect those of the United States Government or any agency thereof or the Regents of the University of California.

MAGNETIC METALLIC MULTILAYERS\*

Randolph Q. Hood

Department of Physics  
University of California  
Berkeley, CA 94720

and

Materials Sciences Division  
Lawrence Berkeley Laboratory  
University of California  
Berkeley, CA 94720

April 1994

---

\*This work was supported in part by the Director, Office of Energy Research, Office of Basic Energy Sciences, Materials Sciences Division of the U. S. Department of Energy under Contract No. DE-AC03-76SF00098.

# **Magnetic Metallic Multilayers**

Copyright © 1994

by

**Randolph Quentin Hood**

The U.S. Department of Energy has the right to use this thesis  
for any purpose whatsoever including the right to reproduce  
all or any part thereof

## Abstract

### Magnetic Metallic Multilayers

by

Randolph Quentin Hood

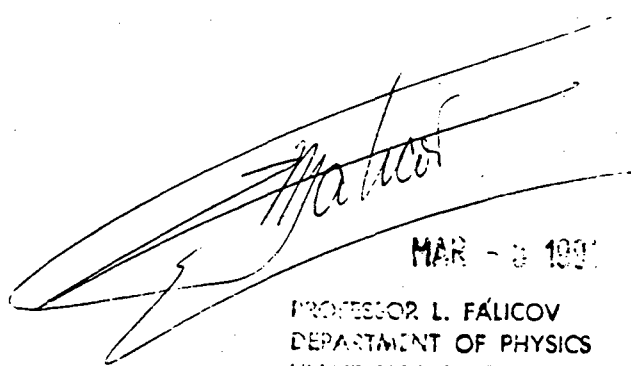
Doctor of Philosophy in Physics

University of California at Berkeley

Professor L. M. Falicov, Chair

Investigations of the magnetic and magnetoresistant properties of magnetic metallic multilayers are presented. Utilizing self-consistent Hartree-Fock calculations several aspects of multilayers and interfaces are explored: enhancement and reduction of the local magnetic moments, magnetic coupling at the interfaces, magnetic arrangements within each film and among non-neighboring films, the global symmetry of the systems, frustration, orientation of the various moments with respect to an outside applied field, and magnetic-field induced transitions. The various situations exhibit a rich structure and a wealth of possible magnetic effects. The magnetoresistance of ferromagnetic-normal-metal multilayers is found by solving the Boltzmann equation. The results explain the giant negative magnetoresistance encountered in these systems when an initial antiparallel arrangement is changed into a parallel configuration by application of an external magnetic field. The calculation depends on (1) geometric parameters (the thicknesses of the layers), (2) intrinsic metal parameters (number of conduction electrons, magnetization, and effective masses in the layers), (3) bulk sample properties (conductivity relaxation times), (4) interface scattering properties (diffuse scattering versus potential scattering at the interfaces, and (5) outer surface scattering properties (specular versus diffuse surface scattering). It is found that a

large negative magnetoresistance requires, in general, considerable asymmetry in the interface scattering for the two spin orientations. Specific features of the interfaces that may produce an asymmetrical spin-dependent scattering are studied: (1) varying interfacial geometric random roughness with no lateral coherence, (2) correlated (quasi-periodic) roughness, and (3) varying chemical composition of the interfaces. The interplay between these aspects of the interfaces may enhance or suppress the magnetoresistance, depending on whether it increases or decreases the asymmetry in the spin-dependent scattering of the conduction electrons.



MAR - 8 1991

PROFESSOR L. FALICOV  
DEPARTMENT OF PHYSICS  
UNIVERSITY OF CALIFORNIA  
BERKELEY, CALIFORNIA 94720

*This thesis is dedicated to my mother,  
Theresa M. Hood*



## Table of Contents

Dedication .....	ii
Table of Contents .....	iii
Acknowledgments .....	v
Chapter I: Introduction .....	1
A. Magnetic Properties .....	2
B. Magnetoresistance .....	3
C. References for Chapter I .....	9
D. Figures for Chapter I .....	12
Chapter II: Itinerant-Electron, One-Dimensional Magnetic Superlattices .....	15
A. Introduction .....	15
B. Model .....	15
C. Results and Discussion .....	18
D. Conclusions .....	24
E. References for Chapter II .....	26
F. Figures for Chapter II .....	27
Chapter III: Boltzmann Equation Approach to the Negative Magnetoresistance of Ferromagnetic-Normal Metallic Multilayers .....	47
A. Introduction .....	47
B. Model .....	48
C. Results .....	55
D. Discussion and Conclusions .....	58
E. References for Chapter III .....	64

F. Figures for Chapter III .....	iv
F. Figures for Chapter III .....	67
Chapter IV: Effects of Interfacial Roughness on the Magnetoresistance of Magnetic Metallic Multilayers .....	82
A. Introduction .....	82
B. Interface Parameters .....	84
C. Results .....	87
D. Conclusions .....	92
E. References for Chapter IV .....	94
F. Figures for Chapter IV .....	97

## Acknowledgments

I want to express my most sincere gratitude to my thesis advisor, Professor Leo Falicov, for his guidance, encouragement and friendship.

I had the good fortune of interacting with Dr. David Penn, for which I am grateful, while working on a portion of this thesis.

I have benefited greatly from many stimulating discussions with members of the Falicov group. It is a pleasure to acknowledge Antônio da Silva, Dr. James Freericks, Dr. Amitesh Maiti, Sadi Turgut, Dr. Andreas Gieseckus, Dr. Emilio Artacho, Dr. Henrik Svensmark, Dr. François Willaime, Dr. Wolfgang Hübner, Jose Menchero, Vijay Iyer, Dr. Leonor Chico, and Dr. Chumin Wang Chen.

To all members, past and present, of the Condensed Matter Theory Group I extend my appreciation for making these years thoroughly enjoyable.

## Chapter I: Introduction

Artificially fabricated structures provide new frontiers for the exploration of physical effects. The availability and control of additional degrees of freedom allow for the isolation and study of specific physical phenomena and the creation of new devices. One class of man-made materials, magnetic metallic multilayers, have burst into prominence recently with the discovery of an oscillatory interlayer coupling<sup>1</sup> and a giant magnetoresistance<sup>2</sup> in these systems.

Magnetic metallic multilayers consist of alternating thin films of two or more chemical compositions, at least one of which is magnetic. In 1902 Maurain<sup>3</sup> fabricated perhaps the first such multilayer when he electrodeposited a layer of copper and then a layer of iron on a magnetized iron cathode. He found that for sufficiently thin copper layers the magnetization of the iron film had a tendency of aligning in the same direction as that of the cathode. However only within the last decade, with improvements in growth and characterization techniques that have become widely available, has a systematic study of well controlled multilayers been undertaken.<sup>4,5</sup>

A variety of different elements have been combined in the fabrication of magnetic metallic multilayers. They may be grown by sputtering, in which case they are polycrystalline, or epitaxially, in which case they are single crystals. This thesis concentrates on those multilayers composed of transition-metal elements and their associated alloys in which the thicknesses of the individual layers vary from single monolayers to thicknesses of about a hundred angstrom. In this chapter the reader is introduced to the subject of magnetic metallic multilayers through a discussion of the magnetic (static) and magnetoresistant (dynamic) properties of these systems. Experimental observations and the theoretical techniques utilized in understanding these properties are presented.

## A. Magnetic Properties

In the transition-metal elements making up the magnetic multilayers, the outer  $s$  and  $d$  electrons largely determine the electronic and magnetic properties. As individual transition-metal atoms are brought together and form a solid,  $d$  electron orbitals overlap forming itinerant Bloch states that partially hybridize with the  $s$  electrons. The magnetization seen in solids that are ferromagnetic (FM) (*e.g.* Fe, Co, and Ni) or anti-ferromagnetic (AFM) (*e.g.* Cr) are mainly caused by the electrons in the  $d$ -like bands. The itinerant nature of the  $d$ -like electrons confers upon the magnetization a sensitive dependence on the composition and structure of the local environment.<sup>6</sup>

The ordered alternating-compositional structure of magnetic multilayers provide bulk systems with tunable environments different from those experienced in simple elemental solids. When two neighboring magnetic layers are in contact, short-range exchange interactions are large and couple the magnetic moments near the interfaces. If there is a thin non-magnetic layer (spacer layer) separating the magnetic layers, the induced polarization of the electrons in the non-magnetic layer can produce a coupling of the magnetic moments between the magnetic layers. A large magnitude coupling that oscillates in sign with increasing thickness of the spacer layer is observed in carefully grown magnetic multilayers composed of alternating FM layers, such as Fe or Co, separated by a number of different transition-metal non-magnetic spacer layers with thicknesses between ten and a hundred angstrom.<sup>1,7</sup>

In general when long- and short- range interactions of comparable magnitude are present, a rich variety of magnetic structures are possible. Perhaps the simplest model that can capture this richness of structures is a suitably generalized Hubbard model. In the Hubbard model<sup>8</sup> both the itinerant nature of the narrow band  $d$ -like electrons and the dominant contribution from the Coulomb interaction -- the repulsion that two electrons experience when they occupy the same site -- are included. In the one-band Hubbard model the Hamiltonian has the form

$$H = \sum_{ij\sigma} t_{ij} c_{i\sigma}^\dagger c_{j\sigma} + U \sum_i c_{i\uparrow}^\dagger c_{i\uparrow} c_{i\downarrow}^\dagger c_{i\downarrow} \quad ,$$

where  $t_{ij}$  is the intersite hopping,  $U$  is the intrasite Coulomb repulsion, and  $c_{i\sigma}^\dagger$  ( $c_{i\sigma}$ ) are the creation (destruction) operators in a Wannier state of spin  $\sigma$  at site  $i$ . By varying the ratio of  $U$  to the bandwidth and the density of valence electrons  $n$ , a phase diagram of the low energy states consisting of paramagnetic, FM, and AFM solutions can be obtained in the Hartree-Fock approximation.<sup>9</sup> Despite the approximations made in this approach, the phase diagram provides a semiquantitative explanation of the observed distribution of magnetism in the transition metals. Thus by choosing different values of the ratio of  $U$  to the bandwidth and  $n$  in different layers, multilayers composed of various combinations of magnetic and non-magnetic transition metals can be simulated.

In chapter II the Hubbard model is generalized and applied to magnetic multilayers consisting of alternating layers composed of two types of materials, including FM, AFM, and paramagnetic layers.<sup>10</sup> The ground state magnetization is calculated both in the presence and in the absence of an external magnetic field. A wealth of magnetic arrangements and magnetic transitions are discovered and discussed.

## B. Magnetoresistance

Many different magnetic metallic multilayers consisting of alternating FM metals separated by non-magnetic metallic layers display a change in the electrical resistivity as the relative orientation of the magnetic moments in the individual FM layers varies. Since these variations in orientation are induced by an external magnetic field, the change in resistance is termed a magnetoresistance (MR). When the magnetic moments in the different FM layers are arranged in an antiparallel configuration the resistance drops under the application of a magnetic field that aligns the magnetic moments in the FM layers. This negative MR has been observed in various sandwiches<sup>11-17</sup> and superlattices,<sup>1,2,18-20</sup> such as NiFe/Cu/NiFe, NiFe/Ag/NiFe,  $(\text{Fe/Cr})_n$ ,  $(\text{Co/Cu})_n$ ,  $(\text{Fe/Cu})_n$ , and  $(\text{Co/Ru})_n$  to name just a few. In some cases the MR is large,<sup>2,18</sup> as in  $(\text{Fe/Cr})_n$  and  $(\text{Co/Cu})_n$ . Currently<sup>18</sup> the largest MR observed at

room temperature is in the  $(\text{Co/Cu})_n$  multilayer where the MR defined as  $\Delta\rho/\rho = [R(0) - R(H_{sat})]/R(H_{sat})$ , is as large as 65 % for a saturating field  $H_{sat}$  as small as 10 kOe (see Fig. 1). Systems with a MR larger than 20 % are said to exhibit a giant magnetoresistance (GMR) and could be very useful for applications in microelectronic devices.

The phenomenon of MR is well known in non-layered bulk metals. When a magnetic field is applied to a normal (*i.e.*, not magnetic) metal, the resistance increases regardless of the orientation of the field with respect to the current or with respect to the crystallographic axes. Increases in the resistance of many orders (a factor of a million is not uncommon) can be seen in particularly pure, single crystalline samples at liquid helium temperatures for applied fields of 100 kOe. At room temperature for similarly large fields increases of a factor of ten can be observed in polycrystalline samples.<sup>21</sup> This positive MR can be understood by noting that the presence of a magnetic field produces electron trajectories that are convoluted or helical in nature. So the net distance an electron can transport its charge before being scattered decreases as the intensity of the magnetic field increases.

In bulk FM metals the phenomenon of negative MR is observed. In high quality crystalline type FM metals at liquid-helium temperatures decreases in the resistivity as large as an order of magnitude can be seen<sup>22</sup> for applied fields as small as a 100 Oe. This drop in resistance is related to the change of the magnetic domain structure of the material induced by the external magnetic field; the material goes from a multi-domain structure to a single domain. As a result the magnetic field experienced by the electrons becomes more uniform, deconvoluting the electron trajectories. In addition the removal of Bloch walls eliminates a source of electron scattering.<sup>23</sup> Both effects result in longer mean-free paths upon the application of a magnetic field.

From an applications standpoint the MR observed in the magnetic multilayers is of greater interest than the MR found in bulk metals. Large magnetoresistances have been found in magnetic multilayers at room temperature for low fields (less than a

100 Oe) in samples which have high resistivities (greater than  $20 \mu\text{ohm-cm}$ ). In bulk magnetic and non-magnetic metals with large MR all of these conditions, which are important for applications, have not yet been met.

The negative MR in the magnetic multilayers has a different physical origin from MR observed in bulk homogeneous materials. A simple picture of the negative MR in the multilayers can be discussed (Fig. 2) by assuming the electrical current is carried in parallel separately by the spin-up and spin-down electrons. With this assumption the total resistivity  $\rho(H)$  takes the form

$$\frac{1}{\rho(H)} = \frac{1}{\rho_{\uparrow}} + \frac{1}{\rho_{\downarrow}},$$

where  $\rho_{\uparrow}$  and  $\rho_{\downarrow}$  are the resistivities associated with the spin-up and spin-down electrons. It should be noted that when magnetic moments in the different FM layers are aligned either parallel or antiparallel to each other then the spin-up and spin-down electrons throughout the entire multilayer can be associated with either the majority or the minority spin electrons in a given individual FM layer depending on its direction of magnetization. When the magnetic moments of the different FM layers are in an antiparallel configuration (Fig. 2(a)) both the spin-up and spin-down electrons are alternatively weakly and strongly scattered as they pass through the different layers; so  $\rho_{\uparrow} = \rho_{\downarrow}$ , and the total resistivity satisfies  $\rho(H=0) = (\rho_{\uparrow} + \rho_{\downarrow})/4$ , where  $\sigma$  is either  $\uparrow$  or  $\downarrow$ . The scattering environments experienced by the spin-up and spin-down electrons are generally different when the magnetic moments of the FM layers are aligned parallel to each other (Fig. 2(b)). If the resistivity associated with one spin component is much larger than the other, e.g.  $\rho_{\downarrow} \gg \rho_{\uparrow}$ , then  $\rho(H=H_{sat}) \approx \rho_{\uparrow}$ . If in addition  $\rho_{\sigma}$  for the antiparallel configuration is much larger than  $\rho_{\uparrow}$ , the smaller value of the spin-component resistivities in the parallel configuration, then  $\rho(H=H_{sat}) \ll \rho(H=0)$  and there is a GMR. This is termed the short circuit effect. The diamagnetic contributions associated with the helical trajectories that electrons follow in the presence of a magnetic field makes a much smaller contribution to the



MR in the magnetic multilayers in comparison to this spin-dependent short-circuit effect.

Spin-flip scattering alters the above picture of the short circuit effect. It is important to distinguish between the concepts of spin-flip scattering and spin-dependent scattering. The first refers to an event in which, during scattering, an electron reverses its spin orientation. The second one refers to the fact that electrons with different spin orientations experience different potentials and have different phase-space distributions. The main source of spin-flip scattering is caused by spin waves, *i.e.*, magnons.<sup>24</sup> As the temperature goes to 0 K spin mixing caused by magnons vanishes, but a residual spin-mixing associated with spin-orbit coupling remains. In 3d transition metals where spin-orbit coupling is small, spin-flip scattering cross sections are estimated as being 100 times smaller than non spin-flip scattering cross sections.<sup>25,26</sup> Therefore in magnetic multilayers composed of 3d transition metals at low temperatures spin-flip scattering is negligible in comparison to non spin-flip scattering, so the current can be thought of as being carried separately by spin-up and spin-down electrons.

The spin-dependent scattering which produces  $\rho_{\uparrow} \neq \rho_{\downarrow}$  in the magnetic multilayers can originate from either within the bulk of the layers or from the interfaces. The presence of impurities or imperfections within the layers are a source of scattering. The fabricated multilayers are far from perfect, exhibiting resistivities between 20 and 80  $\mu$  ohm-cm. Within the FM layers the different density of states for the spin-up (majority) or the spin-down (minority) electrons result in spin-dependent mean free paths. At the interfaces the presence of roughness (variations in layer thickness) is a source of scattering. Experiments by Fullerton *et al.*<sup>27</sup> indicate that increased interfacial roughness in  $(\text{Fe/Cr})_n$  enhances the GMR. Interdiffusion or mixing at the interfaces results in a alloy-like region near the interfaces. Parkin<sup>28</sup> found that the addition of thin Co layers at the interfaces of NiFe-Cu multilayers enhanced the MR. The MR increased monotonically as the Co layer increased to 4 angstrom, then became

insensitive to the thickness of the Co layer with a MR similar to that of  $(\text{Co/Cu})_n$ , despite the presence of NiFe layers sandwiched between the thin Co layers. Baumgart *et al.*<sup>29</sup> have found that ultrathin layers of elements (V, Mn, Ge, Ir, and Al) deposited at the Fe-Cr interface lead to changes in the MR, which correlate with the ratio of spin-up and spin-down resistivities arising from spin-dependent impurity scattering of these elements when alloyed with Fe. This result is in agreement with the suggestion of Baibich *et al.*<sup>2</sup> that the spin dependence of impurity scattering at the interfaces is related to that observed<sup>30</sup> in alloyed ferromagnetic metals such as Ni, Fe, and Co.

Theoretical considerations indicate in many magnetic multilayer systems the nature of the scattering at the interfaces has a greater effect on the MR than the scattering within the bulk of the layers. By fitting MR data of epitaxially grown Fe(001)/Cr(001) multilayers to model-calculation results, Levy *et al.*<sup>31</sup> concluded that the ratio of the interfacial resistivity to bulk resistivity is 0.83. Further confirmation of the importance of the interface in the MR effect was provided by Barthélémy *et al.*<sup>32</sup> who point out that the experimental data they obtained for epitaxially grown Fe(001)/Cr(001) multilayers seem to be in agreement with the variation of the MR with

$$\exp(-t_{Cr}/\lambda^*) \quad ,$$

where  $t_{Cr}$  is the thickness of Cr layer and  $\lambda^*$  is a length of the order of the mean free path. Such a variation of the MR with layer thickness is expected from spin-dependent interface scattering. In contrast with this, if spin-dependent scattering occurred within the Fe layers, a variation of the form

$$\exp[-(t_{Fe} + 2t_{Cr})/\lambda^*]$$

would be expected. Barnaś *et al.*<sup>33</sup> compared experimental data with their theoretical model, based on the Boltzmann transport equation with spin-dependent bulk and interface scattering, and concluded that the experimental data favor the interface contribution as being the dominant one.

Since interfacial scattering plays a significant role in the MR of many different ferromagnetic-normal-metal multilayers, a realistic description of such scattering is important. In chapters III and IV interfacial scattering is treated with increasing levels of sophistication. In chapter III the inclusion of coherent spin-dependent scattering, caused by the variation in the spin-dependent phase space that electrons experience as they traverse an interface, is studied. This scatters electrons into well defined directions, which can be described using angle-dependent reflection and transmission coefficients. The scattering caused by roughness and impurities at the interfaces is treated in an averaged way -- by diffusely scattering a portion of the electrons into the equilibrium direction. It is found that a large negative MR requires, in general, considerable asymmetry in the interface scattering for the two spin orientations.<sup>34</sup> In chapter IV the scattering associated with roughness and impurities is no longer treated in only an averaged way. The influence on the MR caused by scattering by interfaces with the following characteristics is considered: (1) varying interfacial geometric roughness with no lateral coherence, (2) correlated (quasiperiodic) roughness, and (3) varying chemical composition.<sup>35</sup> The interplay between these three aspects of the interfaces may enhance or suppress the MR, depending on whether it increases or decreases the asymmetry in the spin-dependent scattering of the conduction electrons.

In these studies the MR is found by calculating the in-plane spin-dependent resistivities  $\rho_G$  for the parallel and the antiparallel configurations of the FM layers. This is done by solving the Boltzmann equation in the relaxation-time approximation for ferromagnetic-normal-metal multilayers composed of 3d transition metals at low temperatures. In addition to depending on the nature of the interfaces, the parameters that are varied in the calculation include: (a) geometric parameters (the thickness of the layers), (b) intrinsic metal parameters (number of conduction electrons, magnetization, and effective masses in the layers), (c) bulk sample properties (conductivity relaxation times), and (e) outer surface scattering properties (specular *versus* diffuse scattering) for multilayer systems consisting of only a few layers.

## C. References for Chapter I

- <sup>1</sup> S. S. P. Parkin, N. More, and K. P. Roche, *Phys. Rev. Lett.* **64**, 2304 (1990).
- <sup>2</sup> M. N. Baibich, J. M. Broto, A. Fert, F. Nguyen Van Dau, F. Petroff, P. Etienne, G. Creuzet, A. Friederich, and J. Chazelas, *Phys. Rev. Lett.* **61**, 2472 (1988).
- <sup>3</sup> C. Maurain, *J. Phys. (Paris)* **1**, 90 (1902).
- <sup>4</sup> *Growth, Characterization, and Properties of Ultrathin Magnetic Films and Multilayers, Spring 1989*, edited by B. T. Jonker, J. P. Heremans, E. E. Marinero, Materials Research Symposia Proceeding, Vol. 151 (Materials Research Society, Pittsburgh, 1989).
- <sup>5</sup> *Magnetic Ultrathin Films: Multilayers and Surfaces Interfaces and Characterization, Spring 1993*, edited by B. T. Jonker, S. A. Chambers, R. F. C. Farrow, C. Chappert, R. Clarke, W. J. M. de Jonge, T. Egami, P. Grünberg, K. M. Krishnan, E. E. Marinero, C. Rau, and S. Tsunashima, Materials Research Symposia Proceedings, Vol. 313 (Materials Research Society, San Francisco, 1993).
- <sup>6</sup> L. M. Falicov, R. H. Victora, and J. Tersoff, in *The Structure of Surfaces*, edited by M. A. Van Hove and S. Y. Tong (Springer-Verlag, Berlin-Heidelberg-New York-Tokyo, 1985), p.12, and references therein.
- <sup>7</sup> S. S. P. Parkin, *Phys. Rev. Lett.* **67**, 3598 (1991).
- <sup>8</sup> J. Hubbard, *Proc. Roy. Soc.* **A276**, 238 (1963).
- <sup>9</sup> D. R. Penn, *Phys. Rev.* **142**, 350 (1966).
- <sup>10</sup> R. Q. Hood and L. M. Falicov, *Phys. Rev. B* **44**, 9989 (1991).
- <sup>11</sup> G. Binasch, P. Grünberg, F. Saurenbach, and W. Zinn, *Phys. Rev. B* **39**, 4828 (1989).
- <sup>12</sup> B. Dieny, V. S. Speriosu, S. S. P. Parkin, B. A. Gurney, D. R. Wilhoit, and D. Mauri, *Phys. Rev. B* **43**, 1297 (1991).

- 13 A. Chaiken, P. Lubitz, J. J. Krebs, G. A. Prinz, and M. Z. Harford, *J. Appl. Phys.* **70**, 5864 (1991).
- 14 B. Dieny, V. S. Speriosu, S. Metin, S. S. P. Parkin, B. A. Gurney, P. Baumgart, and D. R. Wilhoit, *J. Appl. Phys.* **69**, 4774 (1991).
- 15 A. Chaiken, T. M. Tritt, D. J. Gillespie, J. J. Krebs, P. Lubitz, M. Z. Harford, and G. A. Prinz, *J. Appl. Phys.* **69**, 4798 (1991).
- 16 A. Chaiken, G. A. Prinz, and J. J. Krebs, *J. Appl. Phys.* **67**, 4892 (1990).
- 17 T. Miyazaki, T. Yaoi, and S. Ishio, *J. Mag. Mag. Mat.* **98**, L7 (1991).
- 18 S. S. P. Parkin, Z. G. Li, and D. J. Smith, *Appl. Phys. Lett.* **58**, 2710 (1991).
- 19 F. Petroff, A. Barthélémy, D. H. Mosca, D. K. Lottis, A. Fert, P. A. Schroeder, W. P. Pratt Jr., and R. Loloee, *Phys. Rev. B* **44**, 5355 (1991).
- 20 W. P. Pratt, Jr., S. F. Lee, J. M. Slaughter, R. Loloee, P. A. Schroeder, and J. Bass, *Phys. Rev. Lett.* **66**, 3060 (1991).
- 21 See for instance J. M. Ziman, *Electrons and Phonons* (Oxford University Press, London, 1960), p. 490.
- 22 G. R. Taylor, A. Isin, and R. V. Coleman, *Phys. Rev.* **165**, 621 (1968); R. V. Coleman, R. C. Morris, and D. J. Sellmyer, *Phys. Rev. B* **8**, 317 (1973); R. W. Klaffky and R. V. Coleman, *Phys. Rev. B* **10**, 4803 (1974).
- 23 G. G. Cabrera and L. M. Falicov, *Phys. Status Solidi B* **61**, 539 (1974); *ibid.*, **62**, 217 (1974); G. G. Cabrera and L. M. Falicov, *Phys. Rev. B* **11**, 2651 (1975).
- 24 A. Fert, *J. Phys. C: Solid St. Phys.* **2**, 1784 (1969).
- 25 A. Fert and I. A. Campbell, *J. Phys. F: Metal Phys.* **6**, 849 (1976).
- 26 P. Monod, PhD Thesis (Orsay 1968).
- 27 E. E. Fullerton, D. M. Kelly, J. Guimpel, I. K. Schuller, and Y. Bruynseraede, *Phys. Rev. Lett.* **68**, 859 (1992).

- 28 S. S. P. Parkin, Phys. Rev. Lett. **71**, 1641 (1993).
- 29 P. Baumgart, B. A. Gurney, D. R. Wilhoit, T. Nguyen, B. Dieny, and V. Speriosu, J. Appl. Phys. **69**, 4792 (1991).
- 30 I. A. Campbell and A. Fert, in *Ferromagnetic Materials*, edited by E. P. Wohlfarth (North-Holland, Amsterdam, 1982), Vol. 3, p. 769.
- 31 P. M. Levy, S. Zhang, A. Fert, Phys. Rev. Lett. **65**, 1643 (1990).
- 32 A. Barthélémy, A. Fert, M. N. Baibich, S. Hadjoudj, F. Petroff, P. Etienne, R. Cabanel, S. Lequien, F. Nguyen Van Dau, and G. Creuzet, J. Appl. Phys. **67**, 5908 (1990).
- 33 J. Barnaś, A. Fuss, R. E. Camley, P. Grünberg, and W. Zinn, Phys. Rev. B **42**, 8110 (1990).
- 34 R. Q. Hood and L. M. Falicov, Phys. Rev. B **46**, 8287 (1992).
- 35 R. Q. Hood, L. M. Falicov, and D. R. Penn, Phys. Rev. B **49**, 368 (1994).

## D. Figures for Chapter I

### Figure 1

Experimental plots of the MR,  $[R(H) - R(H_{sat})]/R(H_{sat})$ , versus magnetic field ( $H$ ) at room temperature when the electrical current is in the plane of the layers for (Co/Cu) multilayers having different buffer and cover layers: (1) solid curve is for SiFe(50 Å)[8 Å Co/8.3 Å Cu]<sub>60</sub>Fe(25 Å) (2) dashed curve is for SiRu(50 Å)[8 Å Co/8.3 Å Cu]<sub>60</sub>Ru(25 Å). (Data from S. S. P. Parkin)

### Figure 2

Representative electron trajectories in a ferromagnetic-normal-metal multilayer for a spin  $\uparrow$  and a spin  $\downarrow$  electron when the magnetic moments are in (a) an antiparallel configuration and (b) a parallel configuration.

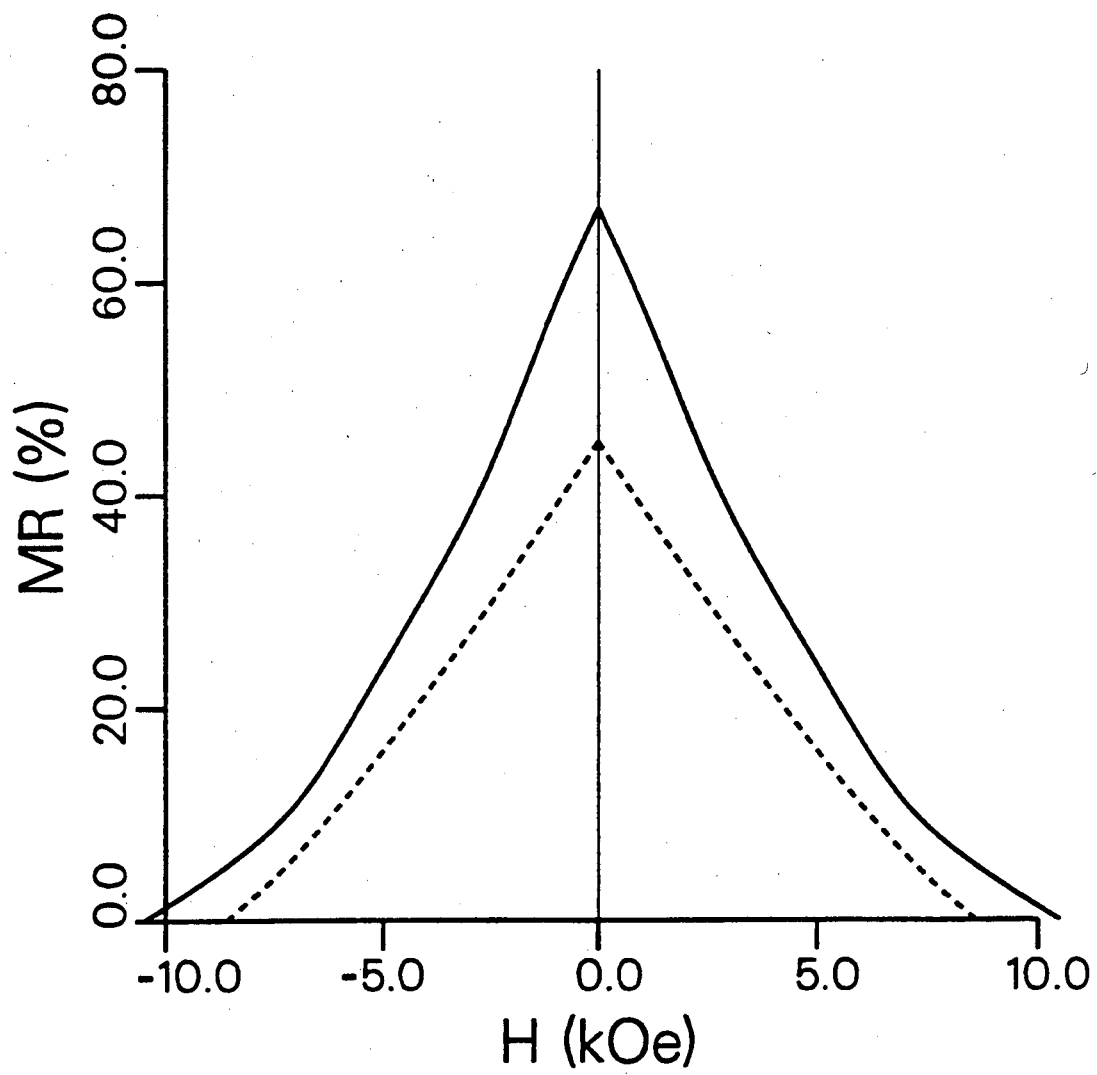
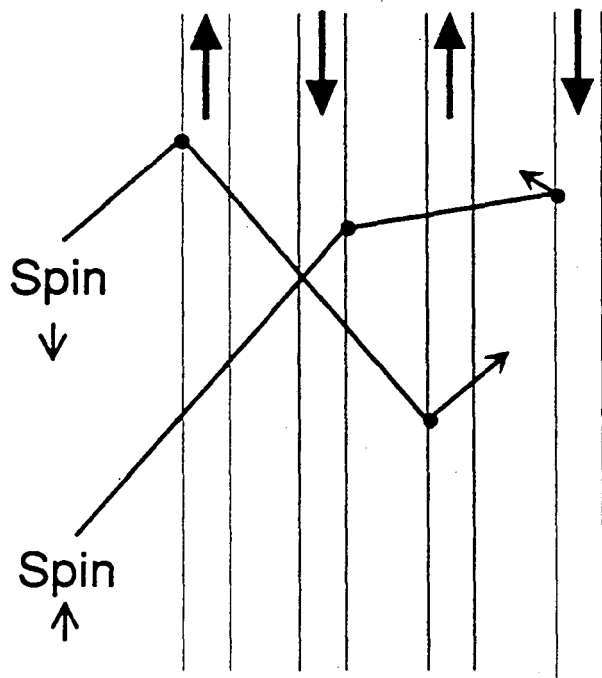


Fig. 1





(a)

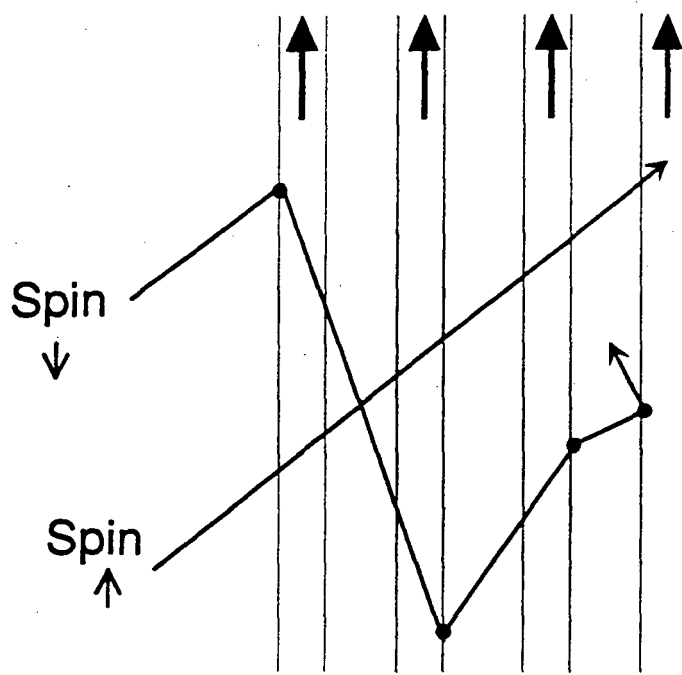


Fig. 2

(b)

## Chapter II: Itinerant-Electron, One-Dimensional Magnetic Superlattices

### A. Introduction

In this chapter I present one of the simplest models which has enough richness to describe many of the properties of magnetic multilayers composed of materials with itinerant-electrons in narrow bands. The model is an extension of that used by Penn<sup>1</sup> to describe the magnetic properties of transition elements and alloys. The model<sup>2</sup> is essentially a Hartree-Fock approximation to the one-band Hubbard model applied to one-dimensional superlattices. Computations were performed with unit cells (chains) composed of 16, 17, 18, and 19 sites consisting of alternating combinations of two types of materials, including FM, AFM, and paramagnetic (PM) layers. Periodic boundary conditions were imposed on the chains, so the multilayers become superlattices. The spatial variation of the magnetization and the total energy of the ground state were calculated for various values of an externally imposed uniform magnetic field. Magnetic-field induced phase transitions (at  $T = 0$ ) were observed to occur in some superlattices. Calculations were also performed in systems with frustration, in order to understand how it influences the magnetization in a superlattice.

While the model chosen is extremely simple, its structure does contain important features that describe a large variety of itinerant-electron magnetic superlattices. Understanding the complex structures of a simple model is necessary before more complex and realistic models can be considered. In section B the model is briefly described. In section C the results of the computations are presented and discussed.

### B. Model

The model chosen to represent multilayer systems consisting of transition-metal elements or alloys is the one-dimensional nearest-neighbor one-band Hubbard model in the presence of a magnetic field

$$\begin{aligned}
H = \sum_{i,\sigma} t_{i,i+1} (c_{i\sigma}^\dagger c_{i+1\sigma} + c_{i+1\sigma}^\dagger c_{i\sigma}) + \sum_i U_i c_{i\uparrow}^\dagger c_{i\uparrow} c_{i\downarrow}^\dagger c_{i\downarrow} \\
+ h \sum_i (c_{i\uparrow}^\dagger c_{i\uparrow} - c_{i\downarrow}^\dagger c_{i\downarrow}) \quad , \quad (1)
\end{aligned}$$

where the uniform magnetic field  $h$  (in energy units) is along the  $z$ -axis, and  $c_{i\sigma}^\dagger$  ( $c_{i\sigma}$ ) is the creation (annihilation) operator for an electron of spin  $\sigma$  in the state located at the  $i$ th site. For all sites within a particular layer  $U_i$  take the same value. Separate layers in general have different values of  $U_i$ . The hopping parameter  $t_{i,i+1}$  is set equal to  $-t$  (the unit of energy of the calculation) for hopping between nearest-neighbor sites within each layer and between different layers. The Hamiltonian is treated in the Hartree-Fock approximation:

$$\begin{aligned}
H_{HF} = -t \sum_{i,\sigma} (c_{i+1\sigma}^\dagger c_{i\sigma} + c_{i\sigma}^\dagger c_{i+1\sigma}) \\
+ \sum_{i,\sigma} U_i \left[ \langle c_{i\sigma}^\dagger c_{i\sigma} \rangle c_{i\bar{\sigma}}^\dagger c_{i\bar{\sigma}} - \langle c_{i\sigma}^\dagger c_{i\bar{\sigma}} \rangle c_{i\bar{\sigma}}^\dagger c_{i\sigma} \right] \\
+ \frac{1}{2} \sum_{i,\sigma} U_i \left[ \langle c_{i\sigma}^\dagger c_{i\bar{\sigma}} \rangle \langle c_{i\bar{\sigma}}^\dagger c_{i\sigma} \rangle - \langle c_{i\sigma}^\dagger c_{i\sigma} \rangle \langle c_{i\bar{\sigma}}^\dagger c_{i\bar{\sigma}} \rangle \right] \\
+ h \sum_i (c_{i\uparrow}^\dagger c_{i\uparrow} - c_{i\downarrow}^\dagger c_{i\downarrow}) \quad , \quad (2)
\end{aligned}$$

where  $\bar{\sigma}$  indicates the spin orientation opposite to  $\sigma$ . With trial wave functions similar to those used by Penn<sup>1</sup>, a ground-state phase diagram for a single layer as a function of the parameters  $x \equiv (U/t)$  and  $n$ , the number of electrons per site, was determined. Energies of FM, PM, and AFM states were compared. The phase diagram is shown in Fig. 1. By choosing various  $x_i = U_i/t$  and electron occupancies  $n_i \equiv \sum_{\sigma} \langle c_{i\sigma}^\dagger c_{i\sigma} \rangle$  for each site  $i$  in each structure, a variety of multilayer magnetic systems can be modeled.

The Hubbard Hamiltonian contains no long-range Coulomb interaction, and is therefore susceptible to large charge fluctuations, which are energetically very unfavorable in real situations. In the approach taken here such fluctuations are completely suppressed by not allowing the existence of charge excess or defects at any

site. The parameters  $n_i$  are thus constant for each species; this is accomplished by adding to  $H_{HF}$  on-site chemical potentials  $\mu_i$  for each site  $i$  so that the resulting Hamiltonian operator

$$H' = H_{HF} - \sum_i \mu_i (c_{i\uparrow}^\dagger c_{i\uparrow} + c_{i\downarrow}^\dagger c_{i\downarrow}) \quad (3)$$

exhibits a ground state with the predetermined  $n_i$ . This treatment involves a self-consistent loop needed to determine the chemical potentials  $\mu_i$ .

Calculations were performed for different multilayers with two species, *i.e.*, the parameters  $x_i$  and  $n_i$  took, throughout the sample, only two different values. The multilayer samples consist of  $N$  sites with periodic boundary conditions, so that the  $(N + i)$  site is considered identical to the  $i$  site for every site  $i$ . Each sample contained two or four layers of thickness  $L_\alpha$ , such that

$$N = \sum_\alpha L_\alpha \quad ,$$

and such that in each  $\alpha$  layer there are sites of only one species. With a given strength of the field  $h$ , the total energy of the ground state and the corresponding expectation values

$$\langle c_{i\sigma}^\dagger c_{i\sigma} \rangle \quad i=1, \dots, N \quad \sigma, \sigma' = \uparrow, \downarrow$$

were determined selfconsistently, subject to the constraints

$$\langle c_{i\uparrow}^\dagger c_{i\uparrow} \rangle + \langle c_{i\downarrow}^\dagger c_{i\downarrow} \rangle = n_i \quad ; \quad (4)$$

the total value and orientation of the magnetic moment at each site could thus be calculated

$$M_i = \sum_{\sigma, \sigma'} \langle i\sigma | \hat{x} \sigma_x + \hat{y} \sigma_y + \hat{z} \sigma_z | i\sigma' \rangle \langle c_{i\sigma}^\dagger c_{i\sigma} \rangle \quad , \quad (5)$$

where  $\sigma_x$ ,  $\sigma_y$  and  $\sigma_z$  are the Pauli matrices:

$$\sigma_x = \begin{bmatrix} 0 & 1 \\ 1 & 0 \end{bmatrix} \quad \sigma_y = \begin{bmatrix} 0 & -i \\ i & 0 \end{bmatrix} \quad \sigma_z = \begin{bmatrix} 1 & 0 \\ 0 & -1 \end{bmatrix}$$

All calculations were performed for  $M_y = 0$ , *i.e.*, all  $\langle c_{i\sigma}^\dagger c_{i\bar{\sigma}} \rangle$  were taken to be real.

### C. Results and Discussion

In all calculations the superlattices were composed of two materials in alternating layers chosen from the following:

- (1) a fully saturated FM state with  $x = 6$  and  $n = \frac{1}{4}$  ;
- (2) an (insulating in the bulk) AFM state with  $x = 6$  and  $n = 1$  ;
- (3) a PM state with  $x = 1$  and  $n = \frac{1}{4}$  , denoted by PM1;
- (4) another PM state with  $x = 1$  and  $n = \frac{1}{3}$  , denoted by PM2;
- (5) a third PM state with  $x = 1$  and  $n = \frac{3}{4}$  , denoted by PM3.

The intersite hopping element  $t$  between adjacent sites was taken to be constant (the unit of energy of the calculation), either between identical or between different species.

The above parameters correspond to no specific element. In the bulk the fully saturated FM has  $|M_i| = 0.25$  at each site  $i$ . The bulk AFM state has partially developed magnetic moments,  $|M_i| = 0.89$ , with fixed but arbitrary orientation, and which alternate in sign between consecutive sites. An exact solution of the one-dimensional Hubbard model<sup>3</sup> yields an insulating AFM ground state for half filling, which is in agreement with the Hartree-Fock solution for  $x = 6$  and  $n = 1$ .

Fourteen different superlattices are reported here. The ground state of each, in the limit as  $h \rightarrow 0^+$ , is shown in Figs. 2 through 15. The direction of the infinitesimal magnetic field pointing in the  $z$ -direction is indicated by the small arrow located in the center of the Figs. 2 through 15. An axis indicating the  $x$  and  $z$  directions is included explicitly in Fig. 2. The orientation of the axis is the same in Figs. 3 through 15 as in Fig. 2. The local magnetic moment (5) at each site is represented by a vector. The sites are arranged in a ring to display more clearly the periodic boundary conditions.

Of the fourteen cases here displayed, eight cases consist of periods of two alternating layers with two interfaces present (Figs. 2, 5-8, and 11-13), while the other six cases have periods with four layers and four interfaces present. The results have many distinctive features that should be noted.

**(1) Magnitude of the magnetic moments.**

The magnitude of the magnetic moments, *i.e.* the values of  $|M_i|$  at each site  $i$ , fall within a range of values for each species. These are:

(1a) For the FM layers  $0.19 \leq |M_i| \leq 0.25$  .

(1b) For the AFM layers  $0.84 \leq |M_i| \leq 0.89$  .

(1c) For the various PM layers  $0.06 \leq |M_i| \leq 0.25$  for PM1,  $0.02 \leq |M_i| \leq 0.33$  for PM2, and  $0.05 \leq |M_i| \leq 0.33$  for PM3; it should be noted that for PM3, as opposed to PM1 and PM2, the sites are always polarized, but never fully polarized, *i.e.*, the maximum value attained is 0.33, as opposed to a possible maximum value of 0.75.

**(2) Magnetic coupling at the interfaces.**

The coupling of the magnetic moments at the interfaces tended to produce either parallel (ferromagnetic) or antiparallel (antiferromagnetic) couplings, never magnetic moments at an angle to each other. The structures, however, because of frustration or outside constraints (see below), exhibit some interfaces with magnetic moments at an angle (see for instance Figs. 3, 13 and 15). In particular:

(2a) All FM/PM interfaces exhibit an induced magnetic moment at the PM sites which align themselves ferromagnetically with respect to (parallel to) the FM moment (see Fig. 2).

(2b) In all AFM/PM interfaces the induced magnetic moment in the PM sites aligns itself antiferromagnetically with respect to the moment of the last AFM site (see Fig. 8).

(2c) A similar antiferromagnetic heterogeneous coupling appears in all FM/AFM interfaces (see Figs. 11-15).

### **(3) Magnetic arrangements within a single layer.**

The FM or AFM couplings of the uniform samples tend to be preserved in the corresponding layers. However, boundary conditions and external constraints modify the behavior in each case.

(3a) Whenever the magnetic moment in the FM is depressed at an interface (typically  $\approx 10\text{--}20\%$  smaller than the bulk value), it tends to recover its bulk value exponentially further inside the layer, with a healing length  $\approx 0.3$  sites (see Figs. 2-4, and 11-15).

(3b) Similarly the magnetic moment at the interface of an AFM layer decreases by  $\approx 1\text{--}6\%$  and recovers its bulk values exponentially with a healing length  $\approx 1.3$  sites.

(3c) In superlattices which contain PM layers, their polarization depends on whether there is a net magnetization present in the other layers, on the effective coupling between magnetic moments at the interfaces (see above), and on the form of the PM susceptibility  $\chi(\mathbf{q})$ ; in the AFM/PM superlattices shown here (Figs. 5-10) a spin-density wave occurs in all PM layers with more than four sites; in the FM/PM superlattices (Figs. 2-4), spin-density waves were found in PM layers consisting of any number of sites.

### **(4) Relative orientation of non-neighboring layers.**

The relative orientation of two well separated layers is of great technological interest, mainly in the case of FM layers.

(4a) Whenever possible, *i.e.*, for small enough fields and whenever the boundary conditions allow it, two consecutive FM layers separated by PM layers tend to align themselves antiparallel to one another (see Figs. 2-4).

(4b) The coupling of FM layers in FM/AFM superlattices is dominated (in the case considered here for which the AFM state is much more stable and much more magnetic than the FM state) by the thickness of the AFM layer; FM layers tend to align themselves parallel to each other if the number of sites in the intervening AFM layer is odd, and antiparallel to each other if that number is even. For a half-filled band, the case considered here for the AFM, the Fermi wave vector is half the distance to the Brillouin zone boundary, and therefore the Fermi-surface induced oscillations (referred to as RKKY oscillations)<sup>4</sup> have a period of two lattice sites, in agreement with the results.

(4c) External constraints and frustration (see below) may change this behavior.

**(5) Global symmetry of the ground-state arrangements.**

All cases shown here (Figs. 2 through 15) exhibit a symmetry line, placed always vertically in the drawings. These symmetry lines are of two types

(5a) Mirror-image sites have identical spin orientations (Figs. 3 and 12).

(5b) Mirror-image sites have magnetic moments that have identical components along the  $z$  axis, but components of identical magnitude and opposite sign along the  $x$  axis (Figs. 2, 4-10, and 13-15).

(5c) In the case in which all spins have  $z$ -axis-only orientation both (5a) and (5b) apply (Fig. 11).

(5d) Figs. 9, 10, and 14 show also an additional (horizontal) line of symmetry, of type (5a).

(5e) Fig. 3 shows also an additional (horizontal) line of symmetry, but of type (5b).

(5f) Finally, Figs. 3, 9, 10, and 14, all four-layer superlattices, can be thought of as composed by two two-layer cells, related to each other by a half-period translation followed by inversion of the  $x$  component of the spin (which is complete spin-inversion in Figs. 9 and 10).



## (6) Frustration.

Although frustration -- incompatible demands on the spin arrangement -- is common in two- and three-dimensional problems, it is never present in *infinite* one-dimensional systems. In one dimension it is always possible to arrange spins in a sequential manner (from left to right, say) and thus avoid incompatible demands. In more realistic three-dimensional models of superlattices, frustration may occur at FM/AFM interfaces because of different possible arrangements of lattice sites, *e.g.*, the presence of triangular arrangements and/or incompatible AFM couplings. It is therefore important to understand how magnetization changes are caused by frustration.

It is possible in one-dimensional situations to obtain frustration conditions artificially by imposing periodic boundary conditions with a period that is not compatible with the physical characteristics of the system. Such an artificially imposed frustrated situation in general disappears with a doubling of the unit cell, in which successive segments are allowed to take different *i.e.*, not identical configurations. In the cases reported here there are five such artificially (periodic-boundary-condition imposed) frustrated situations: those shown in Figs. 2, 6, 7, 13 and 15.

The system of Fig. 2 is frustrated because the induced spin-density wave in the PM is not compatible with a uniform orientation of the FM segments. Evidence of this effect is given in the unfrustrated situation of Fig. 3.

The systems of Fig. 6 and 7 are frustrated because the natural periods of the AFM and the induced spin-density wave in the PM are not compatible within a single combined period. When this incompatibility is removed (Figs. 5, 8, 9 and 10) the frustration disappears.

The system shown in Fig. 13 can be viewed as a distortion of the system shown in Fig. 11 in which a single site from the AFM layer is removed. The presence of only two layers, the even number of AFM sites and the periodic boundary conditions result in a frustrated situation. As a consequence the magnetic moments in the FM

layer are at an angle to each other, resulting, in the full period of the FM-AFM superlattice, in an extra spin rotation of  $180^\circ$ , which compensates for the extra AFM sites. A large part of the  $180^\circ$  net twist occurs at the FM/AFM interface with approximately  $23.7^\circ$  at each interface. A net twist of  $90.6^\circ$  occurs in the FM layer while only  $42.0^\circ$  within the AFM layer. It is interesting to note that the magnitude of the magnetic moments change -- between Fig. 11 and Fig. 13 -- by less than 1%.

In the system shown in Fig. 15 as in the system shown in Fig. 13 the frustration results in a net  $180^\circ$  twist among the relative orientation of the spins from an unfrustrated configuration that would be present if anti-periodic boundary conditions (a doubling of the unit cell) had been imposed instead, with less than a 1% change in the magnitude of the magnetic moments.

The energetics of interfaces and frustration can be estimated from the various calculations: the total energies are  $-6.411 t$  for the case of Fig. 11,  $-6.061 t$  for the case of Fig. 13,  $-6.006 t$  for the case of Fig. 14,  $-6.302 t$  for the case of Fig. 15, and  $-2.950 t$  for a period 8 (four AFM, four FM; not shown) structure. Simple algebra yields an energy of

$-0.296 t$  for the addition of an extra unfrustrated AFM atom;

$0.041 t$  for each AFM/FM interface;

$0.027 t$  for a single  $180^\circ$  "frustration twist" distributed over 16/17 sites;

$0.053 t$  for a single  $180^\circ$  "frustration twist" distributed over 8 sites.

#### **(7) Orientation with respect to the outside field.**

The ground state configuration of each superlattice considered was invariant under a uniform rotation of all magnetic moments simultaneously. When performing the calculations, the limit  $h \rightarrow 0^+$  was taken to give the ground state a preferred orientation. For ground states with no net magnetization it was found that the individual magnetic moments lined up in the direction perpendicular to the infinitesimal magnetic field (Figs. 5, 8-10, 12, and 14): it is well known that for antiferromagnetic

structures, *i.e.*, structures with no net magnetic moment, it is energetically more favorable to orient the individual spins in a direction *perpendicular* to that of the infinitesimal applied magnetic field.<sup>5</sup>

For structures with a net magnetic moment (Figs. 2-4, 6, 7, 11, 13 and 15), the moment aligns itself, as expected, in the  $-z$  (favorable) direction of the infinitesimal field  $h$ .

#### (8) Magnetic-field-induced transitions.

All systems presented here were found to undergo, for high enough magnetic fields, a transition into a final phase in which all local magnetic moments are pointing in the  $-z$  direction and are fully saturated. This occurred for fields  $h > h_f$ , large enough so that the Zeeman energy,  $M_z h$ , becomes the dominant term in the Hamiltonian. In addition to this final transition, the symmetry present in some systems (Fig. 11, and the artificially frustrated cases of Figs. 6, 7, and 15) guarantees that an earlier phase transition at  $h = h_c$  to a state of different symmetry takes place. This transition occurs in systems where at least one site is *on* a mirror axis of symmetry 5b, with its magnetic moment vector oriented along the unfavorable  $+z$  direction. Since for very large fields the final orientation is along the (favorable)  $-z$  axis, either a discontinuous transition takes place, or a state of intermediate broken symmetry appears. In all cases examined here the latter case applies, and the values of  $h_c$  are indicated in the corresponding figure captions. Two possible (mirror-image) broken-symmetry situations, with identical energies, appear.

#### D. Conclusions

The one-dimensional problem of heterogeneous periodic structures made from itinerant magnets examined here shows a wealth of magnetic arrangements and transitions unexpected from such a simple system. The basic mechanisms are relatively easy to understand, but the variety and multiplicity of possible effects are a continuous source of surprises and unexpected results. The effects in real three-dimensional

structures are probably even more complex, and the possibilities of new arrangements, unexpected physical effects, and probable new practical applications make this field a rich one to explore, both experimentally and theoretically.

**E. References for Chapter II**

- <sup>1</sup> D. R. Penn, Phys. Rev. **142**, 350 (1966).
- <sup>2</sup> R. Q. Hood and L. M. Falicov, Phys. Rev. B **44**, 9989 (1991).
- <sup>3</sup> E. H. Lieb and F. Y. Wu, Phys. Rev. Lett. **20**, 1445 (1968).
- <sup>4</sup> RKKY is an acronym for Ruderman, Kittel, Kasuya, and Yosida; the four people who first discussed this physical effect. For a discussion see C. Kittel, *Solid State Physics, Volume 22*, edited by F. Seitz, D. Turnbull, and H. Ehrenreich (Academic Press, New York, 1968), p. 1.
- <sup>5</sup> See for instance R. M. White, *Quantum Theory of Magnetism* (McGraw-Hill, New York, 1970), p.101.

## F. Figures for Chapter II

### Figure 1

The bulk phase diagram for the one-dimensional model as a function of the number of electrons per site  $n$  and the relative strength  $x$  of the Coulomb repulsion with respect to the band hopping parameter. Only paramagnetic (PM), ferromagnetic (FM), and antiferromagnetic (AFM) states were included. The AFM state has a periodicity of two lattice sites. In the region marked PM only that state exists. In the regions marked FM and AFM the corresponding states are stable with respect to the PM state. In region 1 the PM state is stable and the FM state is metastable. In region 2 the AFM state is stable and the FM state is metastable. In region 3 the FM state is stable and the AFM state is metastable.

### Figure 2

Ground-state configuration of a multilayer structure of period 18 consisting of two layers: 12 FM atoms and 6 PM2 atoms. The FM atoms are indicated by dashed circles and the PM atoms by full circles. There is a net magnetic moment for the complete period of 0.78 electron-spins in the  $z$ -direction of the (infinitesimal) magnetic field. Note the mirror global symmetry (type 5b) along the vertical axis. This configuration is frustrated because of the periodic boundary conditions. Recall that the magnetization in the  $y$  direction at each site  $i$  is zero.

### Figure 3

Ground-state configuration of a multilayer structure of period 18 consisting of four layers: 6 FM atoms, 3 PM2 atoms, another 6 FM atoms, and another 3 PM2 atoms. The FM atoms are indicated by dashed circles and the PM atoms by full circles. There is a net magnetic moment for the complete period of 0.74 electron-spins in the direction of the (infinitesimal) magnetic field. Note that mirror-image sites along the vertical axis have identical magnetic moments (5a-type symmetry) whereas mirror-image sites along the horizontal axis have the  $x$ -component of the magnetic-moment vector reversed (5b-type symmetry).

**Figure 4**

Ground-state configuration of a multilayer structure of period 18 consisting of four layers: 6 FM atoms, 4 PM2 atoms, another 6 FM atoms, and another 2 PM2 atoms. The FM atoms are indicated by dashed circles and the PM atoms by full circles. There is a net magnetic moment for the complete period of 0.71 electron-spins in the direction of the (infinitesimal) magnetic field. Note the mirror global symmetry (type 5b) along the vertical axis.

**Figure 5**

Ground-state configuration of a multilayer structure of period 16 consisting of two layers: 8 AFM atoms and 8 PM1 atoms. The AFM atoms are indicated by dot dashed circles and the PM atoms by full circles. There is no net magnetic moment in this structure. Note the mirror global symmetry (type 5b) along the vertical axis.

**Figure 6**

Ground-state configuration of a multilayer structure of period 17 consisting of two layers: 11 AFM atoms and 6 PM2 atoms. The AFM atoms are indicated by dot dashed circles and the PM atoms by full circles. There is a net magnetic moment for the complete period of 0.21 electron-spins in the direction of the (infinitesimal) magnetic field. This configuration is frustrated because of the periodic boundary conditions. Note the mirror global symmetry (type 5b) along the vertical axis. Notice also that, although the magnetic moment of the whole structure is oriented along the  $-z$  (favorable) direction, the AFM site at the top of the structure, which is *on* the symmetry axis, is oriented in the  $+z$  (unfavorable) direction: this feature guarantees a symmetry-breaking transition at a finite magnetic field  $h_c = 0.045 t$ .

**Figure 7**

Ground-state configuration of a multilayer structure of period 19 consisting of two layers: 11 AFM atoms and 8 PM3 atoms. The AFM atoms are indicated by dot dashed circles and the PM atoms by full circles. There is a net magnetic moment for

the complete period of 0.29 electron-spins in the direction of the (infinitesimal) magnetic field. This configuration is frustrated because of the periodic boundary conditions. Note the mirror global symmetry (type 5b) along the vertical axis. Notice also that, although the magnetic moment of the whole structure is oriented along the  $-z$  (favorable) direction, the AFM site at the top of the structure, which is *on* the symmetry axis, is oriented in the  $+z$  (unfavorable) direction: this feature guarantees a symmetry-breaking transition at a finite magnetic field  $h_c = 0.047 t$ .

### Figure 8

Ground-state configuration of a multilayer structure of period 18 consisting of two layers: 12 AFM atoms and 6 PM2 atoms. The AFM atoms are indicated by dot dashed circles and the PM atoms by full circles. There is no net magnetic moment in this structure. Note the mirror global symmetry (type 5b) along the vertical axis.

### Figure 9

Ground-state configuration of a multilayer structure of period 18 consisting of four layers: 6 AFM atoms, 3 PM2 atoms, another 6 AFM atoms, and another 3 PM2 atoms. The AFM atoms are indicated by dot dashed circles and the PM atoms by full circles. There is no net magnetic moment in this structure. Note that mirror-image sites along the horizontal axis have identical magnetic moments (5a-type symmetry) whereas mirror-image sites along the vertical axis have the  $x$ -component of the magnetic-moment vector reversed (5b-type symmetry).

### Figure 10

Ground-state configuration of a multilayer structure of period 16 consisting of four layers: 4 AFM atoms, 4 PM1 atoms, another 4 AFM atoms, and another 4 PM1 atoms. The AFM atoms are indicated by dot dashed circles and the PM atoms by full circles. There is no net magnetic moment in this structure. Note that mirror-image sites along the horizontal axis have identical magnetic moments (5a-type symmetry) whereas mirror-image sites along the vertical axis have the  $x$ -component of the magnetic-moment vector reversed (5b-type symmetry).



**Figure 11**

Ground-state configuration of a multilayer structure of period 17 consisting of two layers: 8 FM atoms and 9 AFM atoms. The FM atoms are indicated by dashed circles and the AFM atoms by dot dashed circles. There is a net magnetic moment for the complete period of 1.00 electron-spins in the direction of the (infinitesimal) magnetic field. Note the mirror global double symmetry (types 5a and 5b) along the vertical axis. Notice also that, although the magnetic moment of the whole structure is oriented along the  $-z$  (favorable) direction, the AFM site at the top of the structure, which is *on* the symmetry axis, is oriented in the  $+z$  (unfavorable) direction: this feature guarantees a symmetry-breaking transition at a finite magnetic field  $h_c = 0.022t$ .

**Figure 12**

Ground-state configuration of a multilayer structure of period 17 consisting of two layers: 4 FM atoms and 13 AFM atoms. The FM atoms are indicated by dashed circles and the AFM atoms by dot dashed circles. There is, fortuitously, no net magnetic moment in this structure.

**Figure 13**

Ground-state configuration of a multilayer structure of period 16 consisting of two layers: 8 FM atoms and 8 AFM atoms. The FM atoms are indicated by dashed circles and the AFM atoms by dot dashed circles. There is a net magnetic moment for the complete period of 1.20 electron-spins in the direction of the (infinitesimal) magnetic field. This configuration is frustrated because of the periodic boundary conditions. Note the mirror global symmetry (type 5b) along the vertical axis.

**Figure 14**

Ground-state configuration of a multilayer structure of period 16 consisting of four layers: 4 FM atoms, 4 AFM atoms, another 4 FM atoms, and another 4 AFM atoms. The FM atoms are indicated by dashed circles and the AFM atoms by dot dashed

circles. There is no net magnetic moment in this structure. Note that mirror-image sites along the horizontal axis have identical magnetic moments (5a-type symmetry) whereas mirror-image sites along the vertical axis have the  $x$ -component of the magnetic-moment vector reversed (5b-type symmetry).

### Figure 15

Ground-state configuration of a multilayer structure of period 17 consisting of four layers: 4 FM atoms, 4 AFM atoms, another 4 FM atoms, and another 5 AFM atoms. The FM atoms are indicated by dashed circles and the AFM atoms by dot dashed circles. There is a net magnetic moment for the complete period of 0.17 electron-spins, with a component of 0.17 electron-spins in the direction of the (infinitesimal) magnetic field, and 0.02 electron-spins in the perpendicular direction. This configuration is frustrated because of the periodic boundary conditions. Note the mirror global symmetry (type 5b) along the vertical axis. Notice that this structure has a well defined chirality; the structure with  $M_x$  inverted in each site is, of course, degenerate with it. Notice also that, although the magnetic moment of the whole structure is oriented along the  $-z$  (favorable) direction, the AFM site at the top of the structure, which is *on* the symmetry axis, is oriented in the  $+z$  (unfavorable) direction: this feature guarantees a symmetry-breaking transition at a finite magnetic field  $h_c = 0.020 t$ .

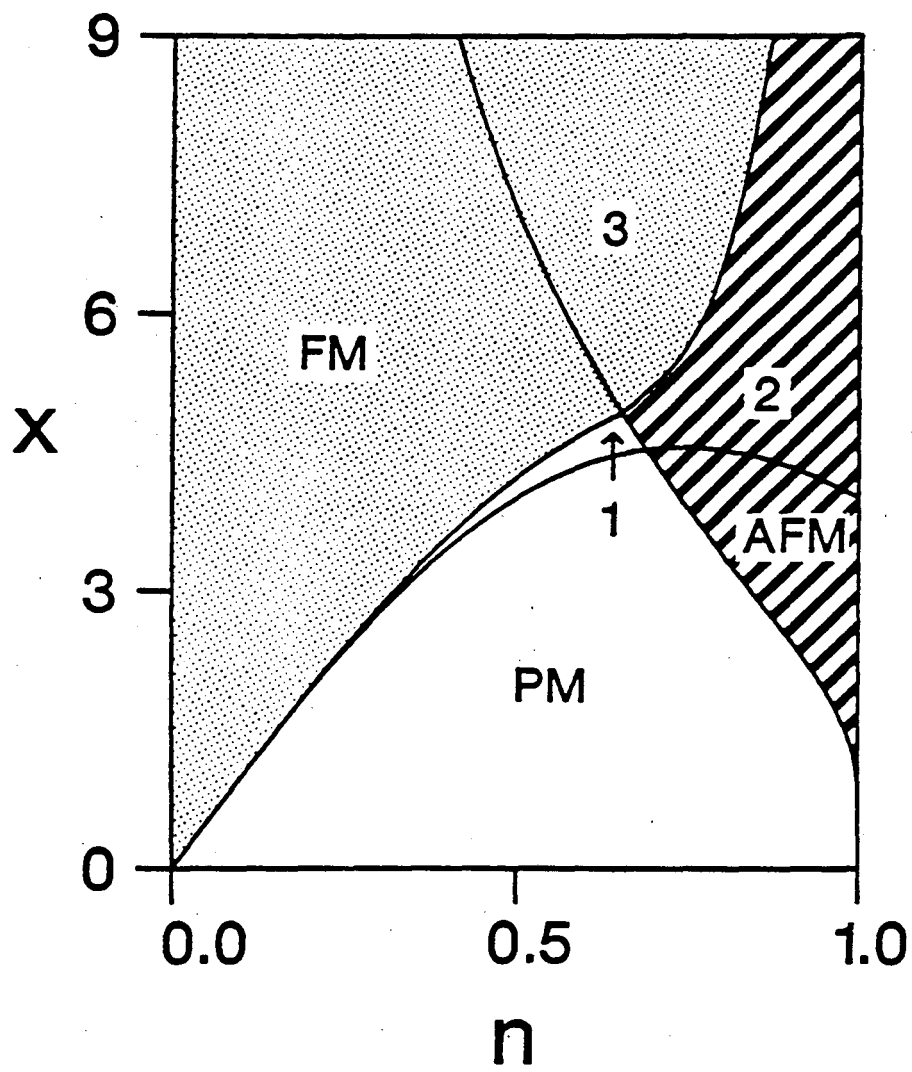


Fig. 1

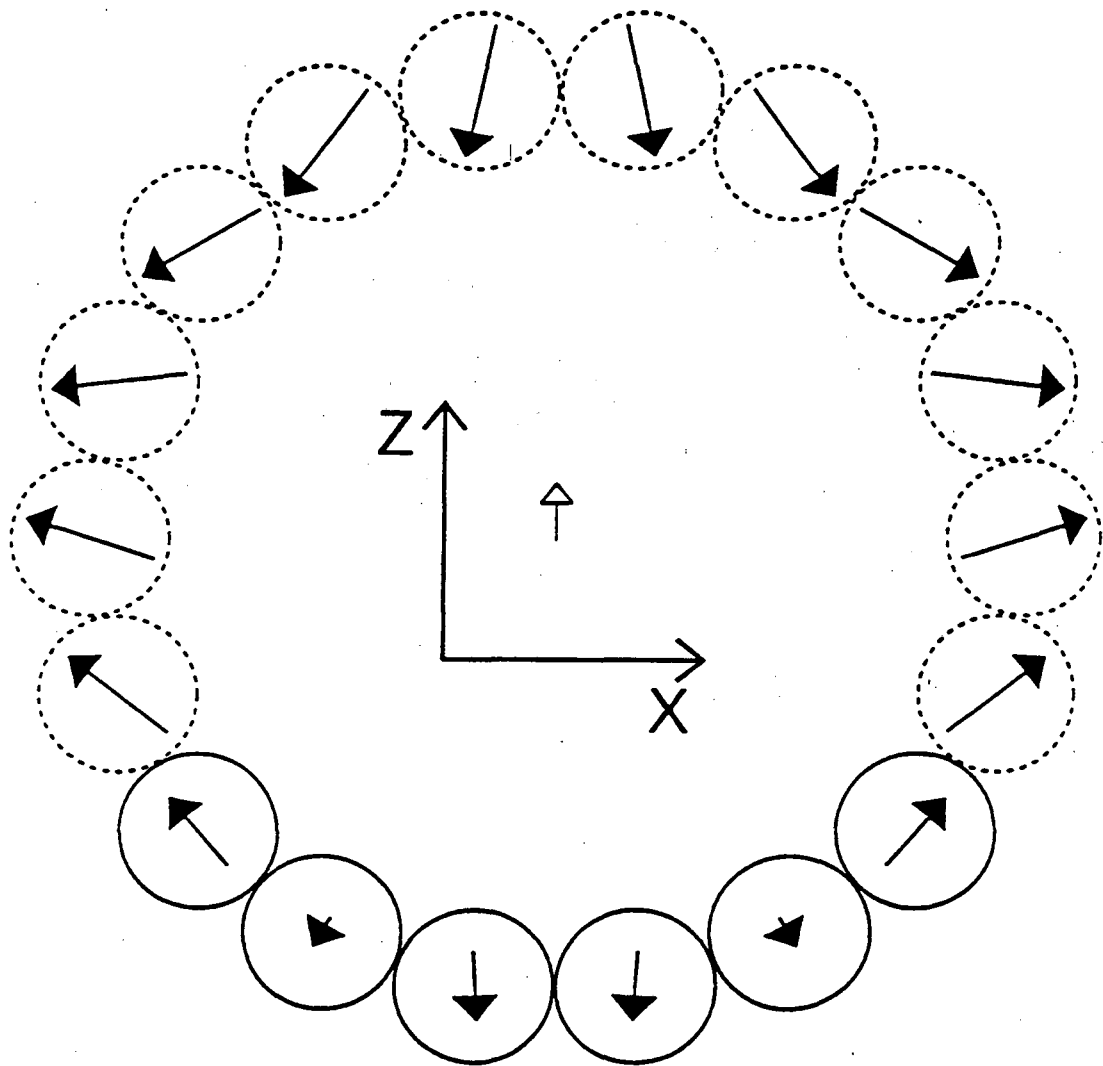


Fig. 2

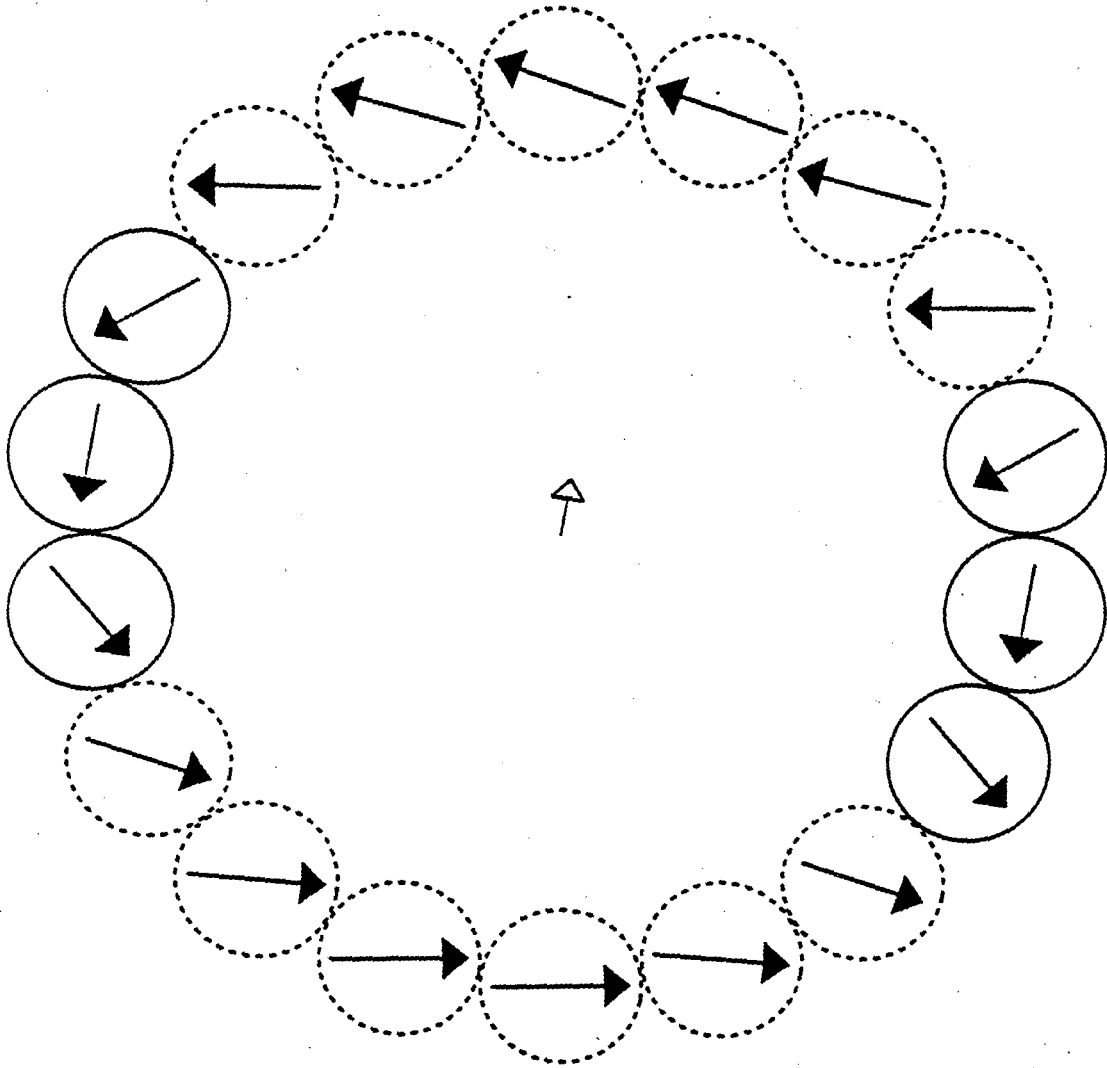


Fig. 3

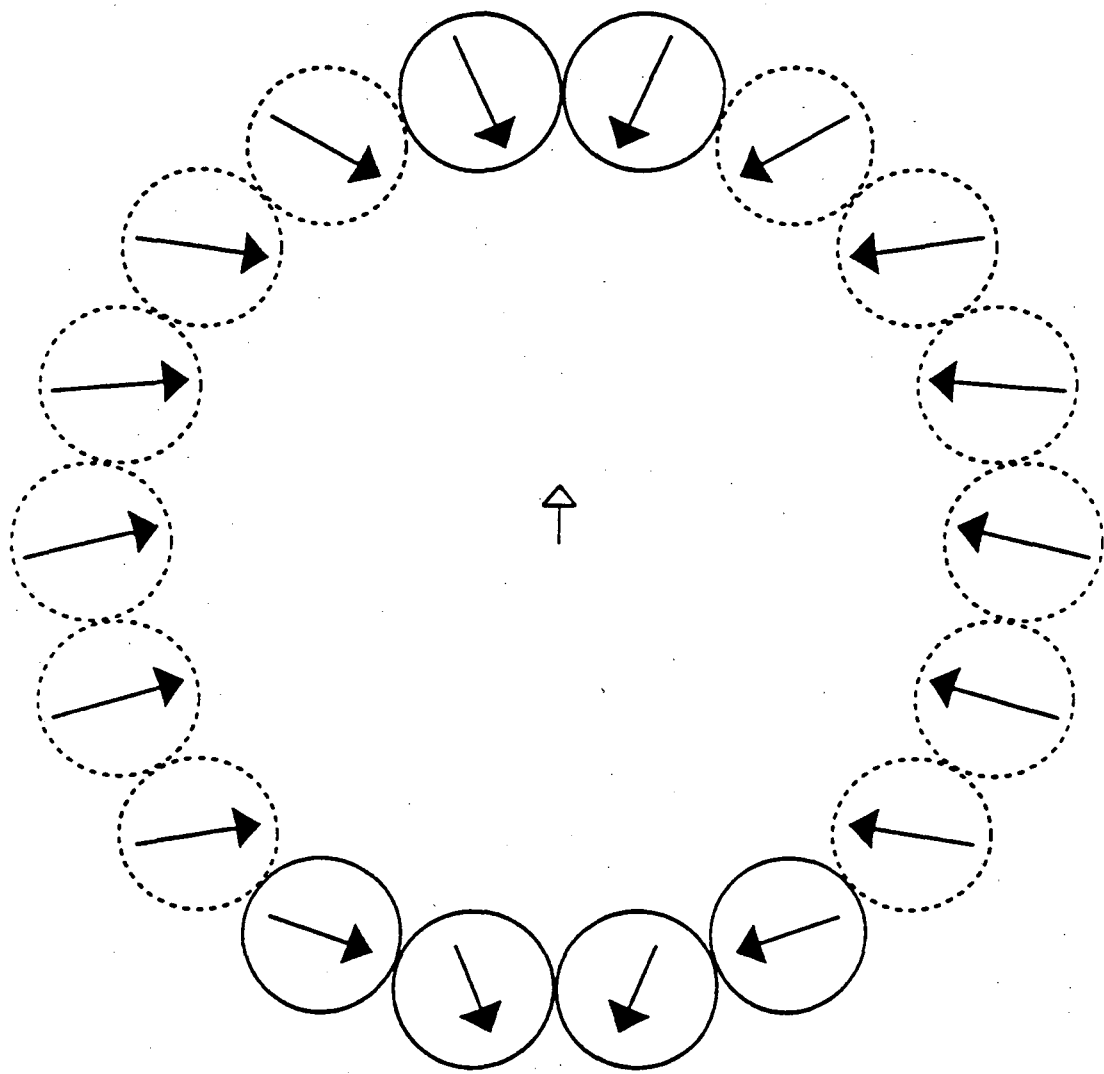


Fig. 4

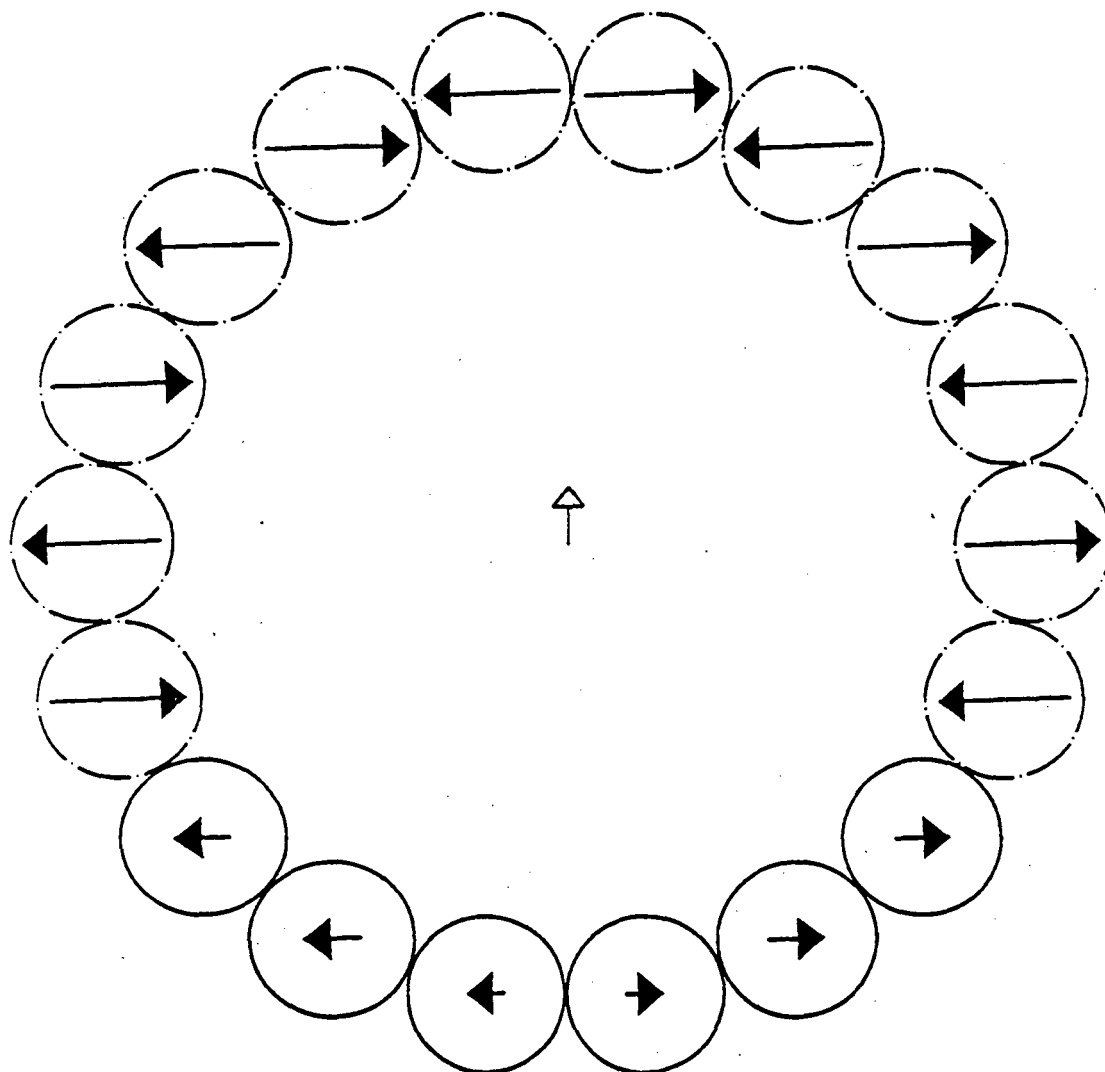


Fig. 5

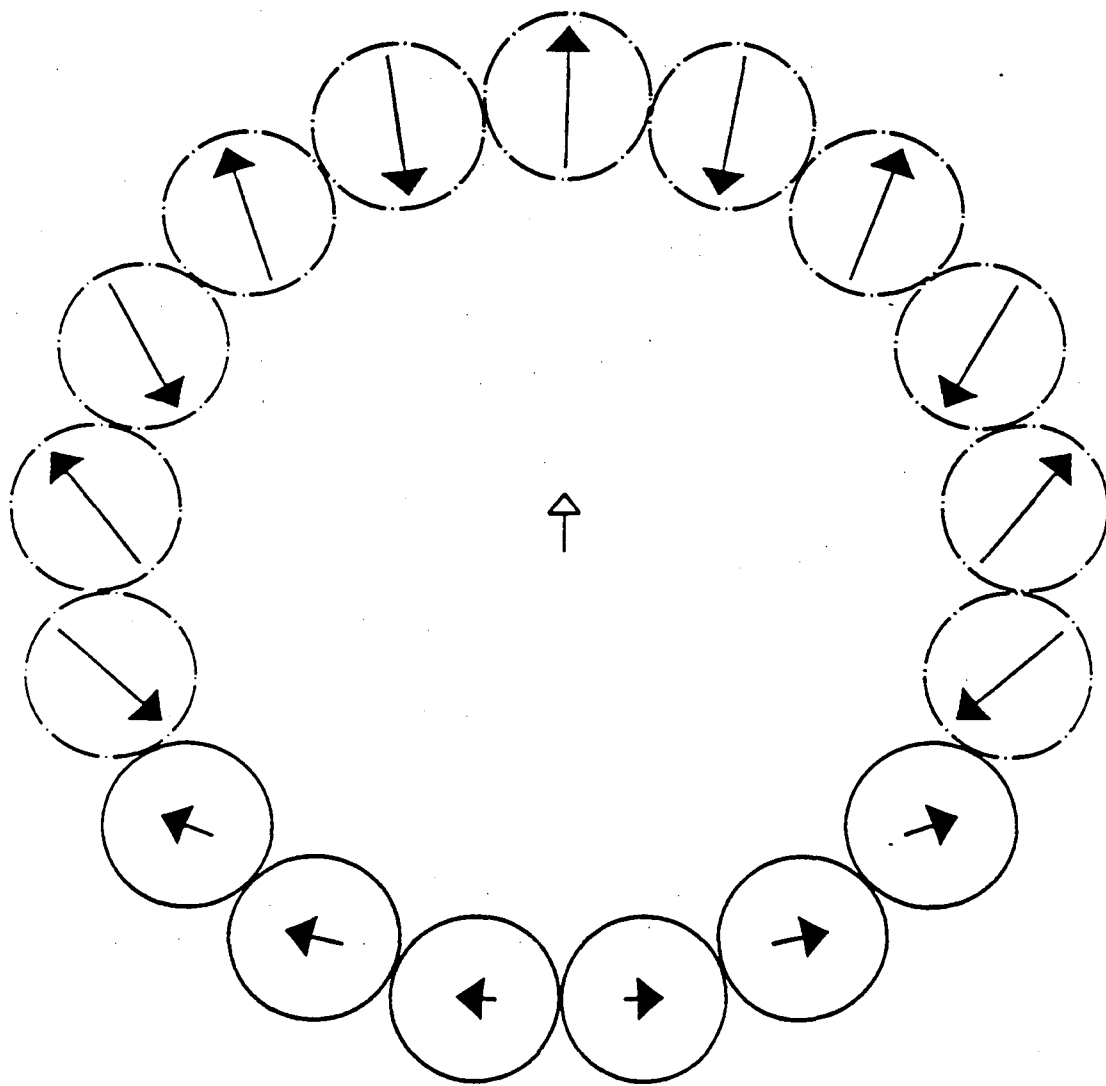


Fig. 6



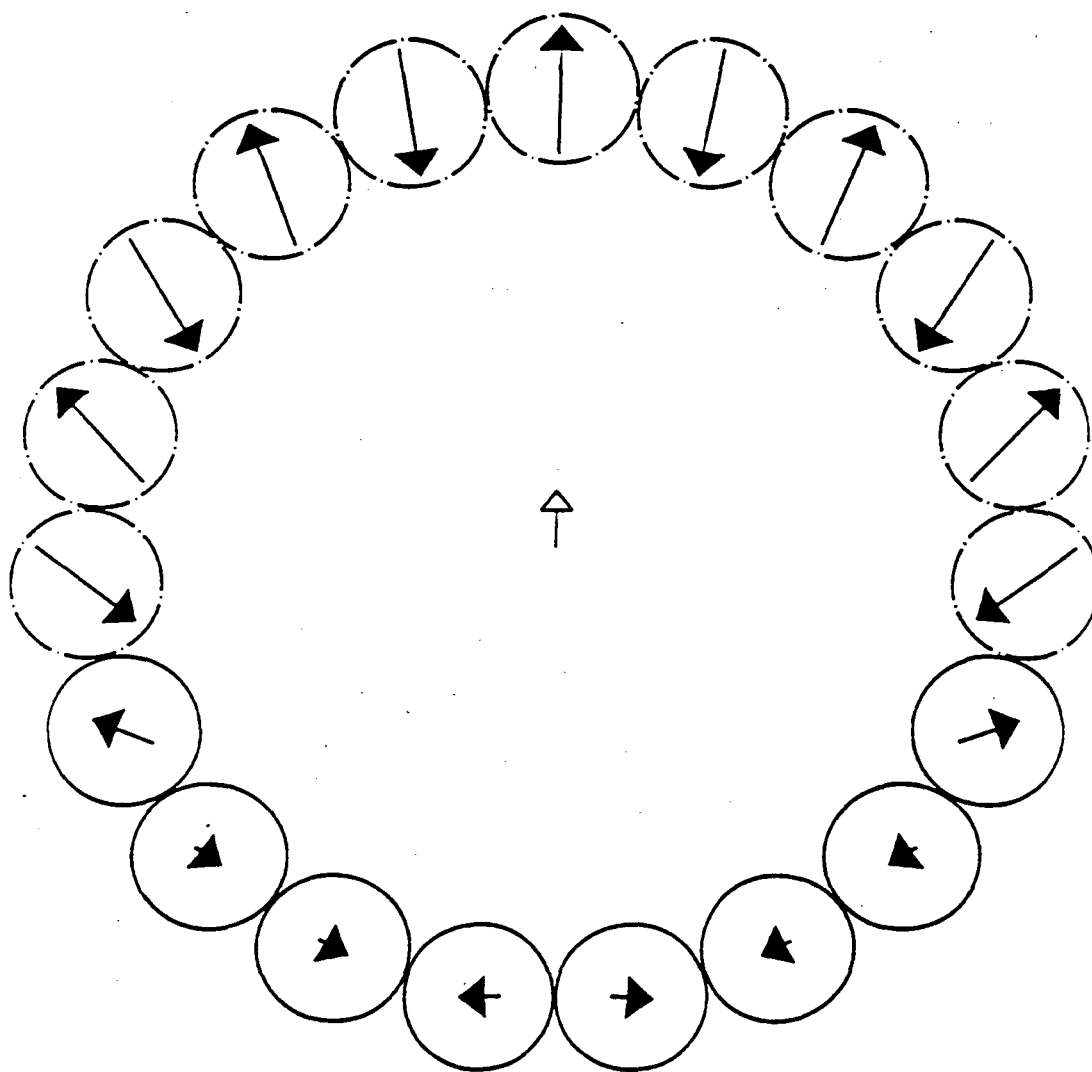


Fig. 7

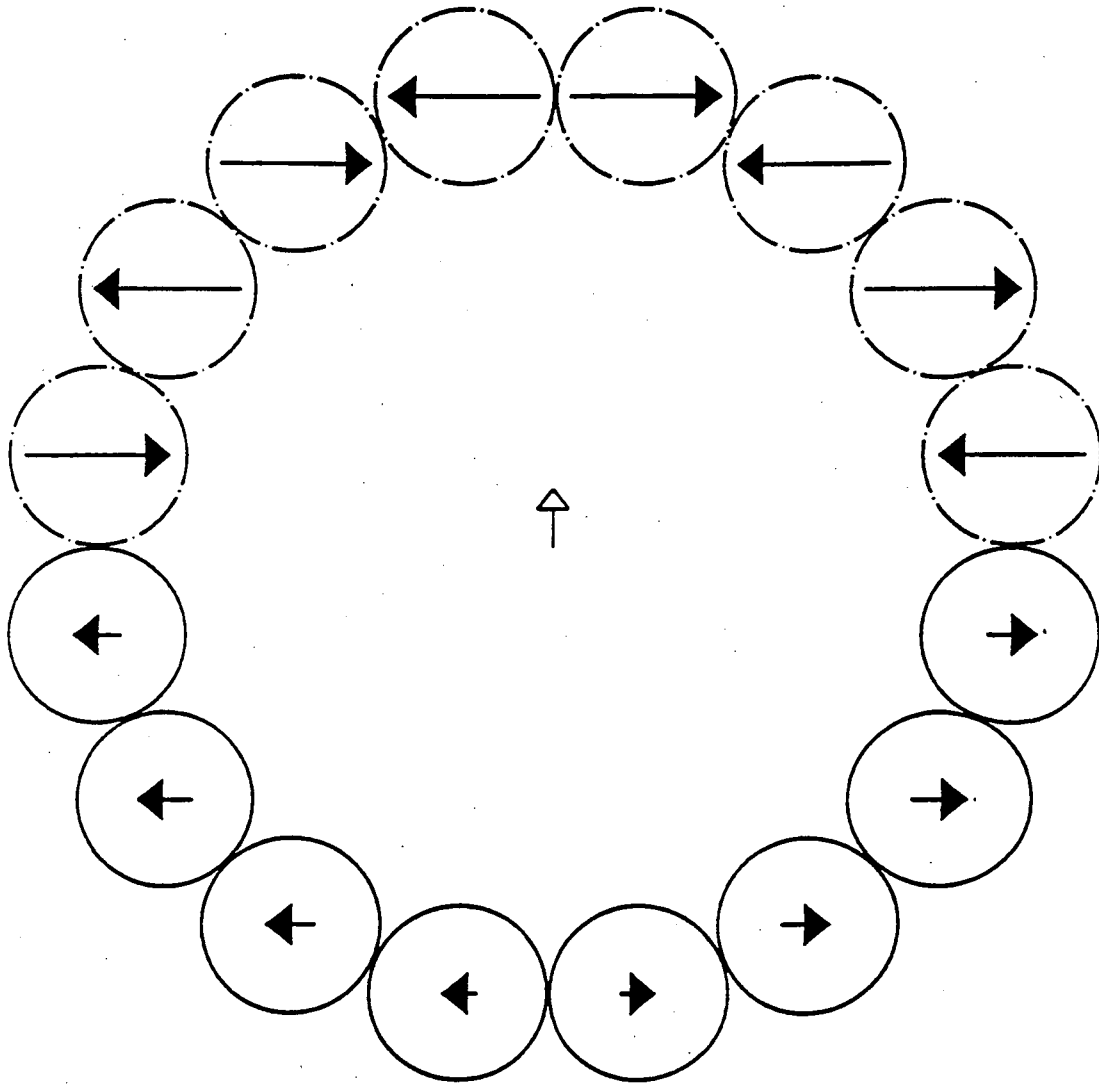


Fig. 8

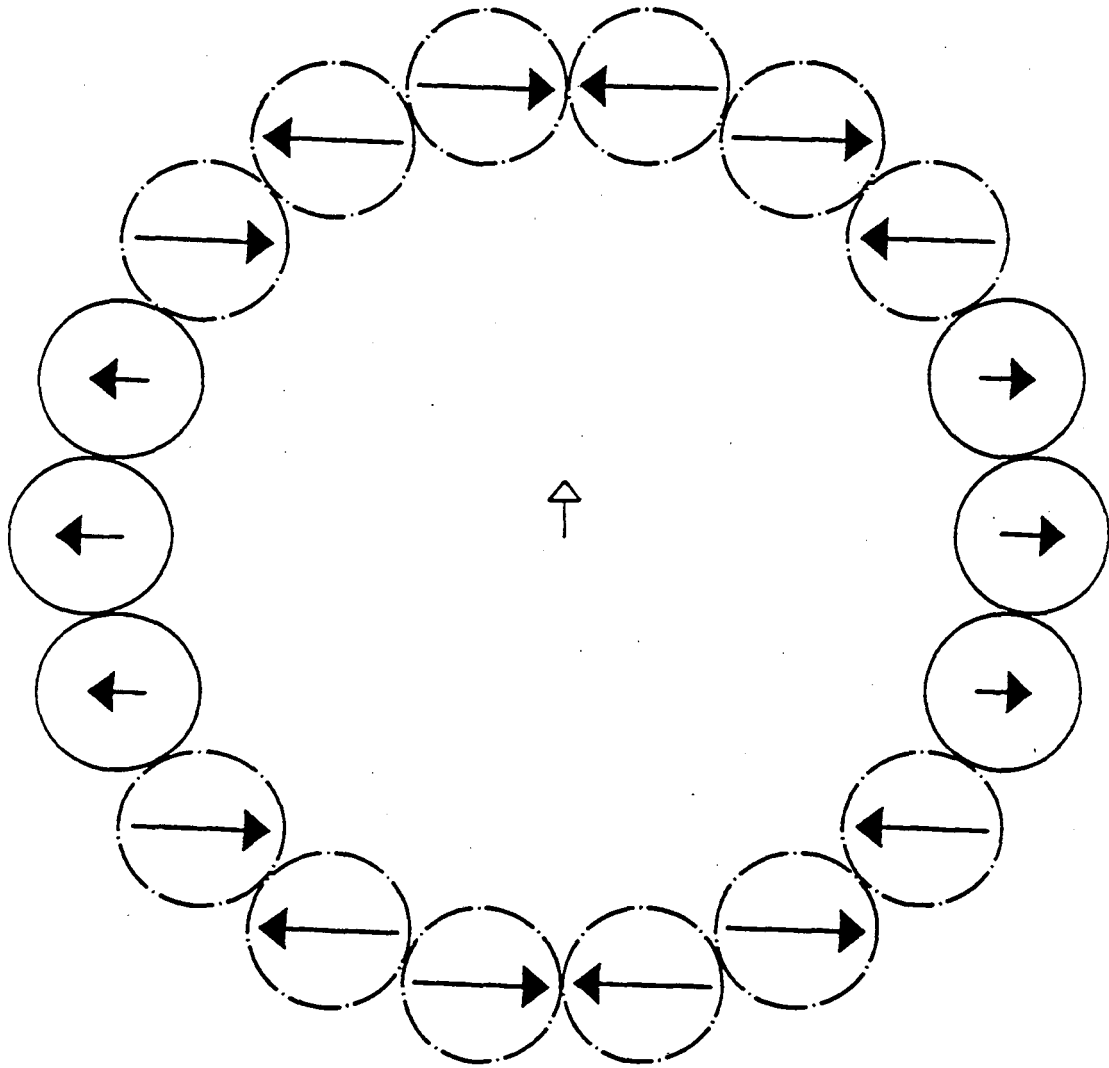


Fig. 9

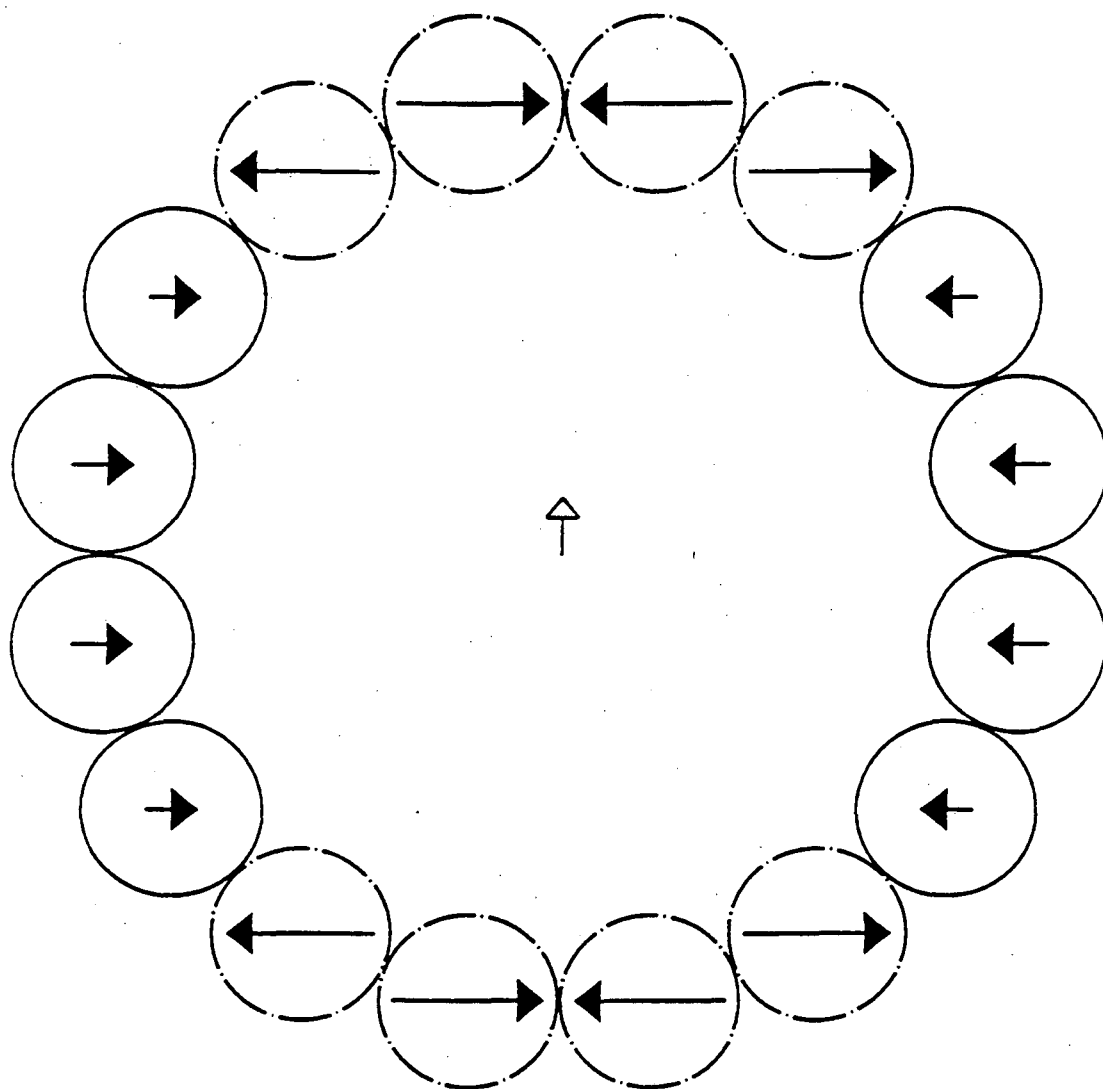


Fig. 10

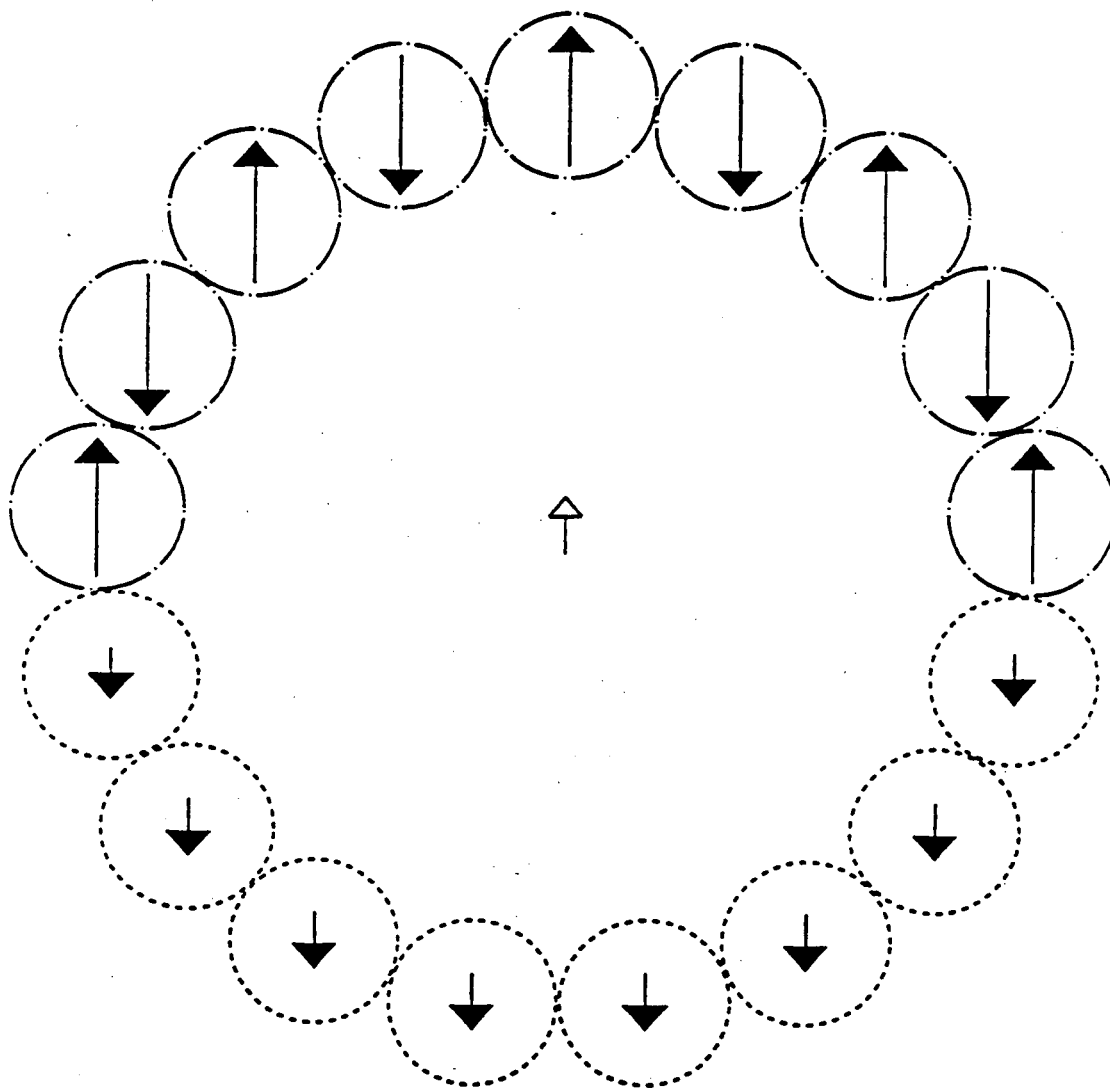


Fig. 11

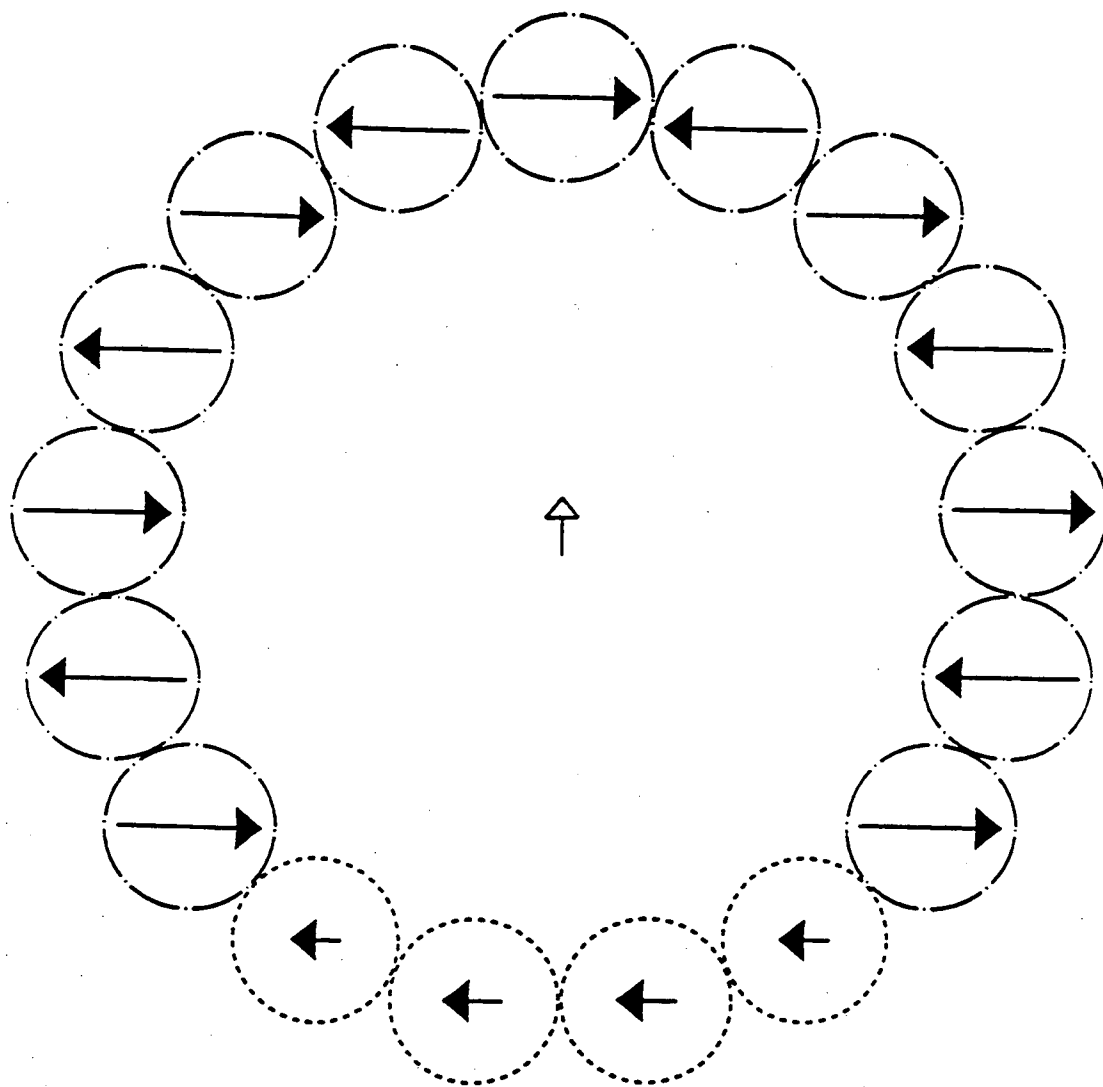


Fig. 12

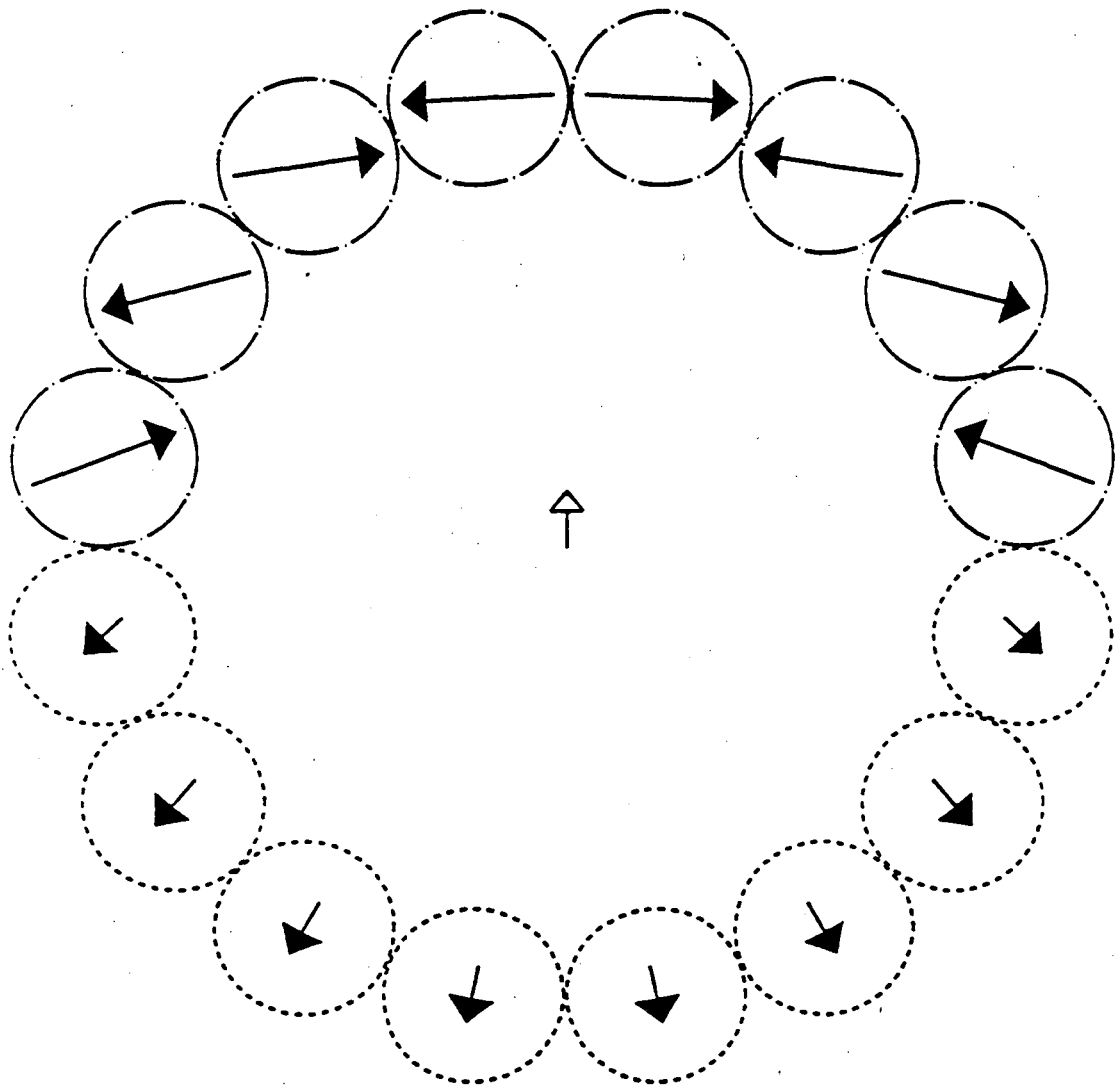


Fig. 13

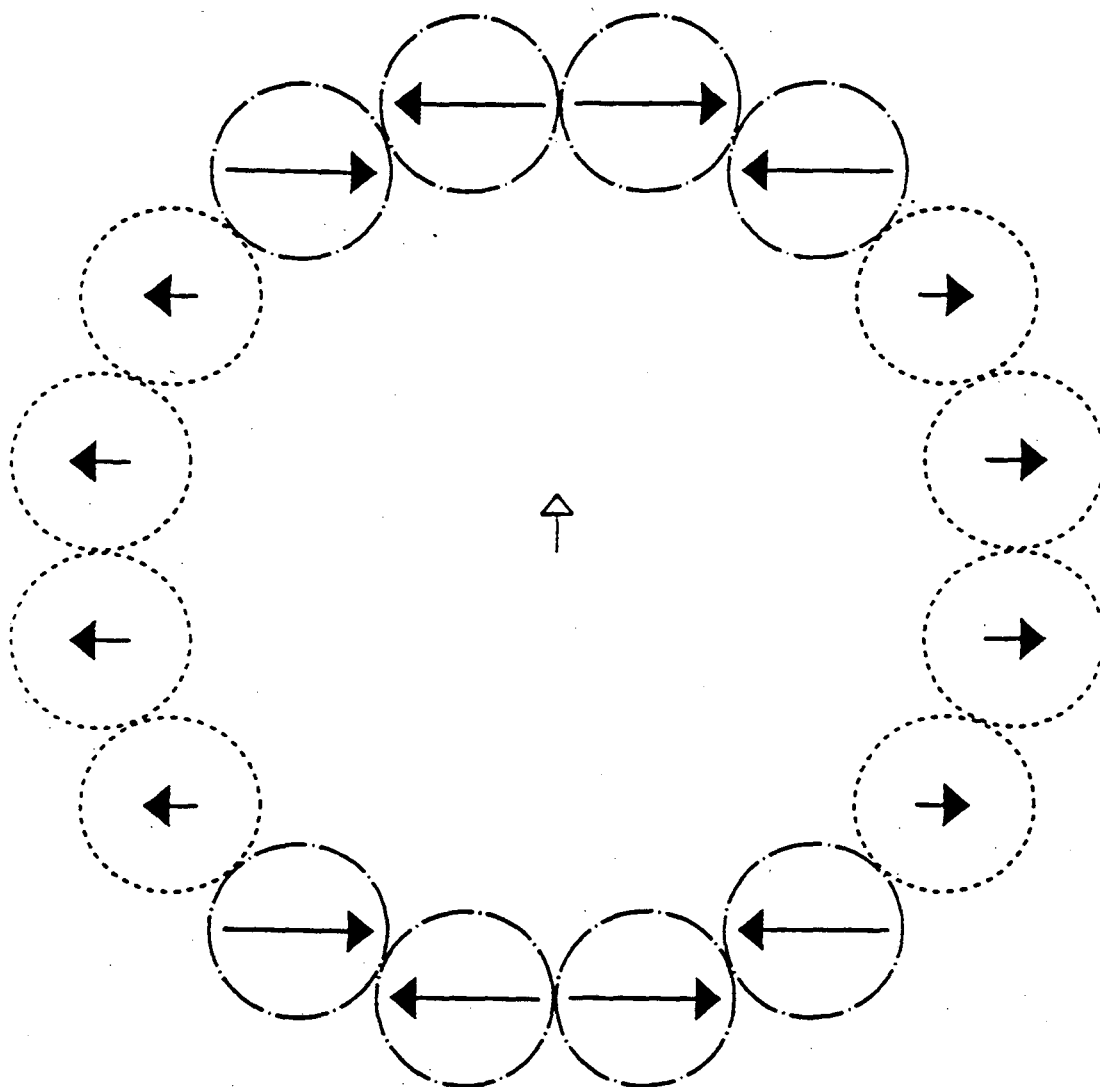


Fig. 14



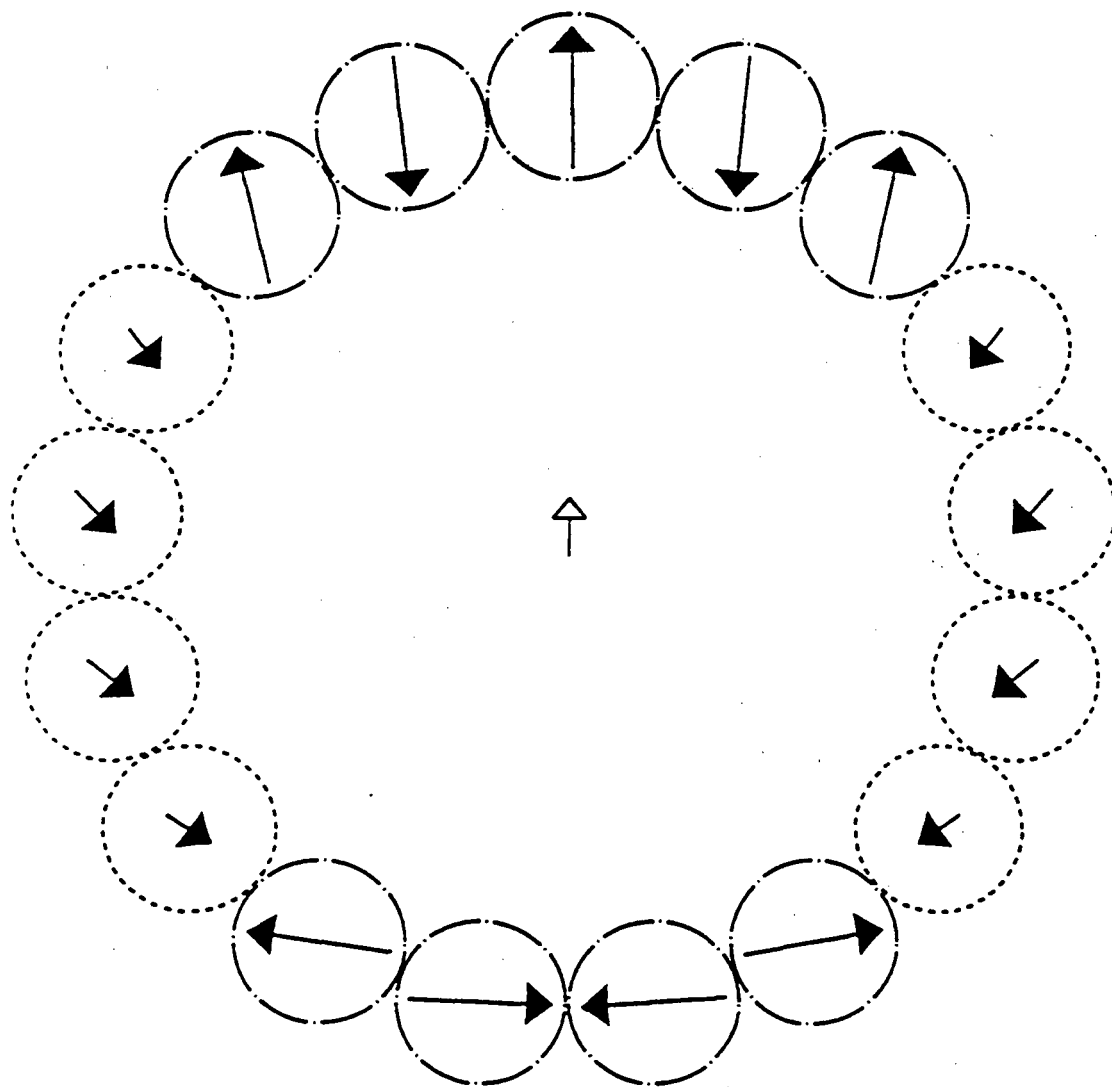


Fig. 15

## Chapter III: Boltzmann Equation Approach to the Negative Magnetoresistance of Ferromagnetic-Normal Metallic Multilayers

### A. Introduction

Since, as discussed in chapter I, interfacial scattering plays a significant role in the MR of many different ferromagnetic-normal-metal multilayers, a realistic treatment of the interfacial scattering is of importance. Camley and Barnaś's model<sup>1,2</sup> description of the MR effect, despite being one of the more complete proposed before this thesis, makes a number of unsuitable approximations, in particular with respect to interfacial scattering. They (A) neglect the difference in phase space available for scattering of electrons with different spin; and (B) they neglect the angular dependence of the transmission and reflection coefficients at the interfaces. These approximations are not made here.

The present model, an extension of the Fuchs-Sondheimer theory,<sup>3,4</sup> uses a Stoner description<sup>5</sup> of the itinerant ferromagnetic Fe layers: it introduces different potentials for majority and minority spins. Band-structure and electron-density effects are included only by means of a constant, metal- and spin-dependent potential, and an isotropic effective mass for each spin in each layer. The different potentials in neighboring layers results in coherent potential scattering (*i.e.*, refraction) of electrons as they traverse the interface. It has been suggested<sup>6</sup> that this effect alone could account for the observed spin-dependent transport properties and the oscillatory effects with layer thickness.<sup>7</sup> Spin-dependent potentials are also responsible for different densities of states at the Fermi level, *i.e.*, different available phase space for the two different spin orientations. This spin-dependent scattering mechanism was found to be important in describing correctly the MR caused by domain-wall scattering in ferromagnetic materials.<sup>8</sup> The angular-dependent effects are treated by a quantum-mechanical matching of the electron wave functions at the interfaces. Impurity scattering at the interface

and interfacial roughness are also a source of spin-dependent scattering, and they contribute to the present model through a single spin-dependent parameter, in a way similar to that used by Camley and Barnaś.

The model here also permits a comparison between Fe-Cu and Fe-Cr sandwiches and explains why, although the two systems have many similarities (*e.g.*, long-range oscillatory interlayer coupling), they exhibit a large difference in MR properties.

The model predicts the dependence of the MR on the thickness of the layers, on the quality of the samples (mean free path) and on the quality (roughness) of the surfaces and interfaces.

In section B a detailed description of the model is given. In section C results are presented. Section D contains the discussion and conclusions.

## B. Model

The in-plane conductivity has been calculated for three-layer sandwich structures. Figure 1 shows the system and defines the axes and geometric parameters. Both the current and the time-independent electric field are in the  $\hat{x}$  direction. A sandwich consists of three flat layers (labeled 1, 2 and 3) of infinite extent in the  $\hat{x}$  and the  $\hat{y}$  directions of thicknesses  $d_1$ ,  $d_2$ , and  $d_3$ . The structures investigated have identical ferromagnetic materials in layers 1 and 3 and a normal metal in layer 2. The symbols  $\alpha$  and  $\beta$  are used to denote the surfaces of layers 1 and 3 with the vacuum, respectively.

For a given sandwich the conductivity was calculated for both antiparallel alignment, denoted  $\sigma_{\uparrow\downarrow}$ , and for parallel alignment, denoted  $\sigma_{\uparrow\uparrow}$ , of the ferromagnetic moments of layers 1 and 3. Antiparallel alignment of ferromagnetic layers in the absence of applied magnetic fields has been observed in Fe-Cr and Fe-Cu multilayers<sup>7,9</sup> and is believed to be caused by an antiferromagnetic interlayer coupling.<sup>10,11</sup> Application of a sufficiently large magnetic field causes the magnetic moments to align parallel to one another. The magnetoresistance ( $\Delta\rho / \rho$ ), is defined by

$$\frac{\Delta\rho}{\rho} \equiv \frac{\rho_{\uparrow\downarrow} - \rho_{\uparrow\uparrow}}{\rho_{\uparrow\downarrow}} = \frac{\sigma_{\uparrow\uparrow} - \sigma_{\uparrow\downarrow}}{\sigma_{\uparrow\uparrow}}, \quad (1)$$

where  $\rho_{\mu,\nu} = (\sigma_{\mu,\nu})^{-1}$ . Note that this quantity varies between zero and one (or 0 and 100%) whenever the resistance decreases upon the application of an external magnetic field.<sup>12</sup>

The conductivity for both alignments is obtained by adding the contributions of the spin-up and the spin-down electrons, calculated separately. This is the two-current model,<sup>13</sup> which provides a good description of electron transport in magnetic 3d metals. As mentioned in chapter I, spin-flip processes, which mix the two currents, are neglected. It is known that their effect is small at low temperatures.<sup>13</sup>

The electrons involved in transport are regarded as free-electron-like, with spherical Fermi surfaces. Within each layer the electrons move in a constant potential  $V_{i\sigma}$  which depends on the particular layer  $i$  and the spin  $\sigma$  of the electron.

The electron distribution function within each layer  $i$  and for each spin  $\sigma$  is written in the form

$$f_{i\sigma}(\mathbf{v}, z) = f_{i\sigma}^0(\mathbf{v}) + g_{i\sigma}(\mathbf{v}, z), \quad (2)$$

which is independent of  $x$  and  $y$  by symmetry. In (2), the first term  $f_{i\sigma}^0(\mathbf{v})$  is the equilibrium distribution in the absence of an electric field and  $g_{i\sigma}(\mathbf{v}, z)$  is the deviation from that equilibrium in the presence of the electric field. For an electric field of magnitude  $E$  in the  $\hat{x}$  direction, the Boltzmann equation in the relaxation time approximation reduces to

$$\frac{\partial g_{i\sigma}}{\partial z} + \frac{g_{i\sigma}}{\tau_{i\sigma} v_z} = \frac{|e|E}{m_{i\sigma} v_z} \frac{\partial f_{i\sigma}^0}{\partial v_x}, \quad (3)$$

where  $\tau_{i\sigma}$  is the relaxation time in layer  $i$  for spin  $\sigma$ , and  $e$  is the charge of the electron. The second-order term, proportional to  $(E \times g_{i\sigma})$ , has been discarded since non-linear effects (deviations from Ohm's law) are neglected. The Lorentz-force term, proportional to  $(\mathbf{v} \times \mathbf{H}/c)$ , has also been dropped from the Boltzmann equation since

it gives an effect which is orders of magnitude smaller than those considered here.<sup>1</sup>

Because of the boundary conditions it is useful to divide  $g_{i\sigma}$  into two parts:  $g_{i\sigma}^+(\mathbf{v}, z)$  if  $v_z \geq 0$  and  $g_{i\sigma}^-(\mathbf{v}, z)$  if  $v_z < 0$ . The general solution to Eq. (3) takes the form

$$g_{i\sigma}^{\pm}(\mathbf{v}, z) = \frac{|e| \tau_{i\sigma} E}{m_{i\sigma}} \frac{\partial f^0(\mathbf{v})}{\partial v_x} \left\{ 1 + F_{i\sigma}^{\pm}(\mathbf{v}) e^{\mp \frac{z}{\tau_{i\sigma} |v_z|}} \right\}, \quad (4)$$

where the functional form of  $F_{i\sigma}(\mathbf{v})$  is determined by requiring the electron distribution function to satisfy the boundary conditions described below.

At the two outer surfaces,  $\alpha$  and  $\beta$ , the boundary conditions are

$$\begin{aligned} g_{1\sigma}^+ &= P_{\alpha\sigma} g_{1\sigma}^- & \text{at } z=0 &, \\ g_{3\sigma}^- &= P_{\beta\sigma} g_{3\sigma}^+ & \text{at } z=d &, \end{aligned} \quad (5)$$

where  $d = d_1 + d_2 + d_3$  is the total thickness of the sandwich. The specularity factors,  $P_{\alpha\sigma}$  and  $P_{\beta\sigma}$  for the respective surfaces and for electrons of spin  $\sigma$ , take values between zero (completely diffusive scattering) and one (completely specular scattering) and provide a measure of the surface roughness. In (5), and in the boundary conditions at the interfaces in (6) below, the explicit functional dependence of the distribution functions  $g_{i\sigma}^{\pm}$  has been dropped.

The boundary conditions for the potential (non-diffusive) scattering at the 1-2 and 2-3 interfaces take the form

$$\begin{aligned} g_{1\sigma}^- &= S_{12;1;\sigma} R_{12\sigma} g_{1\sigma}^+ + S_{21;1;\sigma} T_{21\sigma} g_{2\sigma}^- & \text{at } z = d_1 &, \\ g_{2\sigma}^+ &= S_{21;2;\sigma} R_{21\sigma} g_{2\sigma}^- + S_{12;2;\sigma} T_{12\sigma} g_{1\sigma}^+ & \text{at } z = d_1 &, \\ g_{2\sigma}^- &= S_{23;2;\sigma} R_{23\sigma} g_{2\sigma}^+ + S_{32;2;\sigma} T_{32\sigma} g_{3\sigma}^- & \text{at } z = d_1 + d_2 &, \\ g_{3\sigma}^+ &= S_{32;3;\sigma} R_{32\sigma} g_{3\sigma}^- + S_{23;3;\sigma} T_{23\sigma} g_{2\sigma}^+ & \text{at } z = d_1 + d_2 &. \end{aligned} \quad (6)$$

Here  $S_{ij;j,\sigma}$  which vary between zero and one, are factors that indicate the degree of potential scattering at each of the interfaces  $i-j$  for a spin  $\sigma$  electron arriving from

layer  $i$  and being scattered into the layer  $l$ . The scattering follows the reflection-refraction laws when  $S = 1$  and is completely diffusive when  $S = 0$ . The notation used for the transmission  $T$  and the reflection  $R$  coefficients is the following:  $T_{ij\sigma} \equiv$  probability for an electron of spin  $\sigma$  in layer  $i$  to be transmitted (refracted) into layer  $j$ ;  $R_{kl\sigma} \equiv$  probability for an electron of spin  $\sigma$  in layer  $k$  with a velocity directed towards layer  $l$  to be reflected back into layer  $k$ . The equations and boundary conditions, as written, satisfy all the necessary conservation laws.

The functional form of  $S_{ij;l,\sigma}$  depends in detail on the nature of the interfaces. In chapter IV specific interfacial morphologies are considered along with the corresponding functional forms of  $S_{ij;l,\sigma}$ . In this chapter only the averaged effects of the interfacial scattering due to roughness and the presence of impurities are considered. Two parameters  $S_M$  and  $S_m$ , for the majority and the minority spins respectively, are introduced to describe the averaged effects of interfacial scattering. The scattering is taken to be the same at each of the interfaces. Formally this can be viewed as the case when the function  $S_{ij;l,\sigma}$  is independent of the direction and angle of incidence at the interface and satisfies

$$\begin{aligned} S_{F,S;F;M} &= S_{F,S;S;M} = S_{S,F;F;M} = S_{S,F;S;M} = S_M \quad , & (7) \\ S_{F,S;F;m} &= S_{F,S;S;m} = S_{S,F;F;m} = S_{S,F;S;m} = S_m \quad . \end{aligned}$$

The subscripts  $S$  and  $F$  refer to a spacer layer and a ferromagnetic layer respectively.

The functional dependence of the reflection and transmission coefficients was determined by matching the free electron-like (plane-wave) functions and their derivatives at each interface. The solution to this problem, which is identical to that encountered in optics for an interface between two media with different index of refraction, is shown schematically in Fig. 2. The reflection  $R$  and transmission  $T$  coefficients take the form<sup>14</sup>

$$R_{ij\sigma}(E, \theta) = \left| \frac{1 - h_{ij\sigma}(E, \theta)}{1 + h_{ij\sigma}(E, \theta)} \right|^2 ,$$

$$T_{ij\sigma}(E, \theta) = \frac{4 \operatorname{Re} [h_{ij\sigma}(E, \theta)]}{|1 + h_{ij\sigma}(E, \theta)|^2} = 1 - R_{ij\sigma}(E, \theta) .$$

Here  $\theta$  is the angle of incidence, measured with respect to the  $z$ -axis, of an electron of energy  $E = \frac{1}{2} m_{i\sigma} v^2 + V_{i\sigma}$  in layer  $i$  with spin  $\sigma$  and velocity  $v$  moving in a constant potential  $V_{i\sigma}$ . The scattering is completely elastic, *i.e.*, the energy of the electron is a constant of the motion. The symbol  $\operatorname{Re}$  means "the real part of"; the function  $h_{ij\sigma}(E, \theta)$  has the form

$$h_{ij\sigma}(E, \theta) = \frac{\sqrt{\frac{E - V_{j\sigma}}{E - V_{i\sigma}} - \sin^2 \theta}}{\cos \theta}$$

The transmission and reflection coefficients appearing in (6) are related by

$$R_{ij\sigma}(E, \theta_i) = R_{ji\sigma}(E, \theta_j) ,$$

$$T_{ij\sigma}(E, \theta_i) = T_{ji\sigma}(E, \theta_j) ,$$

where

$$\frac{\sin \theta_i}{\sin \theta_j} = \sqrt{\frac{E - V_{j\sigma}}{E - V_{i\sigma}}} ;$$

this is a consequence of the principle of (optical) reversibility.<sup>15</sup>

Substitution of Eq. (4) into the boundary Eqs. (5) and (6) yields unique solutions of  $F_{i\sigma}^{\pm}(v)$ . The form of the boundary conditions are such that these functions depend only on the magnitude of the velocity  $v$  and the cosine of its angle with respect to the  $z$ -axis. Therefore, the functions can be written as  $F_{i\sigma}^{\pm}(v, \cos \theta)$  where the plus sign corresponds to  $0 \leq \theta \leq \pi/2$  and the minus sign corresponds to  $\pi/2 < \theta \leq \pi$ .

The current density along the electric field in each layer  $i$  for electrons with spin  $\sigma$  is given by

$$J_{xi\sigma}(z) = -|e| \left[ \frac{m_{i\sigma}}{h} \right]^3 \int v_x g_{i\sigma}(v, z) d^3v, \quad (8)$$

where  $h$  is Planck's constant. Substitution of Eq. (4) into Eq. (8) and the use of Fermi-Dirac statistics for  $f_{i\sigma}^0$  yields

$$J_{xi\sigma}(z) = \sigma_{i\sigma} E \left\{ 1 + \frac{3}{4} \int_{-1}^1 \bar{F}_{i\sigma}(u) (1-u^2) e^{-\frac{z}{\lambda_{i\sigma} u}} du \right\}, \quad (9)$$

where the Fermi velocity  $v_{Fi\sigma}$  is given by

$$v_{Fi\sigma} = \sqrt{\frac{2(E_F - V_{i\sigma})}{m_{i\sigma}}}$$

for an electron with the Fermi energy  $E_F$ . The mean free path,  $\lambda_{i\sigma}$ , is defined by  $\lambda_{i\sigma} \equiv v_{Fi\sigma} \tau_{i\sigma}$ . The bulk conductivity of electrons from layer  $i$  of spin  $\sigma$  is denoted by  $\sigma_{i\sigma}$  and is given by

$$\sigma_{i\sigma} = \frac{4}{3} \pi e^2 \tau_{i\sigma} (m_{i\sigma})^2 \left[ \frac{v_{Fi\sigma}}{h} \right]^3.$$

The function  $\bar{F}_{i\sigma}(u)$  is defined by the equation<sup>16</sup>

$$\bar{F}_{i\sigma}(u) = \begin{cases} F_{i\sigma}^+(v_{Fi\sigma}, u) & \text{if } u \geq 0 \\ F_{i\sigma}^-(v_{Fi\sigma}, u) & \text{if } u < 0 \end{cases}.$$

Physically the first term in Eq. (9) corresponds to the current in a solid of infinite extent with no surfaces or interfaces. The second term is a measure of the deviation in the current caused by the presence of surfaces and interfaces. Plots are shown below which show how the current is distributed throughout the trilayer. In order to obtain the MR one requires the effective conductivity, which is found by averaging over the whole film

$$\sigma = \frac{1}{E d} \sum_{i=1}^3 \sum_{\sigma=\uparrow, \downarrow} \int J_{xi\sigma}(z) dz.$$



Integration yields

$$\sigma = \sum_{i=1}^3 \sum_{\sigma=\uparrow,\downarrow} \sigma_{i\sigma} \left[ \left( \frac{d_i}{d} \right) - \frac{3}{4} \left( \frac{\lambda_{i\sigma}}{d} \right) \int_{-1}^1 du (1-u^2) u \bar{F}_{i\sigma}(u) \left\{ e^{-\frac{z_i}{\lambda_{i\sigma}u}} - e^{-\frac{z_{i-1}}{\lambda_{i\sigma}u}} \right\} \right], \quad (10)$$

where  $z_0 = 0$ ,  $z_1 = d_1$ ,  $z_2 = d_1 + d_2$ , and  $z_3 = d$ . The first term in Eq. (10) can be interpreted as the bulk conductivity of each layer weighted by its relative thickness. The exponential factors in Eqs. (9) and (10), which go to infinity as  $u \rightarrow 0^-$ , are compensated by the prefactor  $\bar{F}_{i\sigma}(u)$ , which approaches zero rapidly enough in the same limit to insure integrability.

The MR,  $(\Delta\rho / \rho)$ , is found by calculating independently the conductivities  $\sigma_{\uparrow}$  and  $\sigma_{\downarrow}$ . Although in some cases the ferromagnetic layers may be different, in all results presented here it was assumed that the ferromagnetic layers 1 and 3 are composed of the same material with identical bulk properties. This assumption reduces the number of parameters necessary to characterize a structure. Associated with the electrons in layers 1 and 3 are the minority (denoted using a small subscript  $m$ ) and the majority (denoted using a capital subscript  $M$ ) spins with effective masses  $m_m$  and  $m_M$ , relaxation times  $\tau_m$  and  $\tau_M$ , and potentials  $V_m$  and  $V_M$ . The spin-up and spin-down electrons in layer 2, which is the normal-metal or spacer layer, move in a potential  $V_s$  with an effective mass  $m_s$  and relaxation time  $\tau_s$ . At the outer surfaces  $\alpha$  and  $\beta$  of the ferromagnetic layers 1 and 3 respectively, the surface scattering parameters for the majority and the minority spins are described by  $P_{\alpha M}$ ,  $P_{\beta M}$ ,  $P_{\alpha m}$ , and  $P_{\beta m}$ . At the interfaces  $S_M$  and  $S_m$  describe the interfacial scattering of the majority and the minority spins, respectively.

The values of the potentials are determined by treating all of the valence  $s$  and  $d$  electrons as being in a single free-electron-like band with an isotropic effective mass. The effective mass is, in general, taken to be larger than the electron mass, since the

$d$  electrons, which contribute to the density of electrons, are in narrower bands than the free-electron-like  $s$  electrons. Within the ferromagnetic layers 1 and 3, the bands for the minority and the majority spins are shifted by a  $k$ -independent exchange potential, yielding two different spin-dependent, constant potentials,  $V_m$  and  $V_M$ . The value of the exchange splitting is chosen so that the difference in the density of the majority and the minority electrons yields the net magnetic moment of the bulk ferromagnetic material.

### C. Results

The theory, as developed thus far for a sandwich of two identical ferromagnetic metals separated by a layer of a normal metal, includes 18 parameters:

three effective masses  $m_M$ ,  $m_m$ , and  $m_s$ ;

three constant potentials  $V_M$ ,  $V_m$ , and  $V_s$ ;

three relaxation times  $\tau_M$ ,  $\tau_m$ , and  $\tau_s$ ;

three thicknesses  $d_1$ ,  $d_2$ , and  $d_3$ ;

four free-surface scattering parameters  $P_{\alpha M}$ ,  $P_{\alpha m}$ ,  $P_{\beta M}$  and  $P_{\beta m}$ ;

and two interface scattering parameters  $S_M$ ,  $S_m$

The results presented here include only the cases for which the *relaxation times* are identical  $\tau \equiv \tau_m = \tau_M = \tau_s$ . (The *mean free paths* of the minority and the majority spins within the ferromagnetic layers 1 and 3 and for the spacer metal are still different, however, since the Fermi velocities are different.) The discussion of the results is also confined to the situation  $d_F \equiv d_1 = d_3$  and  $d_s \equiv d_2$ , since this is the most common case. At the outer surfaces all  $P$ s are taken to be identical  $P \equiv P_{\alpha M} = P_{\alpha m} = P_{\beta M} = P_{\beta m}$ . The spin-dependence of these parameters is caused mostly by magnetic impurities, which are taken not to be present at the outer (identical) surfaces.

Results are given for two different multilayer systems, Fe-Cr and Fe-Cu. In these three metals the isotropic effective mass is assumed to be independent of the material

and spin orientation with a value  $m_M = m_m = m_s = 4.0 \times$  free-electron mass. With this effective mass the potentials, with respect to the Fermi energy  $E_F$  chosen to be at  $E_F = 0$ , are

$$V_M = -8.23 \text{ eV}, V_m = -5.73 \text{ eV} \text{ for Fe};$$

$$V_s = -5.77 \text{ eV} \text{ for Cr};$$

$$V_s = -8.54 \text{ eV} \text{ for Cu}.$$

Figure 3 shows the potential energies:  $V_M$ ,  $V_m$ , and  $V_s$  for Fe-Cu for the spin-up and spin-down electrons for both the parallel and the antiparallel configurations.

The parameters that remain to be specified for each case (Fe-Cr and Fe-Cu) are altogether six: (A) two geometric parameters  $d_F$  and  $d_s$ , the thicknesses of the ferromagnetic and spacer layers respectively; (B) one relaxation time  $\tau$ , which depends on bulk sample properties; (C) one outer-surface scattering parameter  $P$  (the roughness of the outer surfaces); and (D) two interface scattering parameters  $S_M$ ,  $S_m$  (diffuse scattering versus potential scattering at the interfaces for the majority and the minority spins respectively).

Even with these specifications, the phenomena under consideration are complicated functions of the 6 variables, and the task of describing these dependencies is not simple. In general terms, and with exceptions, it is found that  $(\Delta\rho / \rho)$  is a strong function of the surface and interface parameters  $P$ ,  $S_M$ , and  $S_m$ , and a relatively weak function of the thicknesses and the mean free path. For example, as  $P$ ,  $S_M$ , and  $S_m$  vary between 0 and 1, the calculated  $(\Delta\rho / \rho)$  varies between 0 and 92.7% for Fe-Cr trilayers and 0 and 94.4% for Fe-Cu trilayers, when values of  $d_F = d_s = 10.0 \text{ \AA}$  and  $\tau = 5.0 \times 10^{-13} \text{ s}$  are chosen. Figures 4 and 5 show the regions in this three-dimensional "surface and interfacial" parameter space where  $(\Delta\rho / \rho)$  is greater than 20% for these values of  $d_F$ ,  $d_s$ , and  $\tau$ . With this choice of  $\tau$ , the mean free paths are: (i) 4,250  $\text{\AA}$  for the majority-spin and 3,540  $\text{\AA}$  for the minority-spin electrons in Fe; (ii) 3,560  $\text{\AA}$  for electrons in Cr; and (iii) 4,330  $\text{\AA}$  for electrons in Cu. These values correspond to all mean free paths which are orders of magnitude larger than the film

thicknesses, *i.e.*, the clean-film limit, where surface and interface effects are supposed to be paramount.

Some of the interesting results of the calculations are illustrated in Figs. 4-11. It was found in general that:

(A) The magnetoresistance ( $\Delta\rho / \rho$ ) increases with increasing values of  $P$ , except in the region where  $S_M \approx S_m \approx 1$  (see Fig. 6).

(B) The magnetoresistance ( $\Delta\rho / \rho$ ) is in general small (only a few percent) when  $S_M = S_m$ , except when both parameters are very close to 1 (see Figs. 4, 5 and 7).

(C) The magnetoresistance ( $\Delta\rho / \rho$ ), as a function of  $d_F$ , exhibits a variety of behaviors which include (i) a monotonic decrease with increasing  $d_F$ ; (ii) an initial increase followed by a decrease (a single maximum); (iii) a decrease, followed by an increase and a subsequent decrease (a minimum followed by a maximum); in all cases the asymptotic value as  $d_F \rightarrow \infty$  is zero (see Fig. 8).

(D) The magnetoresistance ( $\Delta\rho / \rho$ ), as a function of increasing  $d_s$ , exhibits either (i) a continuous monotonic decrease, or, most commonly, (ii) a single maximum<sup>17</sup> at a value of  $d_s$  of the order of  $d_F$ ; the asymptotic value as  $d_s \rightarrow \infty$  is also zero (see Fig. 9).

(E) The magnetoresistance ( $\Delta\rho / \rho$ ), as a function of the relaxation time  $\tau$ , either (i) increases monotonically and saturates at a maximum value, or, most commonly, (ii) increases to a maximum, and then *very gradually* decreases (see Fig. 10).

Figures 4 and 5 contain information on how, for specific values of  $d_F$ ,  $d_s$ , and  $\tau$ , the quality of surfaces and interfaces influences the MR. As the surface scattering parameter  $P$  increases from 0 to 1, *i.e.*, as the scattering becomes less diffuse (or equivalently the surface roughness decreases) the MR in general increases. It is also evident from these two figures that the region of large MR is close either to the plane  $S_M = 1$ , or to the plane  $S_m = 1$ , and away from the plane  $S_M = S_m$ . There is a very large asymmetry between  $S_M$  and  $S_m$  in Fe-Cr, but considerably less so in Fe-Cu.

It is interesting to note that when  $P = 1$ , the MR of the trilayer becomes identical to that of an infinite multilayer or superlattice. A specular-scattering event makes the electron traverse the same ferromagnetic layer for a second time in the opposite direction or, equivalently, "continue" through a mirror-image of the film. Therefore, if for both surfaces  $P = 1$ , then as far as the MR is concerned, a trilayer

$$\text{vacuum} \mid d_F \mid d_s \mid d_F \mid \text{vacuum}$$

is exactly equivalent to an infinite, periodic superstructure

$$\cdots \mid 2d_F \mid d_s \mid 2d_F \mid d_s \mid 2d_F \mid d_s \mid 2d_F \mid \cdots$$

As seen above, the MR increases in general with  $P$ , because the number of interfaces where magnetic scattering can occur "increases" as  $P$  increases. When realistic values are chosen for the parameters, the MR is found to increase by as much as an order of magnitude when  $P$  increases from 0 to 1. This fact can be reinterpreted as an increase in the MR as the number of magnetic interfaces encountered by an electron within its bulk mean-free path increases.

Experimentally it is found that the more layers a sample has, the larger the MR. The (liquid He temperature) MR in Fe-Cr trilayers prepared by molecular-beam-epitaxy methods is found to be a few percent,<sup>18</sup> while the MR is found to be nearly 50% Fe-Cr in *multilayers* prepared by the same method at the same temperature.<sup>19</sup>

#### D. Discussion and Conclusions

Figure 4 shows a marked asymmetry in the dependence of  $(\Delta\rho / \rho)$  on  $S_M$  and  $S_m$ , *i.e.*, the majority- and minority-spin interface scattering have a very different effect on the MR. By contrast, a large asymmetry is not present for Fe-Cu (Fig. 5). Figure 3 shows the potential energies for Fe-Cu for both the parallel and the antiparallel configurations. It is seen that

$$|V_s| \approx |V_M| < |V_m|$$

On the other hand the bottom of the band for Cr is lower than, but much closer to that for the minority spins in iron, *i.e.*, in the Fe-Cr samples

$$|V_M| < |V_s| \approx |V_m|$$

The difference in  $V_s$  has a large effect on the MR, as can be seen in the plots of the in-plane current distribution across the trilayers. Shown in Fig. 11 are the in-plane currents for the parallel ( $PI$ ) and the antiparallel ( $An$ ) configurations of Fe-Cr with  $S_M = 0$ ,  $S_m = 1$ , and  $P = 0.5$ ; the contributions to the current of spin-up and spin-down electrons are plotted separately. For the chosen set of parameters the ( $\downarrow PI$ )-electrons undergo completely non-diffusive scattering at both interfaces, whereas ( $\downarrow An$ )-electrons and the ( $\uparrow$ )-electrons in both configurations undergo completely diffusive scattering either at one or at both interfaces. The current carried by the ( $\downarrow PI$ )-electrons is the largest of the four contributions because those electrons are, in fact, never "randomized" at the interfaces, *i.e.*, their current is not degraded by diffusive interface scattering. The fact that  $(\Delta\rho / \rho)$  is determined by the difference of the conductivities of the parallel and the antiparallel configurations, which are each proportional to the sum of the currents carried by the spin-up and spin-down electrons, explains why  $(\Delta\rho / \rho)$  is large (50.6%) in this case.

A fraction of the ( $\downarrow PI$ )-electrons in the Cr layer, those incident at low-grazing angles upon the Fe/Cr interfaces, are totally internally reflected, since  $|V_s| < |V_m|$ . These electrons scatter diffusively only within the *bulk* of the Cr layer and so are able to follow long trajectories (a full mean free path) before being scattered.<sup>20</sup> This phenomenon leads to a "channeling effect" within the Cr layer. It explains why the current carried by the ( $\downarrow PI$ )-electrons is larger in the Cr layer than in the Fe layers.

Figure 12 shows how the in-plane current is distributed across another Fe-Cr trilayer, but for  $S_M = 1$ ,  $S_m = 0$ , and  $P = 0.5$  of Fig. 4. In this case only the ( $\uparrow PI$ )-electrons are scattered non-diffusely at both interfaces. Since  $|V_s| < |V_M|$ , channeling does not occur in the Cr layer, and the current is actually larger within the Fe

layers. Channeling can only take place in the Fe layers and only when  $P$  is close to one. Therefore the regions where the MR is large, *i.e.*,  $(\Delta\rho / \rho) > 0.2$ , when  $S_M$  is close to one, are clustered around  $P = 1$ . Even when  $P$  is close to one the MR is not very large; channeling occurs in *only one* of the Fe layers for both the ( $\uparrow An$ )- and ( $\downarrow An$ )-electrons. Thus the difference  $[\sigma_{\uparrow\uparrow} - \sigma_{\uparrow\downarrow}]$  in (1) for  $S_M = 1$ ,  $S_m = 0$ , and  $P = 1$  is considerably smaller,  $(\Delta\rho / \rho) = 0.411$ , than that for with  $S_M = 0$ ,  $S_m = 1$ , and  $P = 1$ ,  $(\Delta\rho / \rho) = 0.927$ .

In the Fe-Cu trilayer, since  $|V_s|$  is greater than  $|V_M|$  and  $|V_m|$ , channeling occurs in the Cu layer when either  $S_M$  or  $S_m$  are close to one for the ( $\uparrow Pl$ )- or the ( $\downarrow Pl$ )-electrons, respectively. Channeling within the Cu layer, for either  $S_M$  or  $S_m$  close to one, leads to a large MR and to the symmetric-looking plot of Fig. 5.

Interesting surface and size effects occur when both  $S_M$  and  $S_m$  are close to one. The vacuum-metal interfaces now dominate the scattering processes, and the MR actually decreases as  $P$  increases, as can be seen in Figs. 5 and 6. For well formed interfaces, *i.e.*, for  $S_\sigma \approx 1$ , the MR is enhanced by greater surface roughness. For smoother surfaces, as  $P$  approaches one, the current within the Fe layers increases relative to that within the Cu layers. In the extreme case when all three  $P = S_M = S_m = 1$ , the current within each layer for each spin is directly proportional to the density of electrons of that spin in that layer, *i.e.*, to  $|V_{i\sigma}|^{\frac{3}{2}}$ . Under these conditions the size effect disappears, and the MR vanishes. The trilayer becomes a superlattice with no diffusive scattering at the interfaces. This result,  $(\Delta\rho / \rho) = 0$  for  $P = S_M = S_m = 1$ , is valid for any combination of materials and for all values of  $d_i$  and  $\tau$  (or any other of the geometric and bulk parameters of the general model).<sup>21</sup> It follows from the fact that potential scattering of the electrons at the interface is completely microscopically reversible, so that the conductivity of the multilayer is equal to the sum of the bulk conductivities in each layer independently.

In the opposite case, when  $S_{\sigma} = 0$  for all interfaces ( *i.e.*, rough interfaces with completely diffusive scattering),  $(\Delta\rho / \rho) = 0$  once again, this time regardless of the value of  $P$ , the types of materials in the trilayer or the values of any other parameters. In this case there is no coherence between the ferromagnetic layers. The individual layers are uncoupled and the conductance of the trilayer becomes equal to the sum of the conductances of three layers having rough surfaces,  $P = 0$  (this is the case obtained analytically in Ref. 4).

The experimentally observed values of MR in Fe-Cr and Fe-Cu multilayers can be matched by the calculation with a proper choice of the parameters. However, the model in its present form, which considers all of the valence  $s$  and  $d$  electrons as comprising a single band with a single isotropic effective mass, yields effective resistivities  $\rho_{\uparrow\uparrow}$  and  $\rho_{\uparrow\downarrow}$  which are about an order of magnitude smaller than those measured in multilayer structures. The effective resistivities are too small because the model has too many free-electron-like conduction electrons: eight in Fe, six in Cr, and eleven in Cu. Proper consideration must be taken of the fact that, in these metals,  $s$  and  $d$  electrons contribute very differently to the transport properties. The narrow character of the  $d$ -bands has been accounted for in the single-band approach by a single, large, isotropic effective mass, four times larger than the free-electron mass. A better approach to the problem would be to include a realistic band structure with its 12 bands, wide and narrow, as well as the hybridization and spin polarization. Such a treatment would make the calculations much more involved, if not impossible.

Within the confines of a single-band model a simple, natural way to decrease the number of conduction electrons is by reducing the density of the electrons in each layer by a constant scaling factor,  $\gamma$ , independent of the material and the spin of the electron. It should be stressed that the introduction of such a scaling factor does not change the form of the results found above. The number of electrons and the magnetization decreases by a factor of  $\gamma$ . The resistivities  $\rho_{\uparrow\uparrow}$  and  $\rho_{\uparrow\downarrow}$  increase by a factor of about  $\gamma$ , and  $(\Delta\rho / \rho)$  decreases by a factor of about  $\gamma^{\frac{1}{3}}$ . A value of  $\gamma = 8$  was chosen



for making comparisons with experimental data. With this value the number of effective free-electron-like conduction electrons are: 1.00 in Fe, 0.75 in Cr, and 1.38 in Cu. Calculations were able to yield values of the MR and the resistivities,  $\rho_{\uparrow\uparrow}$  and  $\rho_{\uparrow\downarrow}$ , similar to those measured experimentally.

In order to model multilayers, which consist of several layers, the surface parameter  $P$  is taken to be one. Baibich *et al.*<sup>19</sup> found that a multilayer of  $(Fe\ 30\ \text{\AA}/Cr\ 9\ \text{\AA})_{60}$ , prepared by molecular beam epitaxy, had  $(\Delta\rho / \rho) = 0.46$  and an absolute resistivity change of about  $23\ \mu\Omega\ cm$ . With  $P = 1$ ,  $S_m = 0$ ,  $S_M = 1$ ,  $d_F = 30\ \text{\AA}$ ,  $d_s = 9\ \text{\AA}$  and  $\tau = 1 \times 10^{-13}\ s$  values of  $\rho_{\uparrow\uparrow} = 26.1\ \mu\Omega\ cm$  and  $\rho_{\uparrow\downarrow} = 47.6\ \mu\Omega\ cm$  were calculated, which corresponds to  $(\Delta\rho / \rho) = 0.452$  for the MR. When  $P$  is set equal to zero, with the values for the other parameters unchanged, calculations yield  $\rho_{\uparrow\uparrow} = 63.5\ \mu\Omega\ cm$ ,  $\rho_{\uparrow\downarrow} = 74.2\ \mu\Omega\ cm$ , and  $(\Delta\rho / \rho) = 0.144$  for the MR. Experimental values of  $\rho$  are between 20 and  $80\ \mu\Omega\ cm$ . With this choice of  $\gamma$ ,  $\tau$ , and effective mass (*i.e.*, an effective mass of four times the electron mass), the bulk mean free paths are:  $425\ \text{\AA}$  for the majority-spin and  $354\ \text{\AA}$  for the minority-spin electrons in Fe; and  $356\ \text{\AA}$  for the electrons in Cr.

Petroff *et al.*<sup>9</sup> report that a multilayer  $(Fe\ 15\ \text{\AA}/Cu\ 15\ \text{\AA})_{60}$  made by sputtering, had the following characteristics:  $\rho_{\uparrow\uparrow} = 24.8\ \mu\Omega\ cm$ ,  $\rho_{\uparrow\downarrow} = 27.8\ \mu\Omega\ cm$ , and  $(\Delta\rho / \rho) = 0.108$ . With  $P = 1$ ,  $S_m = 0.72$ ,  $S_M = 0.93$ ,  $d_F = d_s = 15\ \text{\AA}$  and  $\tau = 1 \times 10^{-13}\ s$  values of  $\rho_{\uparrow\uparrow} = 24.1\ \mu\Omega\ cm$  and  $\rho_{\uparrow\downarrow} = 27.0\ \mu\Omega\ cm$  were calculated, which correspond to  $(\Delta\rho / \rho) = 0.107$ . Here the bulk mean free paths are:  $425\ \text{\AA}$  for the majority-spin and  $354\ \text{\AA}$  for the minority-spin electrons in Fe; and  $433\ \text{\AA}$  for the electrons in Cr.

Calculations predict that a trilayer with completely diffuse scattering at the surface,  $P = 0$ , and with atomically clean interfaces,  $S_M = S_m = 1$ , can have a sizable MR (caused by the "channeling effect" discussed above) when the density of spin-up and/or the spin-down electrons is greater in the spacer layer than the corresponding

ones in the outer *ferromagnetic* layers. For example in Fe-Cu, where the density of electrons is greatest in the Cu layer, the results  $\rho_{\uparrow\uparrow} = 10.1 \mu\Omega \text{ cm}$ ,  $\rho_{\uparrow\downarrow} = 16.3 \mu\Omega \text{ cm}$ , and  $(\Delta\rho / \rho) = 0.382$  were found when  $\gamma = 8$ ,  $d_F = d_s = 10\text{\AA}$  and  $\tau = 5 \times 10^{-13}\text{s}$ .

As clearly seen in Figs. 4 and 5, a large MR requires, in general, a large difference in interface scattering for the different spins. When  $S_M = S_m$  (with some exceptions, see Fig. 5 and the size effect discussed above) the MR is found to be not more than a few percent. Therefore a large MR cannot be explained as being caused solely by different densities of electrons with different spins, which vary from layer to layer. What is required is a spin imbalance *and* a spin-dependent scattering mechanism at the interface, *i.e.*,  $S_M \neq S_m$ . When such a spin-dependent scattering mechanism exists, for example when magnetic impurities are present at the interfaces, the MR is profoundly influenced by spatial variations in the density of electron spins. This is the main cause of the GMR effect in ferromagnetic multilayers.

## E. References for Chapter III

- 1 J. Barnaś, A. Fuss, R. E. Camley, P. Grünberg, and W. Zinn, *Phys. Rev. B* **42**, 8110 (1990).
- 2 R. E. Camley and J. Barnaś, *Phys. Rev. Lett.* **63**, 664 (1989).
- 3 K. Fuchs, *Proc. Cambridge Philos. Soc.*, **34**, 100 (1938).
- 4 E. H. Sondheimer, *Adv. Phys.*, **1**, 1 (1952).
- 5 E. C. Stoner, *Proc. Roy. Soc. London A*, **165**, 372 (1938).
- 6 P. Baumgart, B. A. Gurney, D. R. Wilhoit, T. Nguyen, B. Dieny, and V. Speriosu, *J. Appl. Phys.* **69**, 4972 (1991).
- 7 S. S. P. Parkin, N. More, and K. P. Roche, *Phys. Rev. Lett.* **64**, 2304 (1990).
- 8 G. G. Cabrera, and L. M. Falicov, *phys. stat. sol. (b)* **61**, 539 (1974); **62**, 217 (1974).
- 9 F. Petroff, A. Barthélémy, D. H. Mosca, D. K. Lottis, A. Fert, P. A. Schroeder, W. P. Pratt Jr., and R. Loloee, *Phys. Rev. B*, **44**, 5355 (1991).
- 10 S. S. P. Parkin, *Phys. Rev. Lett.* **67**, 3598 (1991).
- 11 P. M. Levy, S. Zhang, A. Fert, *Phys. Rev. Lett.* **65**, 1643 (1990).
- 12 It should be noted that the magnetoresistance ( $\Delta\rho / \rho$ ), as defined, is positive when it refers to what is usually called a negative MR. Only cases with  $(\Delta\rho / \rho) \geq 0$  are considered in this contribution. Situations where  $(\Delta\rho / \rho) < 0$  (ordinary magnetoresistance) may occur in the model when the relaxation times  $\tau_{i\sigma}$  for spin  $\sigma$  take different values in different layers  $i$ . Such cases are not discussed here.
- 13 A. Fert and I. A. Campbell, *J. Phys. F: Metal Phys.* **6**, 849 (1976); I. A. Campbell and A. Fert, in *Ferromagnetic Materials*, edited by E. P. Wohlfarth (North-Holland, Amsterdam, 1982), Vol. 3, p. 769.

- 14 For the sake of simplicity the formulas for the reflection and transmission coefficients are written exclusively for the case in which the effective masses are the same on both sides of the interface, *i.e.*,  $m_{i\sigma} = m_{j\sigma}$ .
- 15 See for instance E. Hecht and A. Zajac, *Optics* (Addison-Wesley, Menlo Park, 1974) p. 91.
- 16 It should be noted that the function  $\tilde{F}_{i\sigma}(u)$  has an analytic form and can be written as a closed expression. The expression takes a somewhat simpler form for long mean free paths. It, however, contains in all instances the transmission and reflection coefficients and, when inserted in Eq. (10), it yields expressions too complicated to be evaluated analytically. For the sake of brevity the expression is not included here.
- 17 The observed maxima in the magnetoresistance shown in Fig. 9 are caused by the fact that most of the effect is caused, as discussed below, by a channeling effect -- within the spacer layer -- of the spin for which  $S = 1$ . As  $d_s \rightarrow 0$  the contribution of the "channel" to the current becomes smaller, the electrons of both spins are subject in all configurations to the strong diffuse scattering of the free surfaces, and the magnetoresistance decreases with decreasing  $d_s$ .
- 18 A. Chaiken, T. M. Tritt, D. J. Gillespie, J. J. Krebs, P. Lubitz, M. Z. Harford, and G. A. Prinz, *J. Appl. Phys.*, **69**, 4798 (1991).
- 19 M. N. Baibich, J. M. Broto, A. Fert, F. Nguyen Van Dau, F. Petroff, P. Etienne, G. Creuzet, A. Friederich, and J. Chazelas, *Phys. Rev. Lett.* **61**, 2472 (1988).
- 20 It should be noted that the channeling effect, *per se*, does not necessarily lead to a large magnetoresistance, as can be seen from the case shown in Fig. 6 [ $(\Delta\rho/\rho) = 0$  for  $P = S_M = S_m = 1$ ]. The large magnetoresistance appears when, in the parallel arrangement, there is channeling for *only one spin* and diffuse interface scattering for the other one. In that case, in the antiparallel arrangement, both spins partake in the diffuse scattering, and the long electron trajectories (and

the channeling) are lost.

- <sup>21</sup> The particular result  $(\Delta\rho/\rho) = 0$  is valid for  $P = S_M = S_m = 1$  and for any combination of geometric and intrinsic metal parameters as long as  $\tau_{i\sigma} = \tau_\sigma$ , i.e., the relaxation times for each spin are *the same* in all layers of the system.

## F. Figures for Chapter III

### Figure 1

Schematic diagram of the ferromagnetic-normal-ferromagnetic metallic trilayer. Axes and thicknesses are defined.

### Figure 2

Schematic diagrams of the scattering processes at (a) the vacuum-metal free surface and (b) the metal-metal interface. The parameters  $P$  and  $S_{\sigma}$  define the fractions controlled by the potentials. In (b)  $S_{\sigma} R$  is the probability of specular scattering;  $S_{\sigma} T$  is the probability of transmission (refraction) into the other metal. The isotropic, diffuse scattering parts are  $(1-P)$  and  $(1-S_{\sigma})$ , respectively.

### Figure 3

Schematic diagrams of the potentials for the spin  $\uparrow$  and spin  $\downarrow$  electrons in the parallel ( $\uparrow\uparrow$ ) and the antiparallel ( $\uparrow\downarrow$ ) configurations of an Fe-Cu-Fe trilayer.

### Figure 4

The region in three-dimensional parameter space  $(P, S_M, S_m)$  where  $(\Delta\rho / \rho) > 0.2$  for the parameters corresponding to Fe-Cr and  $d_F = d_s = 10 \text{ \AA}$ , and  $\tau = 5.0 \times 10^{-13} \text{ s}$ . The three parameters vary between 0 and 1.

### Figure 5

The region in three-dimensional parameter space  $(P, S_M, S_m)$  where  $(\Delta\rho / \rho) > 0.2$  for the parameters corresponding to Fe-Cu and  $d_F = d_s = 10 \text{ \AA}$ , and  $\tau = 5.0 \times 10^{-13} \text{ s}$ . The three parameters vary between 0 and 1.

### Figure 6

Variation of  $(\Delta\rho / \rho)$  as a function of  $P$  for the parameters of Fe-Cr,  $\tau = 5.0 \times 10^{-13} \text{ s}$ ,  $d_F = d_s = 10 \text{ \AA}$  and various values of  $S_M$ , and  $S_m$ .

**Figure 7**

Variation of  $(\Delta\rho / \rho)$  as a function of  $S_m$  for the parameters of Fe-Cr,  $\tau = 5.0 \times 10^{-13} s$ ,  $d_F = d_s = 10 \text{ \AA}$  and four different values of  $S_M$ , and  $P$ : (1) chain dashed curve  $S_M = 1$  and  $P = 0.5$ ; (2) dashed curve  $S_M = 1$  and  $P = 1$ ; (3) chain dotted curve  $S_M = 0.5$  and  $P = 1$ ; and (4) solid curve  $S_M = 0$  and  $P = 1$ .

**Figure 8**

Variation of  $(\Delta\rho / \rho)$  as a function of  $d_F$  for the parameters of Fe-Cr,  $d_s = 10 \text{ \AA}$ ,  $\tau = 5.0 \times 10^{-13} s$  and three different values of  $S_M$ ,  $S_m$  and  $P$ : (1) chain dotted curve  $S_M = S_m = 0.8$  and  $P = 0$ ; (2) dashed curve  $S_M = S_m = 0.8$  and  $P = 1$ ; and (3) solid curve  $S_M = S_m = 1$  and  $P = 0$ .

**Figure 9**

Variation of  $(\Delta\rho / \rho)$  as a function of  $d_s$  for the parameters of Fe-Cr,  $d_F = 10 \text{ \AA}$ ,  $\tau = 5.0 \times 10^{-13} s$  and three different values of  $S_M$ ,  $S_m$  and  $P$ : (1) chain dotted curve  $S_M = S_m = 0.9$  and  $P = 1$ ; (2) dashed curve  $S_M = 0.5$ ,  $S_m = 1$  and  $P = 0.5$ ; and (3) solid curve  $S_M = 1$ ,  $S_m = 0$  and  $P = 0$ .

**Figure 10**

Variation of  $(\Delta\rho / \rho)$  as a function of  $\tau$  for the parameters of Fe-Cr,  $d_s = d_F = 10 \text{ \AA}$ ,  $P = 1$ , and three different values of  $S_M$  and  $S_m$ : (1) chain dotted curve  $S_M = 0$  and  $S_m = 0.7$ ; (2) dashed curve  $S_M = 0.5$  and  $S_m = 1$ ; and (3) solid curve  $S_M = 1$  and  $S_m = 0$ .

**Figure 11**

Distribution of the in-plane current ( $J_x$ ) (plotted in arbitrary units) over the thickness of an Fe-Cr-Fe trilayer. The contribution to the current from the spin-up and the spin-down electrons is plotted in the parallel and the antiparallel configuration of the Fe-layer magnetic moments: (1) solid curve is the ( $\downarrow PI$ )-electrons; (2) chain dotted curve is the ( $\uparrow PI$ )-electrons; (3) dashed curve is the ( $\downarrow An$ )-electrons; (4) chain dashed curve is the ( $\uparrow An$ )-electrons. The values of the parameters are:  $\tau = 5.0 \times 10^{-13}$ ,

$$d_F = d_s = 10 \text{ \AA}, S_M = 0, S_m = 1, \text{ and } P = 0.5.$$

### Figure 12

Distribution of the in-plane current ( $J_x$ ) (plotted in arbitrary units) over the thickness of an Fe-Cr-Fe trilayer. The contribution to the current from the spin-up and the spin-down electrons is plotted in the parallel and the antiparallel configuration of the Fe-layer magnetic moments: (1) solid curve is the ( $\downarrow PI$ )-electrons ; (2) chain dotted curve is the ( $\uparrow PI$ )-electrons ; (3) dashed curve is the ( $\downarrow An$ )-electrons; (4) chain dashed curve is the ( $\uparrow An$ )-electrons. The values of the parameters are:  $\tau = 5.0 \times 10^{-13}$ ,  $d_F = d_s = 10 \text{ \AA}$ ,  $S_M = 1$ ,  $S_m = 0$ , and  $P = 0.5$



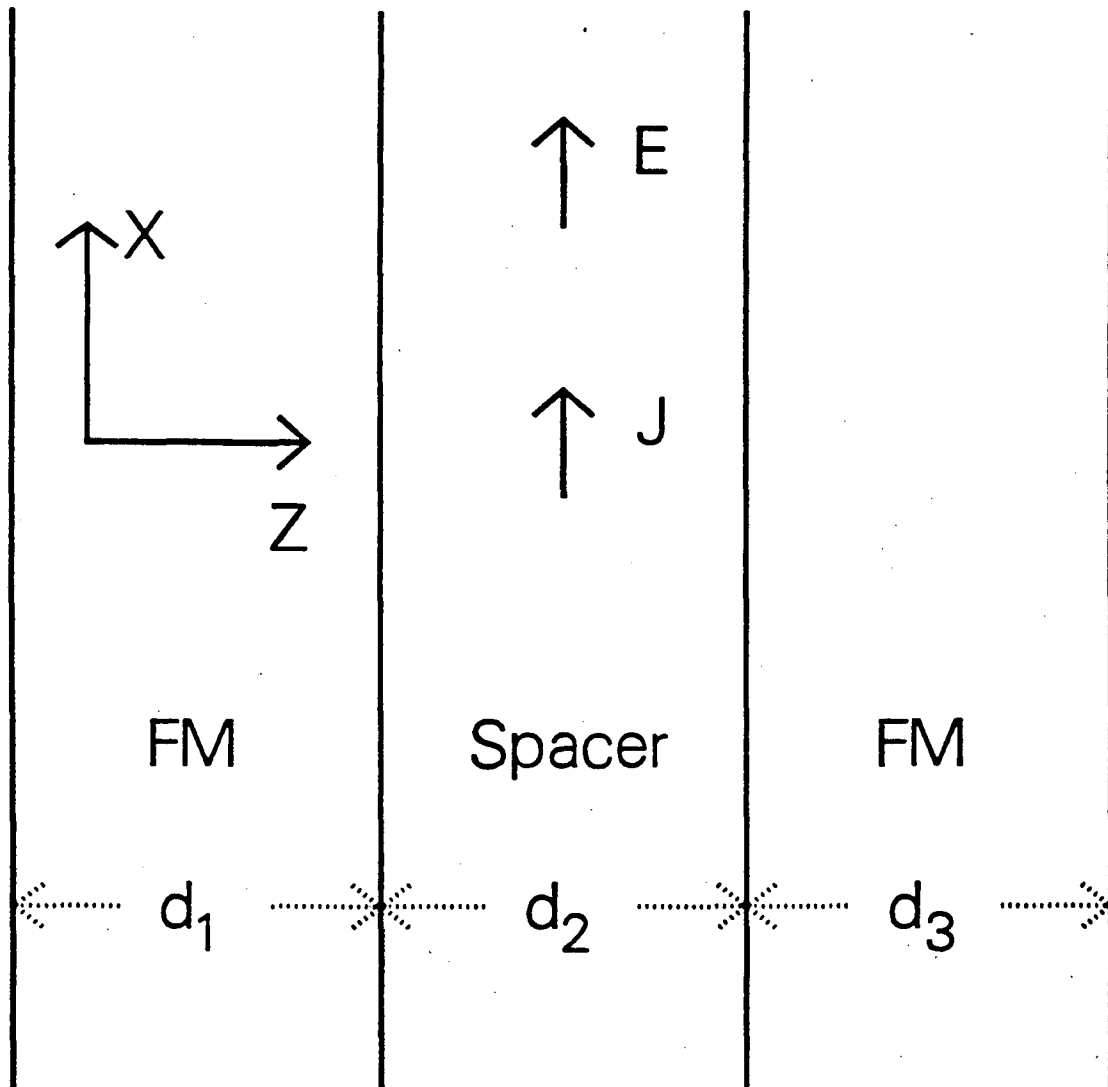


Fig. 1

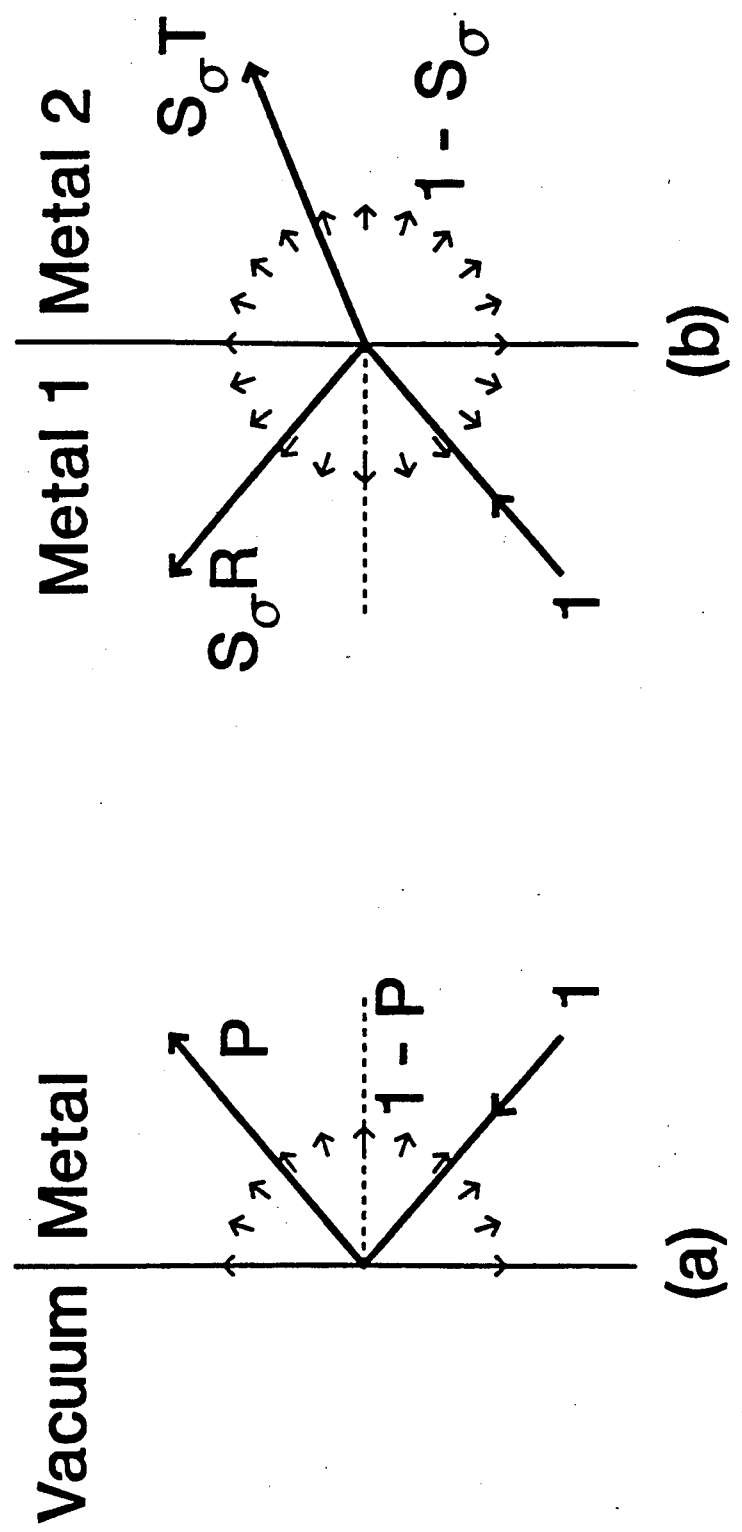


Fig. 2

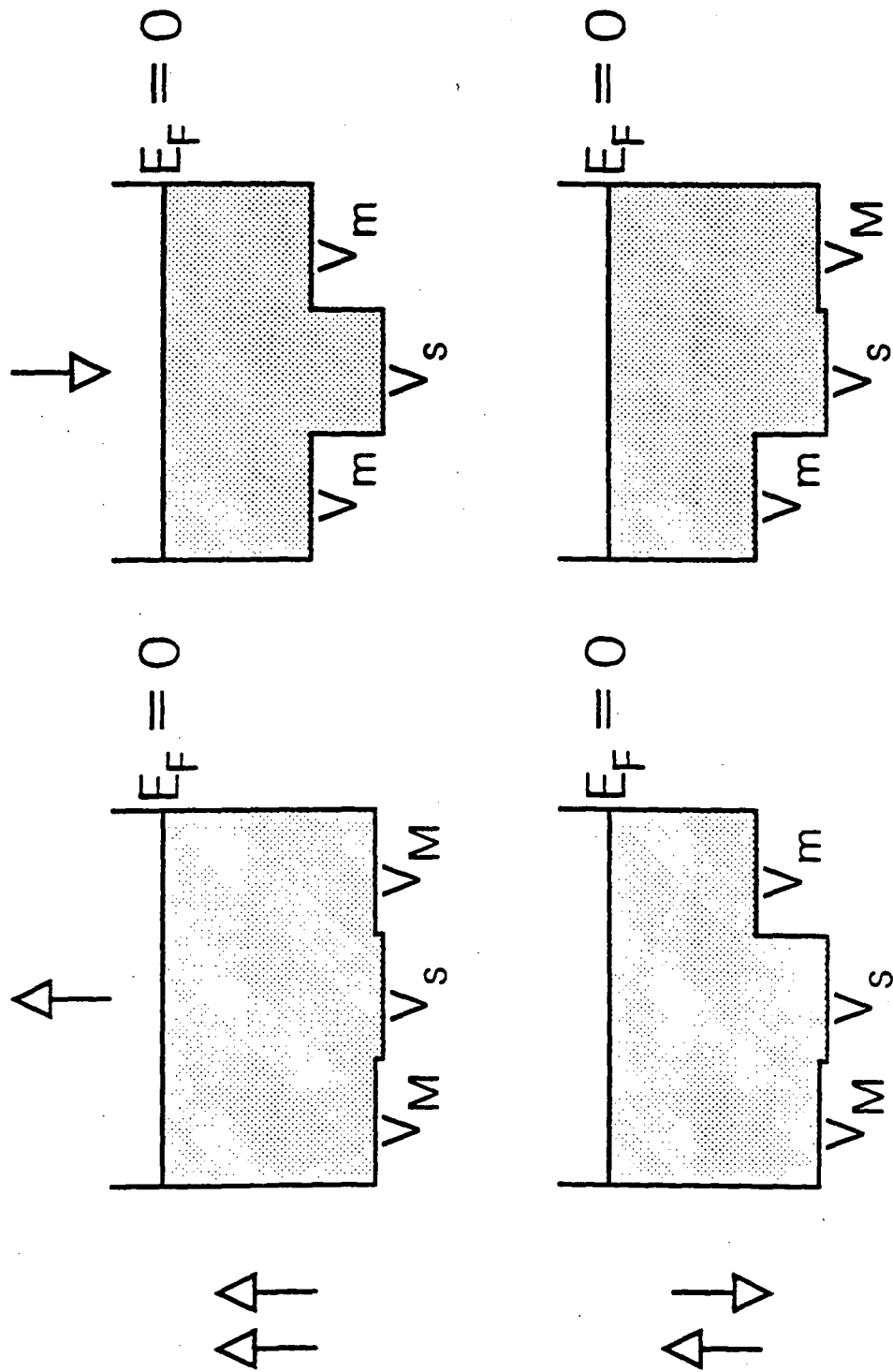


Fig. 3

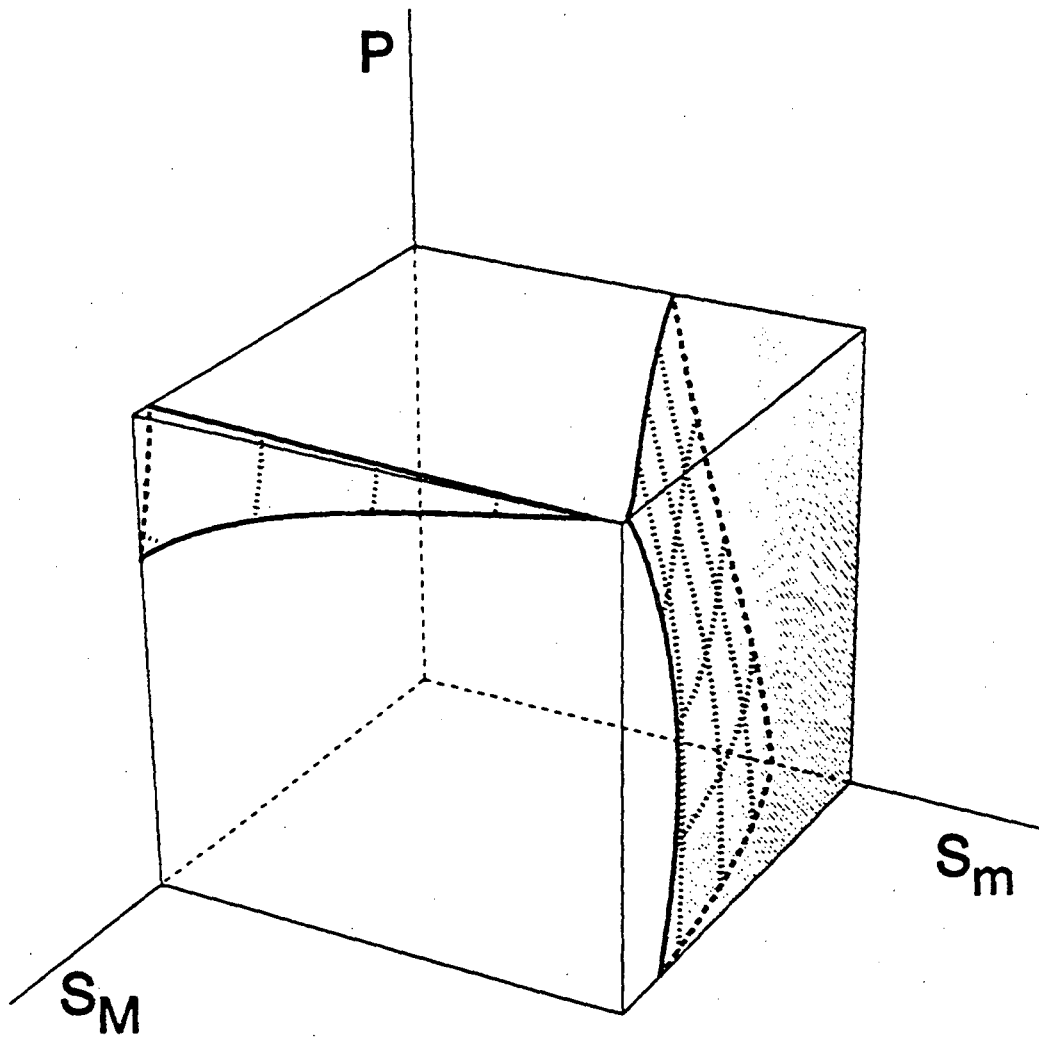


Fig. 4

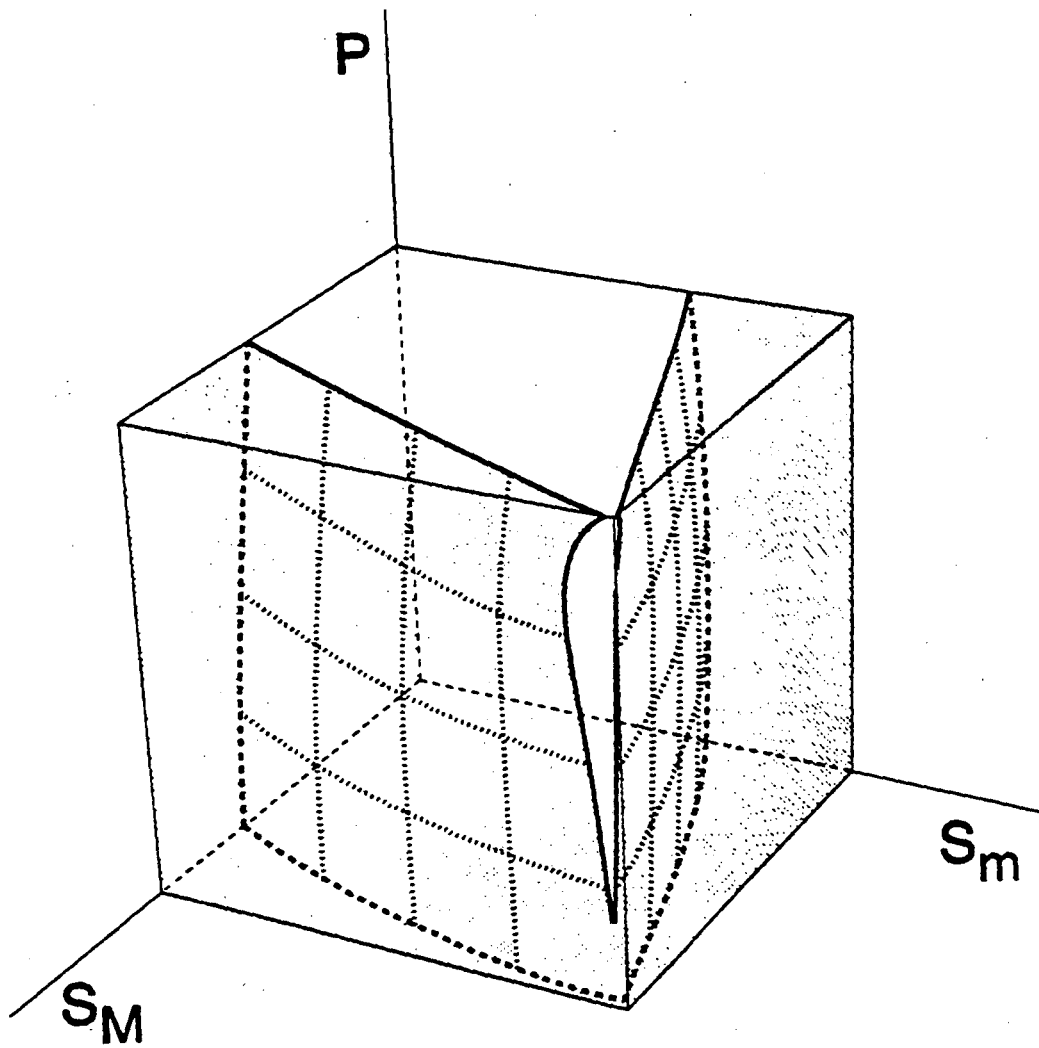


Fig. 5

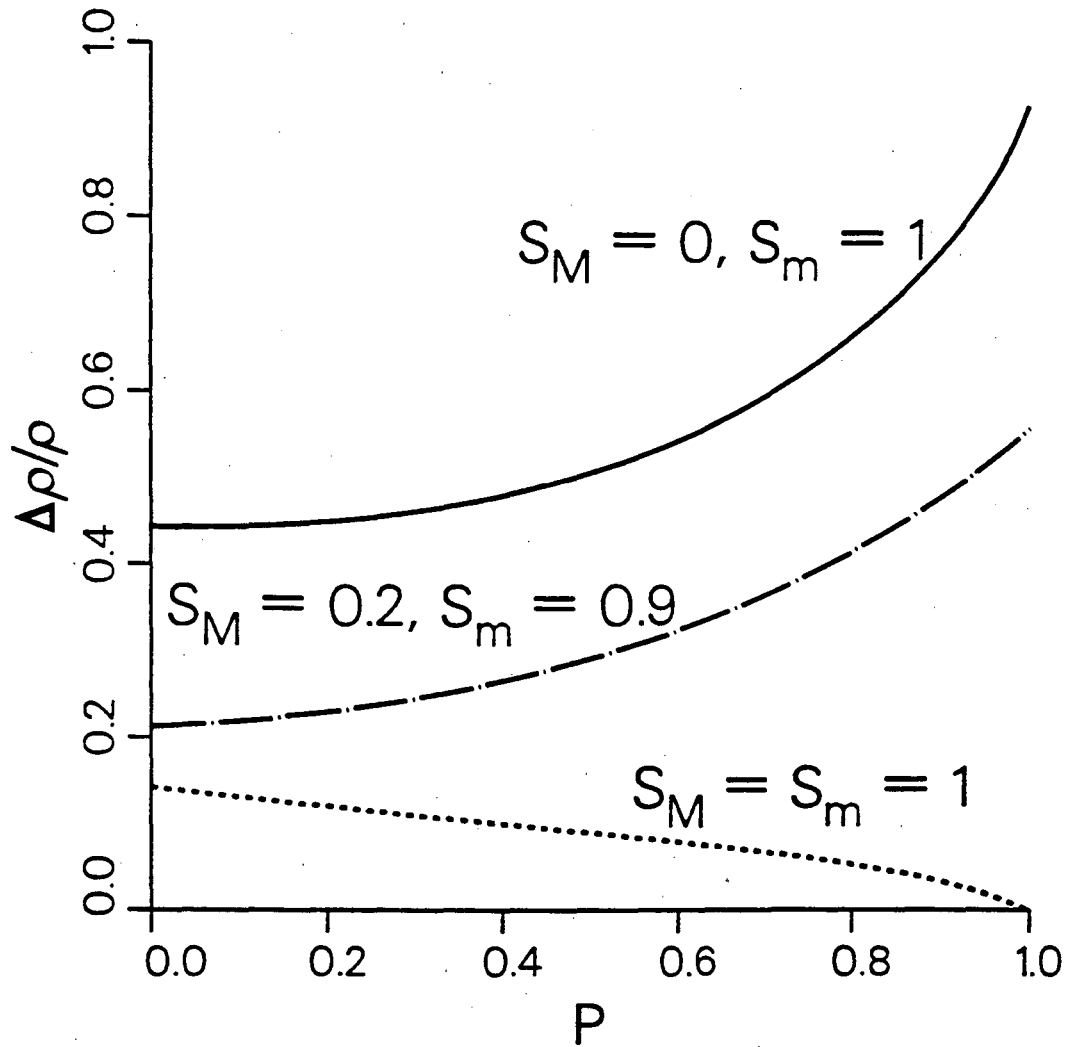


Fig. 6

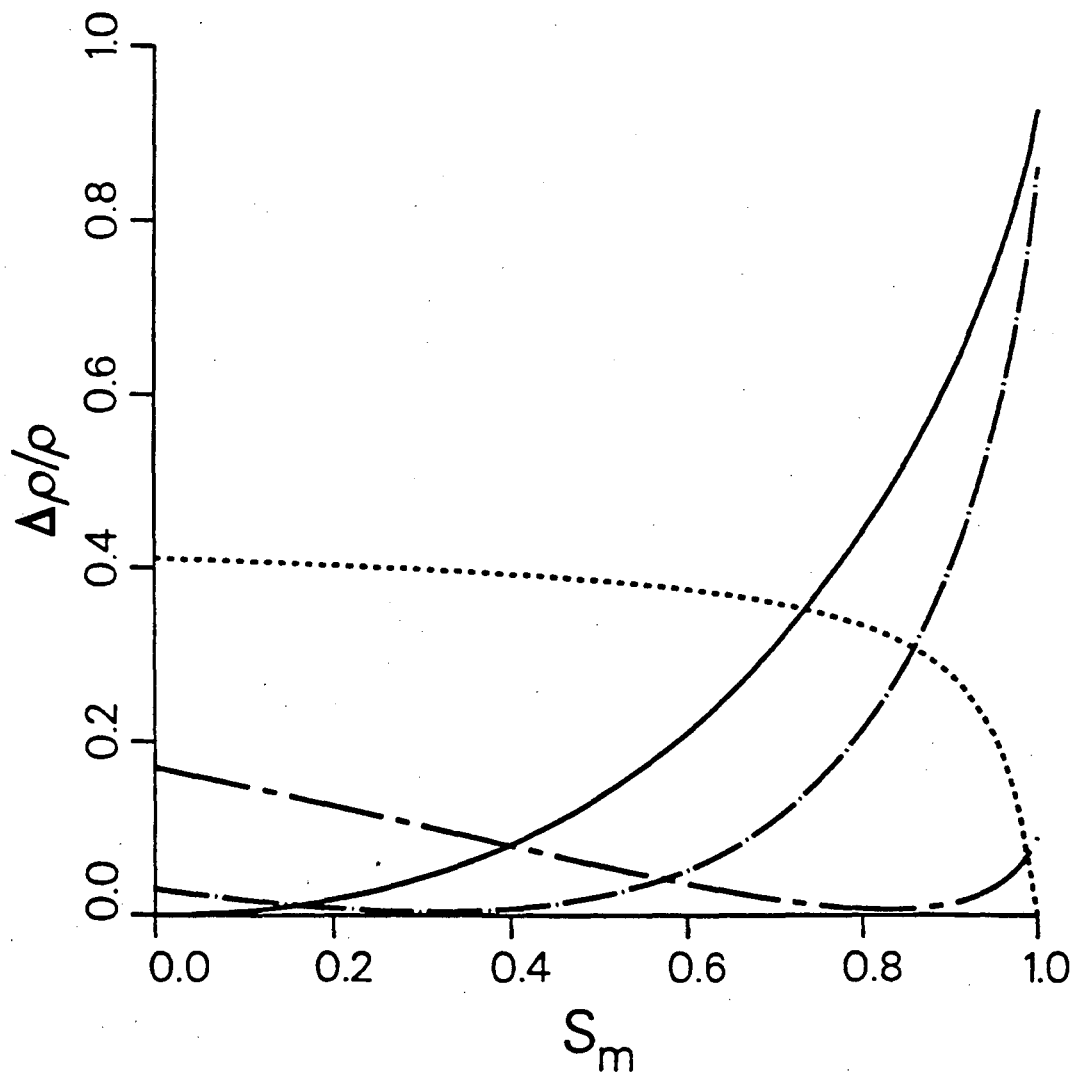


Fig. 7

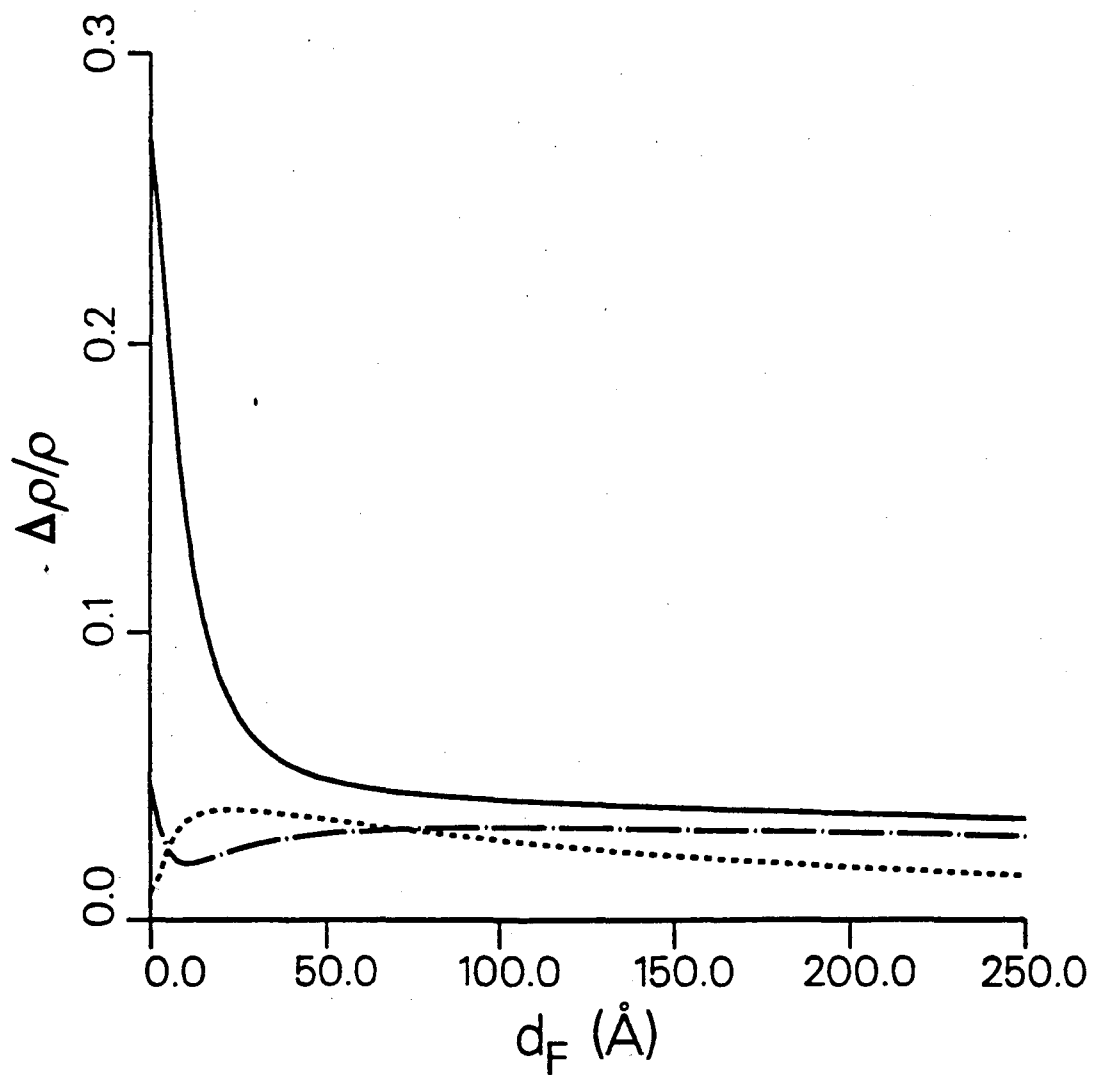


Fig. 8



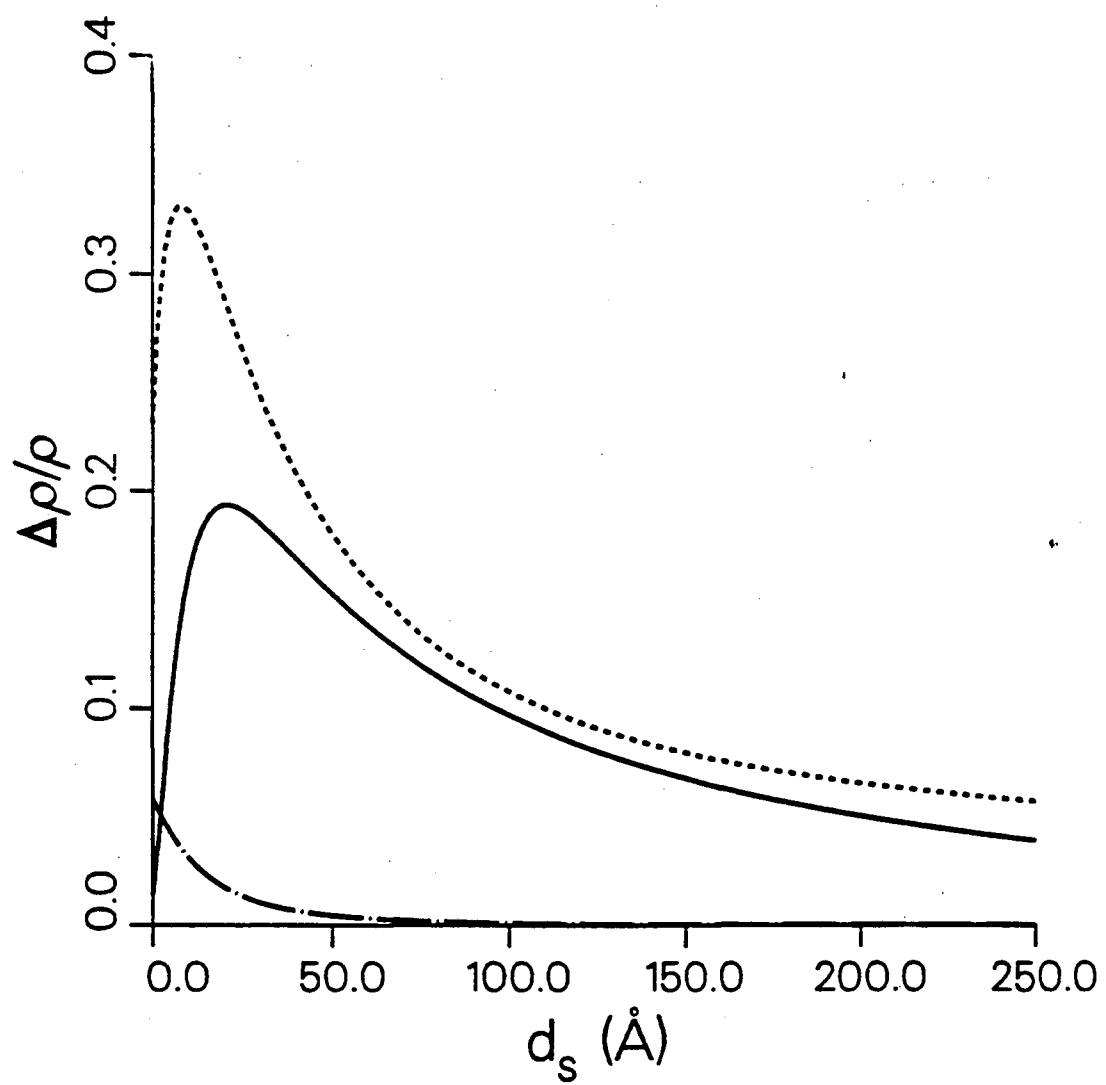


Fig. 9

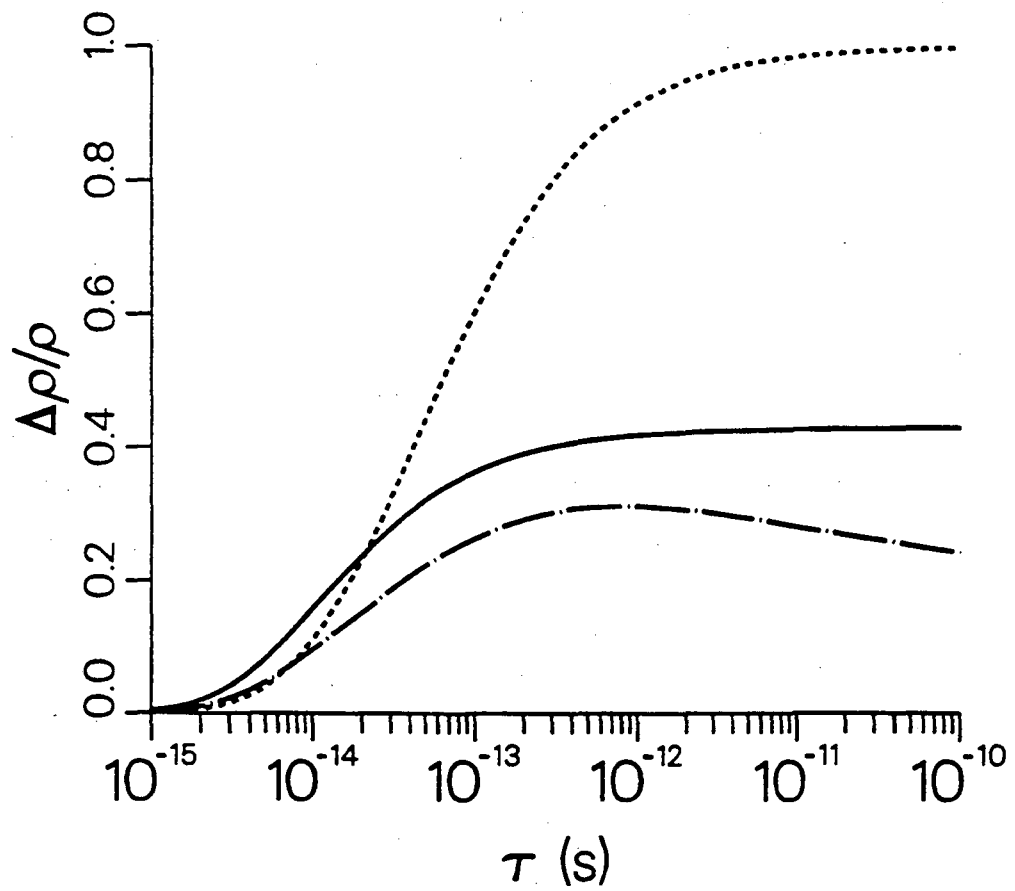


Fig. 10

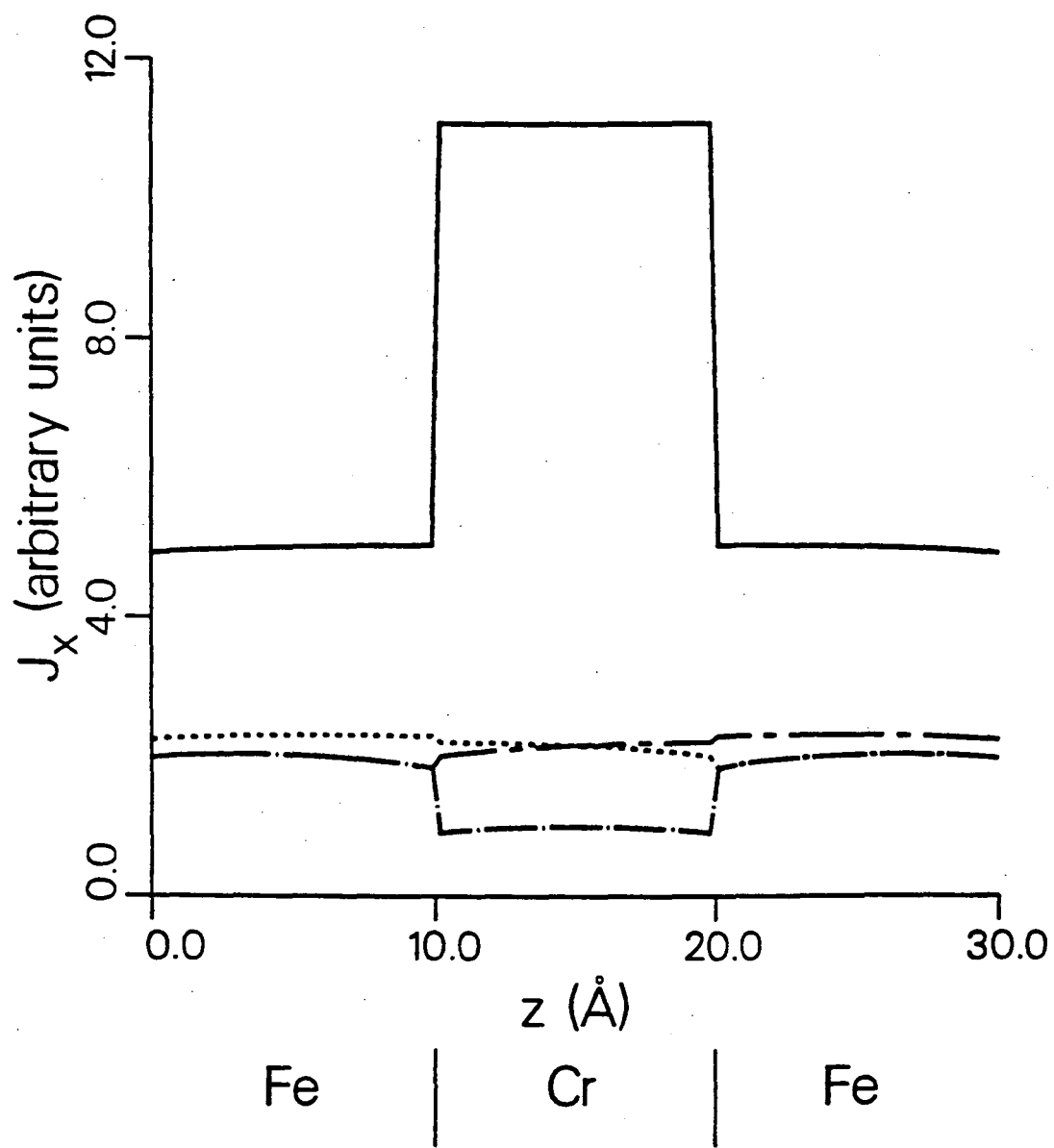


Fig. 11

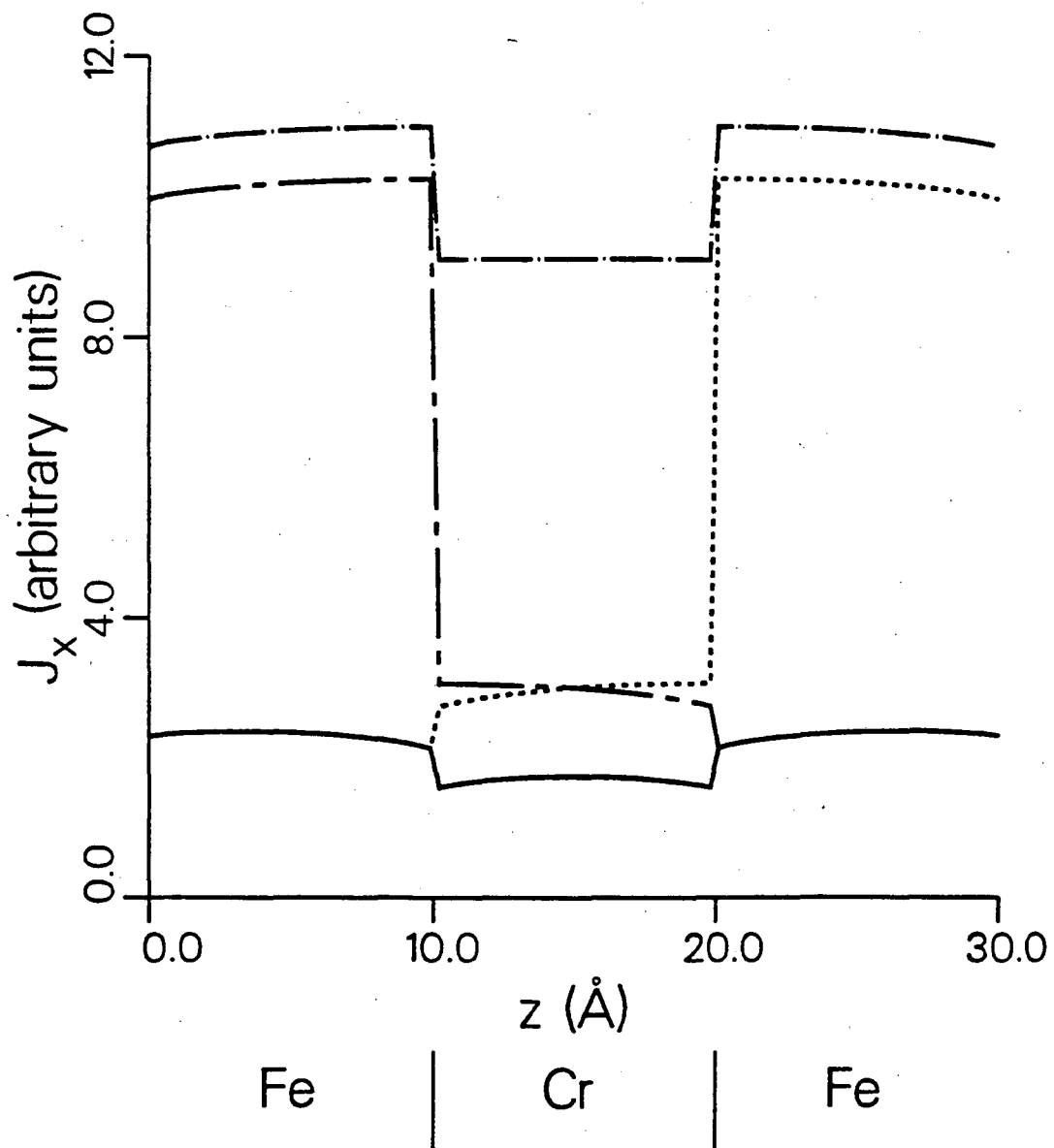


Fig. 12

## Chapter IV: Effects of Interfacial Roughness on the Magnetoresistance of Magnetic Metallic Multilayers

### A. Introduction

A precise description of the character of the interfaces and the resulting spin-dependent scattering mechanisms in magnetic multilayers is currently unavailable either from experiment or from theory. There are several possibilities, which depend on the growth conditions and the materials used during fabrication. Interdiffusion may be present and intermix the elements within a region around each of the interfaces. By contrast there may be regions, laterally along the interfaces, with little interdiffusion but with variations in thickness, *i.e.*, geometrical roughness. The variations in thickness may vary in a random manner with little lateral coherence, or there may be steps and terraces with considerable correlations. In addition there may be chemical impurities at the interfaces that may have been introduced, intentionally or unintentionally. In principle both the position and the type of atoms present at the interfaces can influence the spin-dependent scattering of the conduction electrons.

In this chapter I present an extension of the semiclassical (Boltzmann) approach of chapter III, that looks at how particular changes in the structure and the chemical composition of the interfaces influence the interfacial spin-dependent scattering mechanism and, more importantly, the MR. Specifically I consider how the MR is affected by: 1) variations in the size of the geometrical roughness, the mean square deviation of the surfaces from being atomically flat, with no lateral coherence; 2) the presence of correlated (quasi-periodic) roughness; and 3) the chemical composition of the interface. With few exceptions, the simple rule that emerged in chapter III does not change. That is, in order to have a GMR, it is advantageous to have a large asymmetrical spin-dependent interfacial scattering mechanism, with one spin component largely scattered diffusely, and the other mainly scattered coherently by the potentials. What emerges from this study is an understanding of how different qualities of the

interfaces leads to asymmetrical spin-dependent scattering. In some cases the interplay of the different aspects of the interfaces I mention above may enhance the asymmetrical nature of the interfacial spin-dependent scattering and hence the MR; in other cases it may decrease the asymmetry and correspondingly suppress the MR.

As in chapter III -- an extension of the Fuchs-Sondheimer theory<sup>1,2</sup> and Camley and Barnas's approach<sup>3,4</sup> to multilayers -- I use a Stoner description<sup>5</sup> of the itinerant F layers; there are different potentials for the majority and minority spins. Band-structure and electron-density effects are included by means of constant metal- and spin-dependent potentials, and an isotropic effective mass for each spin in each layer. As an electron traverses an F-S interface the potential difference between the layers causes it to be partially reflected, with a probability  $R$ , and partially transmitted (refracted) into the other layer, with probability  $T$ . The coefficients  $R$  and  $T$  are determined by quantum-mechanical matching of the wave functions at the interface, and found in general to depend on the Fermi velocity, the orientation of the spin, and the angle of incidence. In addition a single spin-dependent parameter  $S$  is introduced at each interface to characterize the fraction of electrons which are coherently scattered by the potential. The remainder,  $(1-S)$ , is assumed to be diffusely scattered back to the equilibrium distribution. In chapter III it was assumed that  $S$  was independent of the angle and direction of incidence. It represents the averaged effects of any spin-dependent interfacial scattering mechanisms present at the interfaces not caused by the potential difference. In other words, it represented the average effect of the structural and chemical imperfections at the interfaces. In this chapter I show that it is possible to quantify specific information about the interfaces by allowing  $S$  to depend more generally on the angle and direction of incidence, and the spin orientation.

Section B contains a discussion of the interfacial scattering parameters,  $S$ . In section C results are presented for various interfaces in  $(\text{Fe/Cr})_n$  and  $(\text{Fe/Cu})_n$  multilayers. Section D contains the conclusions.

## B. Interface Parameters

When there is little interdiffusion, an interface separating a spacer and a ferromagnetic layer can be described by a function  $z = z_{ij} + \zeta(x,y)$ , where  $z$  is the coordinate normal to the layers and  $z_{ij}$  is the average coordinate of the interface,  $z_{1,2} = d_1$  or  $z_{2,3} = d_1 + d_2$ . In general the specific form of the function  $\zeta$  for a given interface is unknown: a statistical description of an interface is appropriate. A common approach<sup>6-9</sup> is to consider  $\zeta$  as a random variable with a gaussian distribution

$$w(\zeta) = \frac{1}{\eta\sqrt{2\pi}} e^{-\zeta^2/2\eta}$$

that is independent of position in the  $(x,y)$ -plane, so that

$$\eta = \sqrt{\langle \zeta(x,y)^2 \rangle}$$

and that the in-plane correlation function between two points in the interface is

$$C(|\mathbf{r}_1 - \mathbf{r}_2|) \equiv \langle \zeta(\mathbf{r}_1) \zeta(\mathbf{r}_2) \rangle / \langle \zeta(\mathbf{r}_1) \rangle^2 = e^{-|\mathbf{r}_1 - \mathbf{r}_2|^2/L^2}$$

where  $\mathbf{r}_i = x_i \hat{\mathbf{x}} + y_i \hat{\mathbf{y}}$  and  $L$  is the correlation length. For a finite nonzero  $L$ , the boundary conditions, Eq. (6) in chapter III, must be replaced by a set of integral equations, since the diffuse scattering makes a contribution to the current. In the limit as  $L$  goes to zero the diffuse scattering no longer contributes to the current, Eq. (6) in chapter III is valid,<sup>10</sup> and the function  $S_{ij;i;\sigma}$  takes the form (see Refs. 6-7 for a derivation and discussion):

$$S_{ij;i;\sigma} = S_\sigma \exp \left[ -4\eta^2 (k_{i\sigma} \cos\theta_i)^2 \right] ; \quad (1)$$

$$S_{ij;j;\sigma} = S_\sigma \exp \left[ -\eta^2 (k_{i\sigma} \cos\theta_i - k_{j\sigma} \cos\theta_j)^2 \right] .$$

Here  $k_{i\sigma}$  is related to the magnitude of the velocity of an electron in layer  $i$  with spin  $\sigma$ , given by  $k_{i\sigma} = m_{i\sigma} v_{i\sigma} / \hbar$ . I have inserted the prefactor  $S_\sigma$  in Eq. (1) to include, in an averaged way, the scattering effects from impurities, interdiffusion, band structure, correlation, etc., caused neither by potential difference at the interface nor by

geometrical roughness.<sup>11</sup>

The presence of roughness causes spin-dependent scattering at the interfaces since for electrons at the Fermi energy in the ferromagnetic layers,  $i = F$ , the  $k_{i\sigma}$  have magnitudes that depend on the spin  $\sigma$ . From Eq. (1) the diffuse scattering is considerably larger for electrons impinging upon the interface in directions close to the normal. Grazing-angle electrons are less effectively scattered, and they tend to be almost completely internally reflected.

If the surface, on the other hand, has strong lateral correlations, with typical correlation lengths of the order of the Fermi wavelength, quantum-mechanical coherence effects may take place. In particular, the presence of a "periodic" potential that satisfies Bragg's condition is responsible for electron-diffraction phenomena. Roughness at interfaces with strong in-plane spatial correlations and with typical lengths of, say, the Fermi wavelength of the majority-spin electrons, will cause these electrons -- which match Bragg's diffraction condition -- to be coherently scattered onto the Bragg-peak directions, and removed from the reflected and transmitted beams more efficiently. These Bragg-diffracted electrons do not contribute effectively to the conduction processes. A given "cone" of electrons of a given spin is thus removed, at the interface, from the current-carrying stream.<sup>12</sup> For strongly peaked in-plane correlation lengths this process may affect one spin and not the other.

Bragg's condition follows from the conservation of the electron total energy and crystal momentum in the plane of the interface. An electron with  $k_{i\sigma}$  in layer  $i$ , with spin  $\sigma$ , incident on an interface separating the  $i$  and  $j$  layers is predominantly diffracted into those directions  $k_{l\sigma}$  (where  $l = i$  or  $j$ ) that satisfy<sup>13</sup>

$$|k_{i\sigma_{||}}|^2 + k_{i\sigma_{\perp}}^2 = |k_{l\sigma_{||}}|^2 + k_{l\sigma_{\perp}}^2 + \frac{2 \cdot m}{\hbar^2} (V_{l\sigma} - V_{i\sigma}) \quad (2)$$

$$k_{l\sigma_{||}} = k_{i\sigma_{||}} + K_{ij} \quad (3)$$

Here  $K_{ij}$  is any (two-dimensional) reciprocal lattice vector in the plane of the interface (say the  $x,y$ -plane) that is related to the real-space quasi-periodic roughness of



the ( $ij$ ) interface. A pictorial representation of Bragg's condition in reciprocal space is shown in Fig. 1. Because of lack of periodicity in the  $z$ -direction, there is conservation of crystal-momentum only in the  $x, y$ -plane, as stated in Eq. (3). The "Bragg spots" (three-dimensional reciprocal lattice vectors) are in this case "Bragg rods", lines parallel to  $z$  (perpendicular to the interface) that pass through each point  $\mathbf{K}_{ij}$ . In Fig. 1 these rods are drawn along with two hemispheres centered at the origin of  $\mathbf{k}_{i\sigma}$ . The radius of each hemisphere follows from Eq. (2) and depends on whether the electrons are scattered into layer  $i$  (backward scattering) or layer  $j$  (forward scattering). Possible  $\mathbf{k}_{l\sigma}$  (*i.e.*, those that satisfy the equations above) are drawn with the tail at the center of the two hemispheres and the head at those points where a hemisphere intersects one rod. Two cases,  $V_{i\sigma} < V_{j\sigma}$  and  $V_{i\sigma} > V_{j\sigma}$  are illustrated in Fig. 1. In both cases shown a reflected R and a transmitted T beam occur. In addition the angle of incidence was chosen in each case such that an additional diffracted beam D just appears. This has the effect of reducing the intensity of the reflected and the transmitted beams. The threshold angle of incidence,  $\theta_t$ , at which a diffracted peak appears is given by

$$|\mathbf{k}_{i\sigma}| \sin(\theta_t) + k_{max,\sigma} = \kappa_{ij} \quad ,$$

where  $\kappa_{ij}$  is the smallest nonzero reciprocal lattice vector and  $k_{max,\sigma}$  is equal to the maximum value of the magnitudes of the two vectors  $\mathbf{k}_{i\sigma}$  and  $\mathbf{k}_{j\sigma}$ . In this equation an average was taken over the azimuthal component of  $\mathbf{k}_{i\sigma}$ , assuming a polycrystalline interface as in most common situations. The removal of electrons from the reflected and the transmitted beams can be taken into account by assuming that in the range of angles,  $\theta > \theta_t$ , the corresponding functions  $S_{ij;l;\sigma}$  are substantially reduced. This can be achieved by multiplying  $S_{ij;l;\sigma}$  by a factor  $0 \leq c_{ij;l;\sigma} \leq 1$ .

A suitable function, used in the calculations is

$$\begin{aligned} c_{ij;l;\sigma} &= 1, \quad \text{if } \kappa_{ij} > k_{i,\sigma} + k_{max,\sigma} \quad ; \\ c_{ij;l;\sigma} &= 1, \quad \text{if } \kappa_{ij} \leq k_{i,\sigma} + k_{max,\sigma} \quad \text{and } \theta < \sin^{-1} \left[ \frac{\kappa_{ij} - k_{max,\sigma}}{k_{i,\sigma}} \right] \quad ; \end{aligned} \quad (4)$$

$$c_{ij;l;\sigma} = (1-\alpha), \quad \text{if } \kappa_{ij} \leq k_{i,\sigma} + k_{max,\sigma} \text{ and } \theta \geq \sin^{-1} \left[ \frac{\kappa_{ij} - k_{max,\sigma}}{k_{i,\sigma}} \right] ;$$

here  $\theta$  is the angle of incidence at the  $(ij)$  interface,  $0 \leq \alpha \leq 1$  depends on the strength of the interface quasi-periodic potential, and the factor  $c$  is independent of the emerging layer  $l$ . If the roughness in the interface is characterized by more than one typical wavevector,  $\mathbf{K}_{ij}$ , Eq. (4) can be modified accordingly.

### C. Results

Here results of the MR for  $(\text{Fe/Cr})_n$  and  $(\text{Fe/Cu})_n$  multilayers with different types of interfaces are presented.

Shown in Fig. 2 are MR results for  $(\text{Fe/Cr})_n$  superlattices with interfacial scattering given by Eq. (6) in chapter III and Eq. (1). The MR can vary considerably as a function of  $\eta$ , the magnitude of the geometric roughness, depending on the values of  $S_\sigma$  (i.e.,  $S_M$  and  $S_m$ ) in Eq. (1). These results can be understood by examining the plots of the functions of Eq. (1), with  $S_\sigma = 1$  and  $\eta = 2\text{\AA}$  shown in Figs. 3 and 4. The electrons transmitted across an interface have the largest asymmetry in the spin-dependent scattering. As seen in Eq. (1) the transmitted portion that is not diffusely scattered, is larger when an electron experiences a small change in potential as it crosses an interface, because the factor in the exponential,

$$(k_{i\sigma} \cos\theta_i - k_{j\sigma} \cos\theta_j)^2 ,$$

is smaller. Since in  $(\text{Fe/Cr})_n$

$$|V_M| < |V_S| \approx |V_m| ,$$

the majority electrons are more likely to be diffusely scattered than the minority electrons.

When  $S_M = S_m = 1$  and  $\eta = 0$  an electron is always coherently scattered by the potential as it traverses an interface, regardless of the orientation of its spin, and the MR is zero. As  $\eta$  increases the majority-spin electrons are more likely to be diffusely

scattered than the minority-spin electrons. As shown in Fig. 2 the MR reaches its maximum value of 82.0% at  $\eta \approx 2\text{\AA}$ , which is one fifth of the spacer layer thickness and one tenth of the F layer thickness.

On the other hand, when there is a large asymmetry in the values of  $S_M$  and  $S_m$ , increasing  $\eta$  from zero lowers the MR, since the net difference in the spin-dependent scattering for the minority and the majority spins will decrease. This can be understood by noting that when  $\eta$  is zero all  $S_{j,k;l;\sigma}$  reduce to the angle independent prefactors  $S_\sigma$  of Eq. (1), as shown in Eq. (7) in chapter III. Multiplication of the plots in Figs. 3 and 4, that have  $\eta = 2\text{\AA}$  and the prefactors equal to unity, by the constants  $S_M$  and  $S_m$  where  $S_M < 1$  and/or  $S_m < 1$ , with  $S_M$  very different from  $S_m$ , leads to a smaller difference in the spin-dependent scattering for  $\eta > 0$ . This corresponding lowering of the MR with increasing  $\eta$  can be seen in two of the curves ( $S_M = 0$  and  $S_m = 1$ , and  $S_M = 1$  and  $S_m = 0.5$ ) of Fig. 2. The curve with  $S_M = 1$  and  $S_m = 0.5$  falls off more drastically with increasing  $\eta$  because the prefactors  $S_\sigma$  cause the minority spins to be more diffusely scattered while the exponential or angular dependent part in Eq. (1), shown in Figs. 3 and 4, causes the majority spins for  $(\text{Fe/Cr})_n$  to be more diffusely scattered. These two factors cause the asymmetry in the spin-dependent scattering to decrease significantly with increasing  $\eta$ . By contrast the case with  $S_M = 0$  and  $S_m = 1$  has a more gradual decrease in the MR with increasing  $\eta$ , because both the prefactors  $S_\sigma$  and the exponentials in Eq. (1) cause the minority-spin electrons to be selectively diffusely scattered so that a considerable asymmetry in the spin-dependent interfacial scattering persists.

In general, as a function of  $\eta$ , the MR undergoes the most dramatic changes from  $\eta = 0$  to  $\eta \approx 2\text{\AA}$ . For increasing  $\eta > 2\text{\AA}$  the MR falls off gradually. Shown in Figs. 5 and 6 are contour plots of the MR in the parameter space ( $S_M - S_m$ ) for  $(\text{Fe/Cr})_n$  and  $(\text{Fe/Cu})_n$  multilayers. In the region where  $S_M \approx S_m$  the MR increases as the geometric roughness  $\eta$  increases from 0 to  $2\text{\AA}$ , since the roughness leads to asymmetrical spin-dependent scattering. In the regions where  $S_M$  is very different

from  $S_m$  the MR decreases either slightly or drastically depending on whether the exponential factors and the constant prefactors  $S_M$  and  $S_m$  in Eq. (1) lead to a larger or smaller asymmetrical scattering. The region in the parameter space where the MR is the largest for an  $(\text{Fe/Cu})_n$  multilayer with  $\eta = 2 \text{ \AA}$  (see Fig. 6b) is for  $S_M > 0.75$ , and independent of  $S_m$ . By contrast, Fig. 5b for  $(\text{Fe/Cr})_n$  shows that the largest values of the MR occur in the region  $S_m > 0.65$ , independent of  $S_M$ . This difference is caused by the different values of the spacer layer potentials for Cu and Cr relative to  $V_M$  and  $V_m$  for Fe. Since in  $(\text{Fe/Cu})_n$

$$|V_M| \approx |V_S| < |V_m| ,$$

the exponential factors in Eq. (1) cause the minority electrons to be diffusely scattered more than the majority electrons. This is opposite to the case of  $(\text{Fe/Cr})_n$  mentioned above.

For interfaces with correlated (quasi-periodic) roughness, Eq. (6) in chapter III, and Eqs. (1) and (4) describe the interfacial scattering. An interface is now characterized by five parameters:  $S_M$ ,  $S_m$ ,  $\kappa$ ,  $\alpha$ , and  $\eta$ . All interfaces in a given multilayer are taken to have the same characteristics; the subscript  $ij$  can be dropped from  $\kappa_{ij}$ . Calculations with  $\kappa$  in the range of values satisfying the Bragg condition, *i.e.*,  $\kappa \leq 2k_{\max,\sigma}$ , where the values of  $k_{\max,\sigma}$  depend on the composition of the multilayer, reveal that there are regions of the parameter space  $S_M$ ,  $S_m$ ,  $\kappa$ , and  $\eta$  where the MR for  $(\text{Fe/Cr})_n$  and  $(\text{Fe/Cu})_n$  increases with increasing  $\alpha$ .

- [1] For  $(\text{Fe/Cr})_n$  there are two overlapping regions, called (a) and (b), where the MR increases sharply with increasing  $\alpha$ . Increases in the MR,  $\Delta \equiv \text{MR}(\alpha = 1) - \text{MR}(\alpha = 0)$ , as large as 61.0% were found.
- [2] For  $(\text{Fe/Cu})_n$  there is one region, called (c), where the MR increases by moderate amounts. The maximum value of  $\Delta$  is less than 13.5 %.

Note that as a function of  $\alpha$ , the changes in the MR are always monotonic, in either an abrupt or a gradual manner. In each region there is a set of parameters for which

the MR increases the most: in region (a) it is  $S_M = S_m = 1$ ,  $\kappa = 4.91 \text{ \AA}^{-1}$ , and  $\eta = 0 \text{ \AA}$ ; in region (b)  $S_M = 1$ ,  $S_m = 0$ , and  $\kappa = 5.40 \text{ \AA}^{-1}$ , and  $\eta = 0 \text{ \AA}$ ; and in region (c)  $S_M = S_m = 1$ ,  $\kappa = 5.92 \text{ \AA}^{-1}$  and  $\eta = 2.0 \text{ \AA}$ . In all these cases  $d_F = 20 \text{ \AA}$ ,  $d_S = 10 \text{ \AA}$ , and  $\tau_M = \tau_m = \tau_S = 5 \times 10^{-13}$  sec. The reasons for the increase in the MR for these values of the parameters reveal both why the MR increases in these regions and why there is such a marked difference in the magnitude of  $\Delta$  between  $(\text{Fe/Cr})_n$  and  $(\text{Fe/Cu})_n$ .

For  $S_M = S_m = 1$ ,  $\kappa = 4.91 \text{ \AA}^{-1}$ , and  $\eta = 0 \text{ \AA}$  in region (a) the MR is zero when  $\alpha = 0$  and 61.0% when  $\alpha = 1$ . At  $\kappa = 4.91 \text{ \AA}^{-1}$ , which is identically equal to  $(k_{F;m} + k_{max,m})$ , the Bragg condition, Eq. (4), is not satisfied by the minority-spin electrons for any angle of incidence on an interface from an F layer to a spacer layer. Since in addition  $S_m = 1$ , the minority-spin electrons are coherently scattered by the potential on approaching an interface from an F layer. The majority-spin electrons reaching an interface from an F layer with an angle of incidence greater than

$$\theta = \sin^{-1} \left[ \frac{4.91 \text{ \AA}^{-1} - k_{max,M}}{k_{F;M}} \right] = 41.4^\circ$$

have a probability  $\alpha$  of being diffusely scattered. The asymmetry in the spin-dependent interfacial scattering is the largest when  $\kappa = 4.91 \text{ \AA}^{-1}$ ,  $\alpha = 1$  and so is the MR.

The point in region (b) with  $S_M = 1$ ,  $S_m = 0$ ,  $\kappa = 5.40 \text{ \AA}^{-1}$ , and  $\eta = 0 \text{ \AA}$  has a MR of 41.1% when  $\alpha = 0$  and 90.9% when  $\alpha = 1$ . The current distribution in the plane of the layers for  $\alpha = 0$  and  $\alpha = 1$  is shown in Fig. 7. When  $\alpha = 0$  the current is largest in the F layers for the spin component in the potential  $V_M$ . On the other hand, when  $\alpha = 1$  the current of the same spin component in the F layer is considerably reduced. This reduction, which leads to the large increase in MR, can be understood by considering the majority electrons in the F layer incident on an interface. Since  $V_M < V_S$  in  $(\text{Fe/Cr})_n$  there is a critical angle of incidence  $\theta_{c;M}$  such that for larger angles  $R_{F,S;M}$  and  $T_{F,S;M}$  in Eq. (6) in chapter III are one and zero respectively. The

critical angle determined from Eqs. (7) and (8) in chapter III is  $\theta_{c;M} = 56.9^\circ$ . At  $\kappa = 5.40 \text{ \AA}^{-1}$ , where the MR is found to increase the most with increasing  $\alpha$ ,

$$\theta_{c;M} = \sin^{-1} \left[ \frac{5.40 \text{ \AA}^{-1} - k_{max;M}}{k_{F;M}} \right].$$

Since  $S_M = 1$ , an electron with  $\theta_{F;S;M} > \theta_{c;M}$  is totally internally reflected with probability  $(1 - \alpha)$  and diffusely scattered at the interface with probability  $\alpha$ . Therefore, increasing  $\alpha$  decreases the amount of current in the F layers for the majority spins both when the magnetic moments of the F layers are in parallel and in antiparallel configurations. The electrons with  $\theta_{F;S;M} < \theta_{c;M}$  have a nonzero probability  $T_{F;S;M}$  of being transmitted into the spacer layer. When the magnetic moments of the F layers are parallel these electrons are not diffusely scattered at any interface, but are always diffusely scattered at alternating interfaces when the F layers are antiparallel, since  $S_m = 0$ . In short increasing  $\alpha$  removes the portion of electrons in the F layers that are totally internally reflected, *i.e.*, channeled. These electrons make an equal contribution to the conductivity for the F layers in parallel  $\sigma_{\uparrow\uparrow}$  and in antiparallel  $\sigma_{\uparrow\downarrow}$  configurations. By removing this equal contribution the remaining unequal contributions to the conductivities in Eq. (7) in chapter III, mainly arising from  $S_m = 0$ , become more pronounced, causing an increase in the MR.

At the point  $S_M = S_m = 1$ ,  $\kappa = 5.92 \text{ \AA}^{-1}$  and  $\eta = 2.0 \text{ \AA}$  in region (c) for  $(\text{Fe/Cu})_n$ , the MR increases from 48.2 % to 61.5 % as  $\alpha$  increases from 0 to 1. The increase is the result of the interplay between the scattering caused by geometric roughness, Eq. (1), and the quasi-periodic roughness, Eq. (4), which tend to produce the largest spin-dependent asymmetry for those electrons near normal incidence and grazing incidence, respectively.

In contrast to  $(\text{Fe/Cr})_n$ , where there are two substantial regions, (a) and (b), in parameter space where  $\Delta$  is large, in  $(\text{Fe/Cu})_n$  there is only a small region (c) where the MR increases moderately with increasing  $\alpha$ . The reason is that  $V_S < V_M$ . To illustrate this point I discuss two sets of values of the parameters for  $(\text{Fe/Cu})_n$  that are

analogous to those analyzed for  $(\text{Fe/Cr})_n$  in regions (a) and (b). If I consider the MR as a function of  $\alpha$  for different values of  $\kappa$  with  $S_M = S_m = 1$  and  $\eta = 0$ , similar to the point considered in region (a) for  $(\text{Fe/Cr})_n$ , I find no value of  $\kappa$  such that only one spin component is selectively diffusely scattered at an interface. For instance if  $\kappa$  is chosen so as to maximize the interfacial diffuse scattering of the majority-spin electrons from the Fe layer without affecting the minority-spin electrons, the electrons in the Cu spacer layer impinging on an interface are still diffusely scattered because  $k_s > k_{F,M}$  at the Fermi energy. This lack of asymmetry in the total spin-dependent scattering at the interfaces prevents the MR from increasing as a function of  $\alpha$ . When  $\alpha = 0$  the point in parameter space with  $S_M = 1$ ,  $S_m = 0$ , and  $\eta = 0$ , similar to the point considered in region (b) for  $(\text{Fe/Cr})_n$ , has a larger contribution to the current in the Cu layers than in the Fe layers. The larger current in the Cu layer occurs only when the magnetic moments of the F layers are parallel and only for the spin component that experiences the potential  $V_M$  in the F layers. The larger current is caused by channeled electrons in the Cu layers that are non-diffusively scattered, since  $S_M = 1$ , and totally internally reflected for angles of incidence greater than a critical angle, since  $V_S < V_M$ . This channeled current leads to a larger MR since it contributes to  $\sigma_{\uparrow\uparrow}$  but not to  $\sigma_{\uparrow\downarrow}$ . For  $\kappa$  in a range of values that destroys this channeled current the MR will decrease with increasing  $\alpha$ , unlike the increase that occurs in  $(\text{Fe/Cr})_n$ , since the channeling that is destroyed there occurs in the F layers when the magnetic moments are both parallel and antiparallel.

#### D. Conclusions

In studying the influence of interface scattering on the negative magnetoresistance of ferromagnetic-normal metal multilayers, three aspects have been considered: (1) random geometric roughness described by  $\eta$ , the mean square deviation of the interfaces from being atomically flat; (2) correlated (quasi-periodic) roughness, characterized by the dominant  $k$ -vector of the coherence,  $\kappa$ , and the scattering strength  $\alpha$ ;

and (3) averaged effects due to impurities, interdiffusion, band structure, etc. The last effect has been included in a simple way using the parameters  $S_M$  and  $S_m$ . Geometric uncorrelated roughness scatters electrons at normal incidence more efficiently, while the correlated (quasi-periodic) roughness has its greatest effect on electrons at grazing angles. These different properties of the interfaces can combine to produce either a large or a small asymmetry in the spin-dependent interfacial scattering. A giant MR results whenever the spin asymmetry is large. Further experimental and theoretical investigations are needed to ascertain which properties of the interfaces are realized during particular instances of fabrication of multilayers by means of various techniques.



## E. References for Chapter IV

- 1 K. Fuchs, Proc. Cambridge Philos. Soc., **34**, 100 (1938).
- 2 E. H. Sondheimer, Adv. Phys., **1**, 1 (1952).
- 3 R. E. Camley and J. Barnaś, Phys. Rev. Lett. **63**, 664 (1989).
- 4 J. Barnaś, A. Fuss, R. E. Camley, P. Grünberg, and W. Zinn, Phys. Rev. B **42**, 8110 (1990).
- 5 E. C. Stoner, Proc. Roy. Soc. London A, **165**, 372 (1938).
- 6 S. B. Soffer, J. Appl. Phys. **38**, 1710 (1967).
- 7 V. Bezák and J. Krempaský, Czech. J. Phys. B **18**, 1264 (1968).
- 8 V. Bezák, M. Kedro, and A. Pevala, Thin Solid Films **23**, 305 (1974).
- 9 P. Beckmann and A. Spizzichino, *The Scattering of Electromagnetic Waves from Rough Surfaces*, (Pergamon, Oxford, 1963) pp. 70 - 98.
- 10 It should be noted that the derivation of the equations in Refs. 6-9 require a correlation length longer than the electron Fermi wavelength, so that a vector normal to the surface can be properly defined. In this sense the limit  $L \rightarrow 0$  is not strictly valid. It should be understood as the limit in which  $L$  is still longer than the Fermi wavelength but shorter than all other lengths in the problem.
- 11 If the geometric random roughness of the interfaces were the only source of scattering, the prefactors in Eq. (1) must all be taken to be  $S_{\sigma} = 1$ . This is, however, not a realistic assumption. Impurities and other defects at the interfaces scatter electrons of opposite spin in a different way. Hence  $S_M$  and  $S_m$  are not equal, and in general both less than one.
- 12 It should be emphasized that "roughness" with a single, given periodicity, produces Bragg beams with well defined directions of propagation, *i.e.*, electron trajectories with their own (positive or negative) contribution to the current. For a smooth, non-uniform, quasi-periodic distribution of geometrical defects at the

interface (*i.e.*, a Fourier transform of the topography consisting of a peaked but continuous function), the distribution of velocities of electrons Bragg-scattered over the Fermi surface tends to average down to zero, resulting in the electrons being effectively removed from the current-carrying distribution, *i.e.*, relaxing back to equilibrium.

- <sup>13</sup> As in Eq. (7) in chapter III, the masses  $m_{i\sigma}$  and  $m_{j\sigma}$  in Eq. (2) are assumed to be equal. All calculations presented in the paper have  $m_{i\sigma} = m$ , independent of the layer  $i$  and the spin  $\sigma$ .

## F. Figures for Chapter IV

### Figure 1

Illustration of the Bragg condition in reciprocal space for a periodically modulated interface with a minimum nonzero reciprocal lattice vector  $\kappa_{ij}$  viewed from two different perspectives and for two different cases: on the left side  $V_{i\sigma} < V_{j\sigma}$ ; and on the right side  $V_{i\sigma} > V_{j\sigma}$ . The perspectives at the top of the figure are in the plane of the interface; the "Bragg rods" are out of the page. Hemispheres of  $\mathbf{k}$ -vectors for the two films at the interface, corresponding to an incident  $\mathbf{k}_{i\sigma}$ , labeled I, with the angle of incident  $\theta$  are shown. The solid vectors labeled R and T are the reflected and transmitted beams, respectively. The angle  $\theta$  was chosen in each case to equal the threshold angle. A single grazing-angle additional diffraction peak occurs either in back-scattering (left) or in forward-scattering (right). The corresponding  $\mathbf{k}$ -vectors are shown (dotted vectors), and labeled D in the figure.

### Figure 2

Variation of  $(\Delta\rho/\rho)$  as a function of  $\eta$ , the magnitude of the geometric roughness, for an  $(\text{Fe/Cr})_n$  multilayer with interfacial scattering described by Eq. (6) in chapter III and Eq. (1). The parameters are  $d_F = 20 \text{ \AA}$ ,  $d_S = 10 \text{ \AA}$ , and  $\tau_M = \tau_m = \tau_S = 5 \times 10^{-13} \text{ sec}$ , with four different values of  $S_M$  and  $S_m$ : (1) chain-dashed curve  $S_M = 0$  and  $S_m = 1$ ; (2) solid curve  $S_M = S_m = 1$ ; (3) dashed curve  $S_M = 1$  and  $S_m = 0.5$ ; and (4) chain-dotted curve  $S_M = S_m = 0.5$ .

### Figure 3

Variation of  $S_{F,S;i;\sigma}$ , from Eq. (1), as a function of  $\theta$ , the angle of incidence, with  $S_\sigma = 1$  and  $\eta = 2 \text{ \AA}$  for an  $(\text{Fe/Cr})_n$  multilayer, with four different values of  $i$  and  $\sigma$ : (1) dashed curve  $i = S$  and  $\sigma = m$ ; (2) solid curve  $i = S$  and  $\sigma = M$ ; (3) chain-dashed curve  $i = F$  and  $\sigma = m$ ; and (4) dotted curve  $i = F$  and  $\sigma = M$ . Note that  $S_{F,S;S;M}$  is zero for  $\theta$  greater than the critical angle of incidence; the angle at which  $T_{F,S;M}$  goes to zero.

**Figure 4**

Variation of  $S_{S,F;i;\sigma}$ , from Eq. (1), as a function of  $\theta$ , the angle of incidence, with  $S_\sigma = 1$  and  $\eta = 2 \text{ \AA}$  for an  $(\text{Fe/Cr})_n$  multilayer, with four different values of  $i$  and  $\sigma$ : (1) dashed curve  $i = F$  and  $\sigma = m$ ; (2) solid curve  $i = F$  and  $\sigma = M$ ; (3) chain-dashed curve  $i = S$  and  $\sigma = m$ ; and (4) dotted curve  $i = S$  and  $\sigma = M$ . Note that the chain-dashed curve and dotted curve overlap.

**Figure 5**

Contour plots of  $\Delta\rho/\rho$  in the parameter space  $S_m$  and  $S_M$  for an  $(\text{Fe/Cr})_n$  multilayer with  $d_F = 20 \text{ \AA}$ ,  $d_S = 10 \text{ \AA}$ ,  $\tau_M = \tau_m = \tau_S = 5.0 \times 10^{-13} \text{ sec}$ . The electron scattering at the interfaces is described by Eq. (6) in chapter III and Eq. (1). In (a)  $\eta = 0$  and in (b)  $\eta = 2 \text{ \AA}$

**Figure 6**

Contour plots of  $\Delta\rho/\rho$  in the parameter space  $S_m$  and  $S_M$  for an  $(\text{Fe/Cu})_n$  multilayer with  $d_F = 20 \text{ \AA}$ ,  $d_S = 10 \text{ \AA}$ ,  $\tau_M = \tau_m = \tau_S = 5.0 \times 10^{-13} \text{ sec}$ . The scattering at the interfaces is described by Eq. (6) in chapter III and Eq. (1). In (a)  $\eta = 0$  and in (b)  $\eta = 2 \text{ \AA}$

**Figure 7**

Diagrams of the potentials and the calculated in-plane current  $J_x(z)$  for the  $\uparrow$ -spin and  $\downarrow$ -spin electrons in the parallel ( $\uparrow\uparrow$ ) and in the antiparallel ( $\uparrow\downarrow$ ) configurations of an  $(\text{Fe/Cr})_n$  multilayer in which three of the layers are shown. The scattering at the interfaces is described by Eq. (6) in chapter III, and Eqs. (1) and (4) where  $S_M = 1$ ,  $S_m = 0$ ,  $\eta = 0$ , and  $\kappa = 5.404 \text{ \AA}^{-1}$ , with two different values of  $\alpha$ : (1) dashed curve  $\alpha = 0$ ; and (2) chain-dotted curve  $\alpha = 1$ . The other parameters are  $d_F = 20 \text{ \AA}$ ,  $d_S = 10 \text{ \AA}$ , and  $\tau_M = \tau_m = \tau_S = 5.0 \times 10^{-13} \text{ sec}$ .

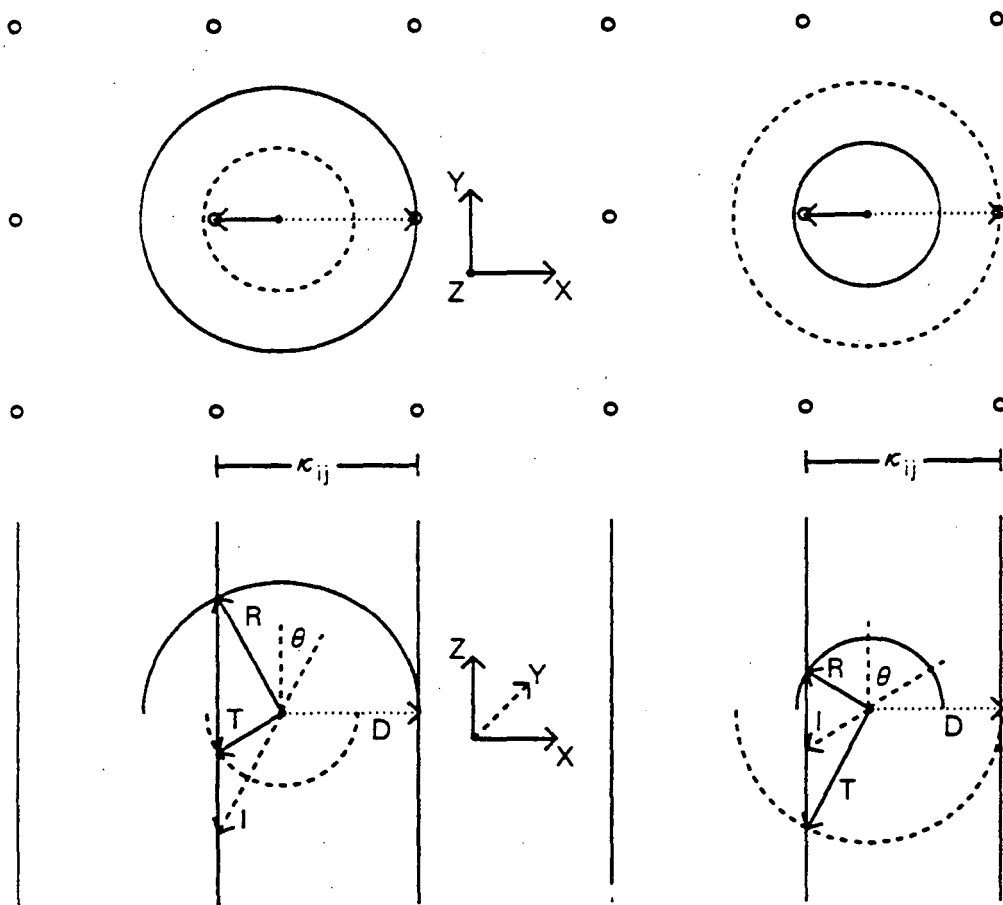


Fig. 1

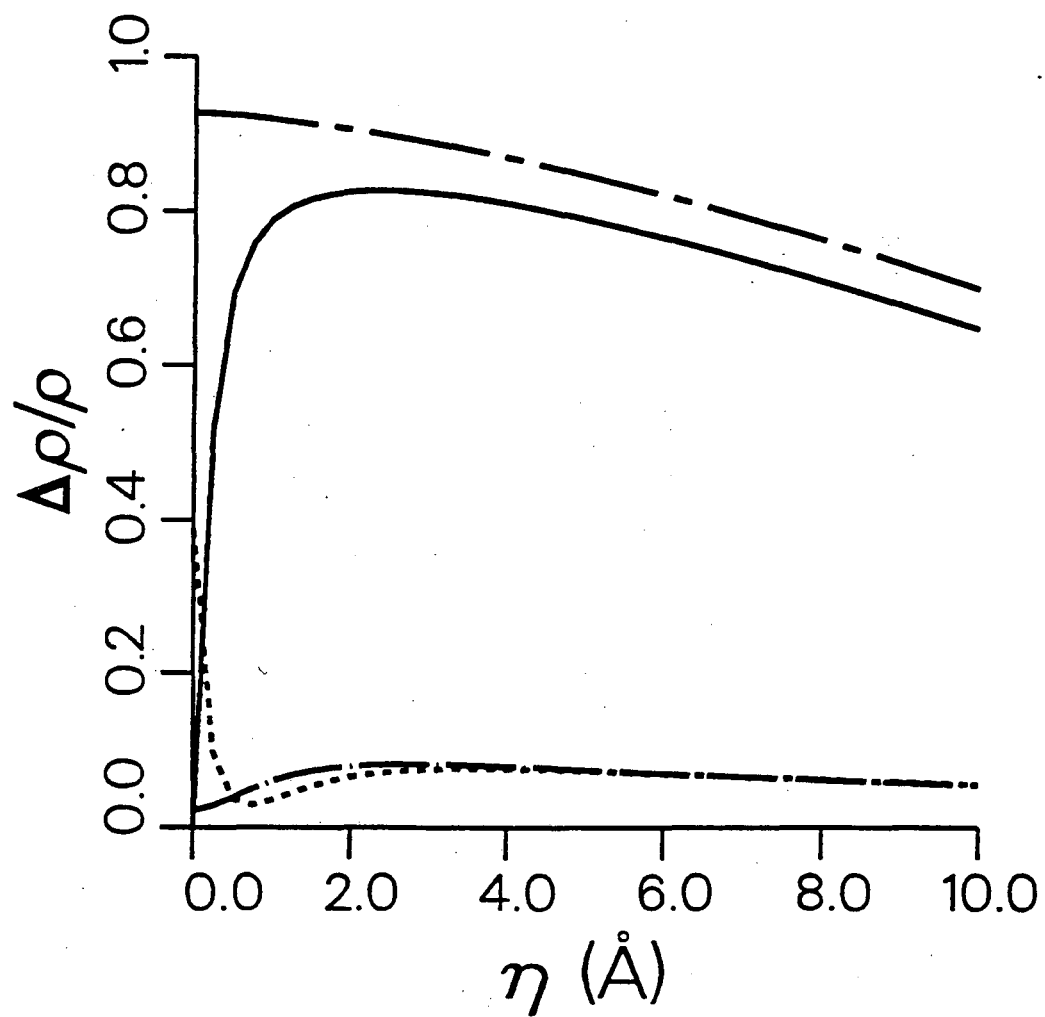


Fig. 2

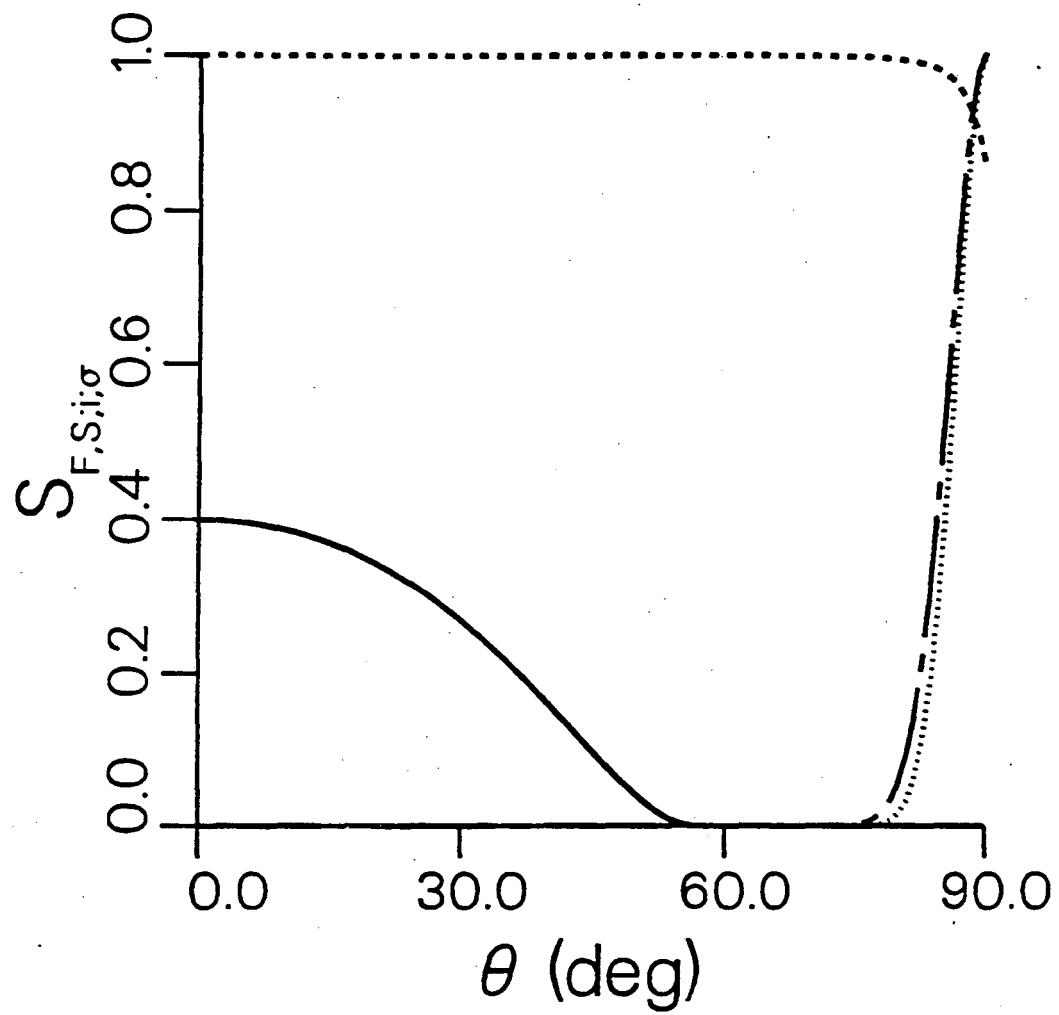


Fig. 3

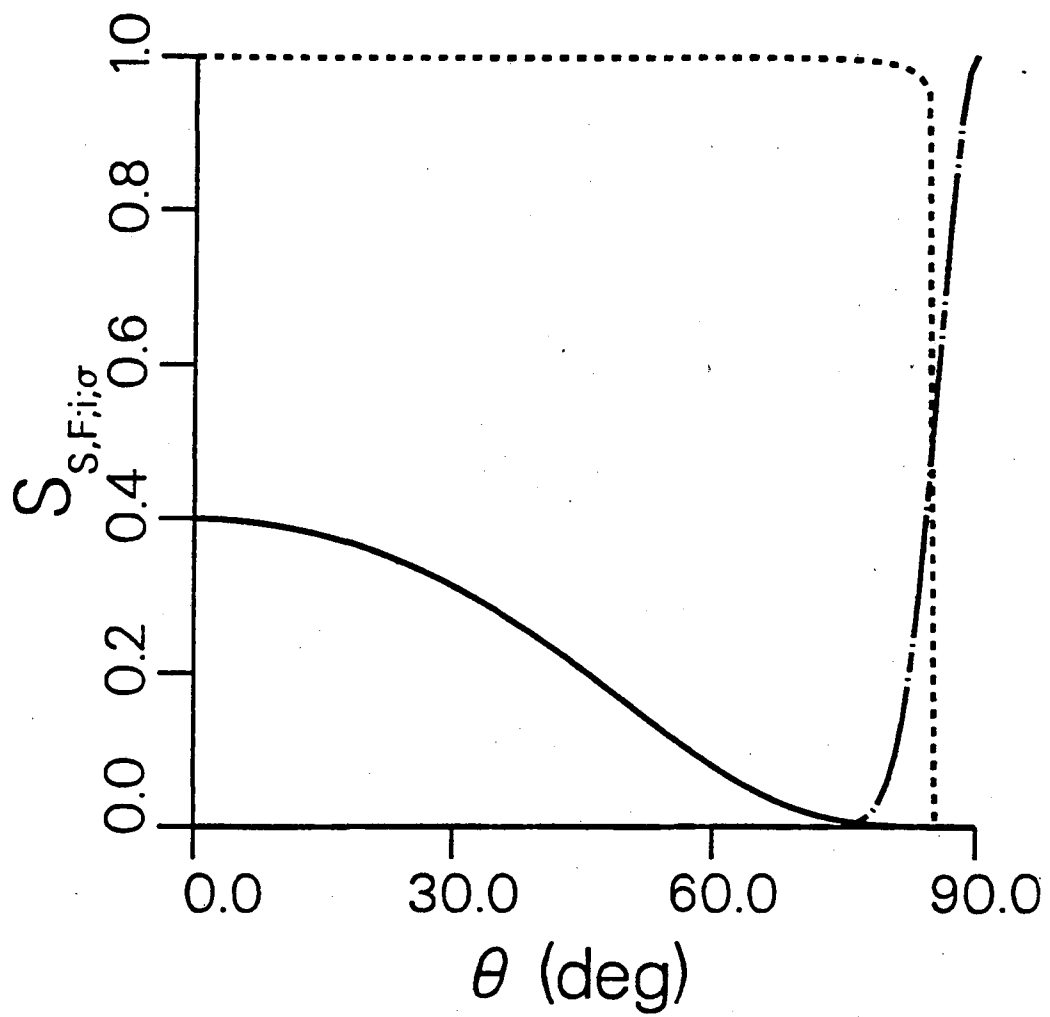


Fig. 4



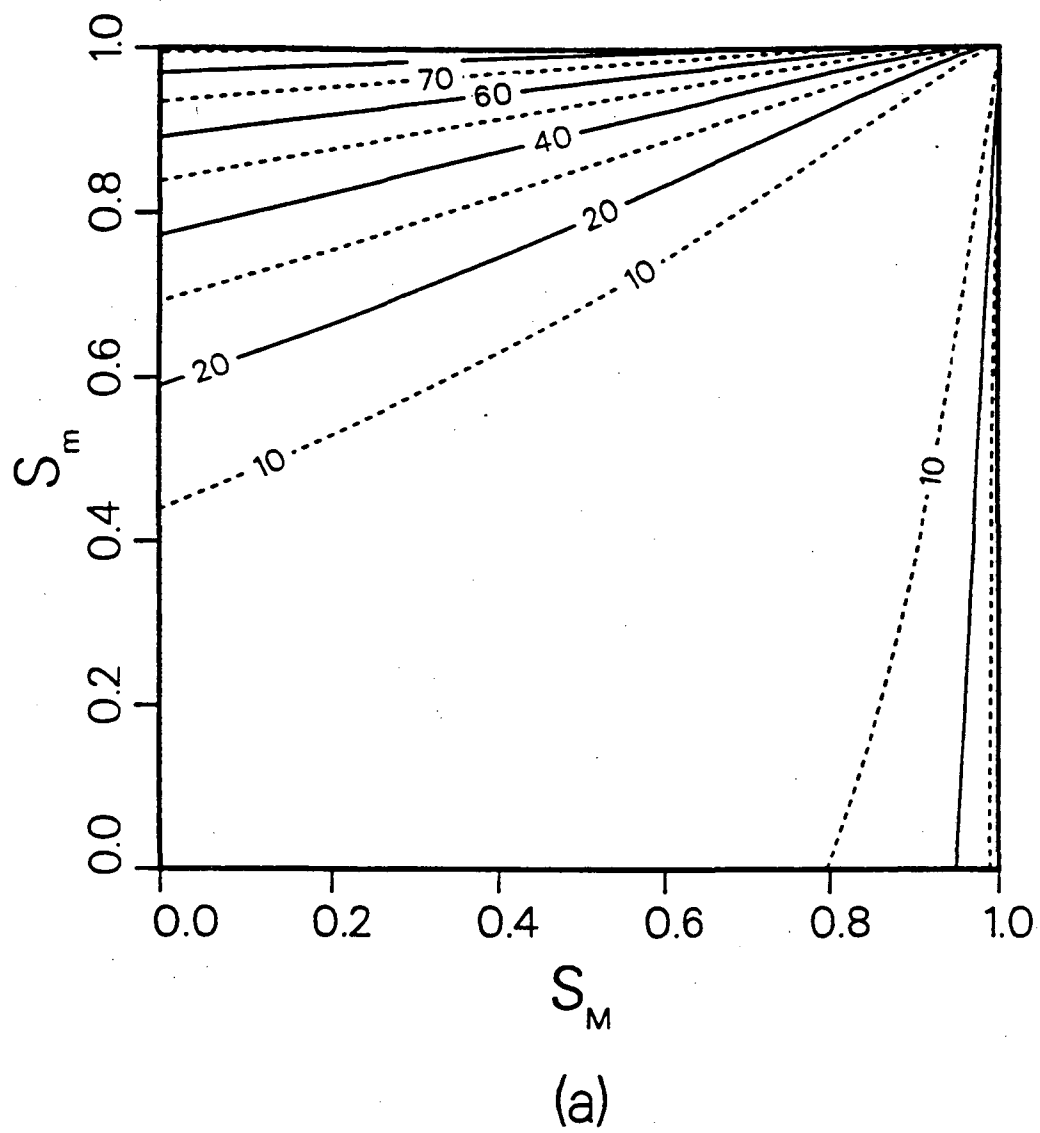


Fig. 5

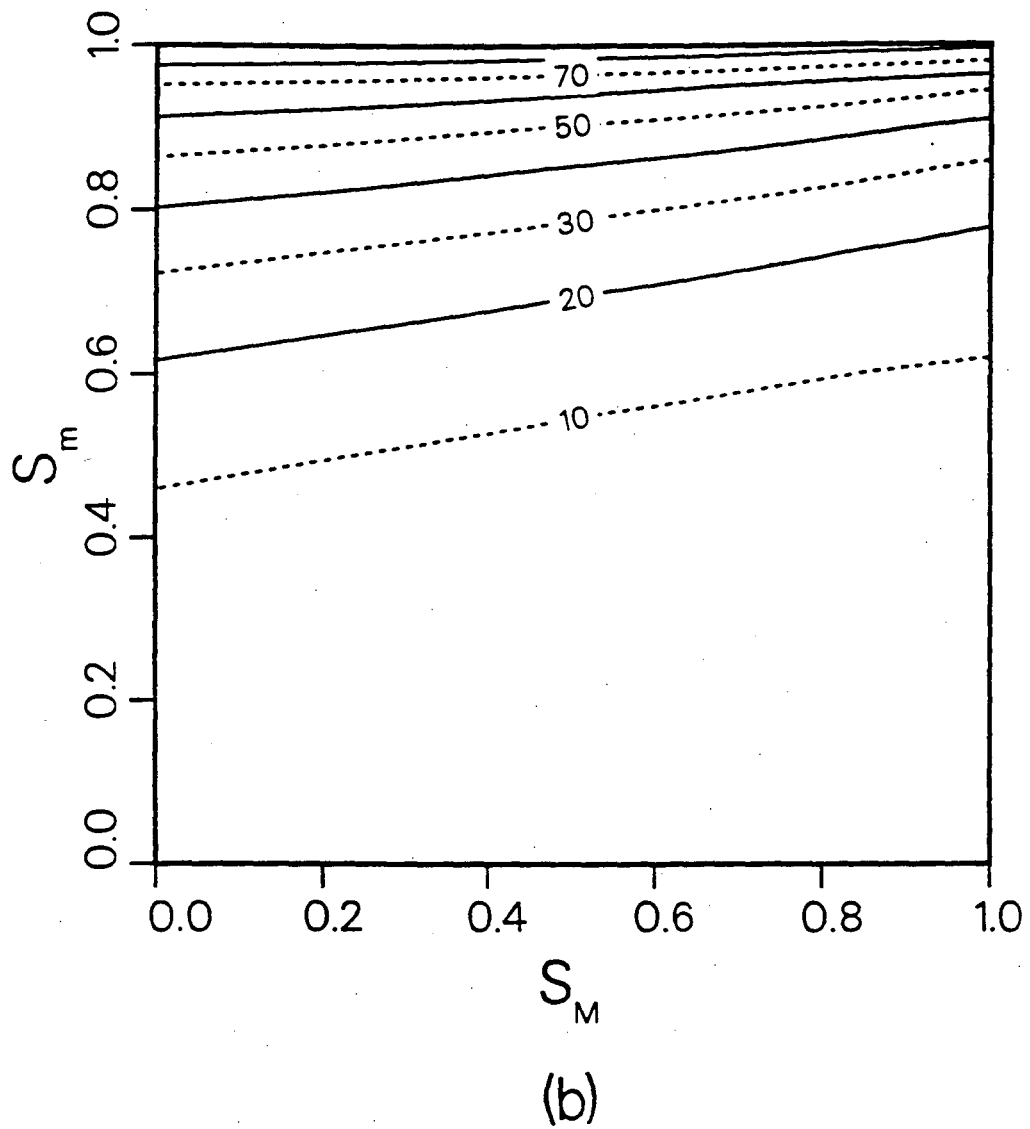


Fig. 5

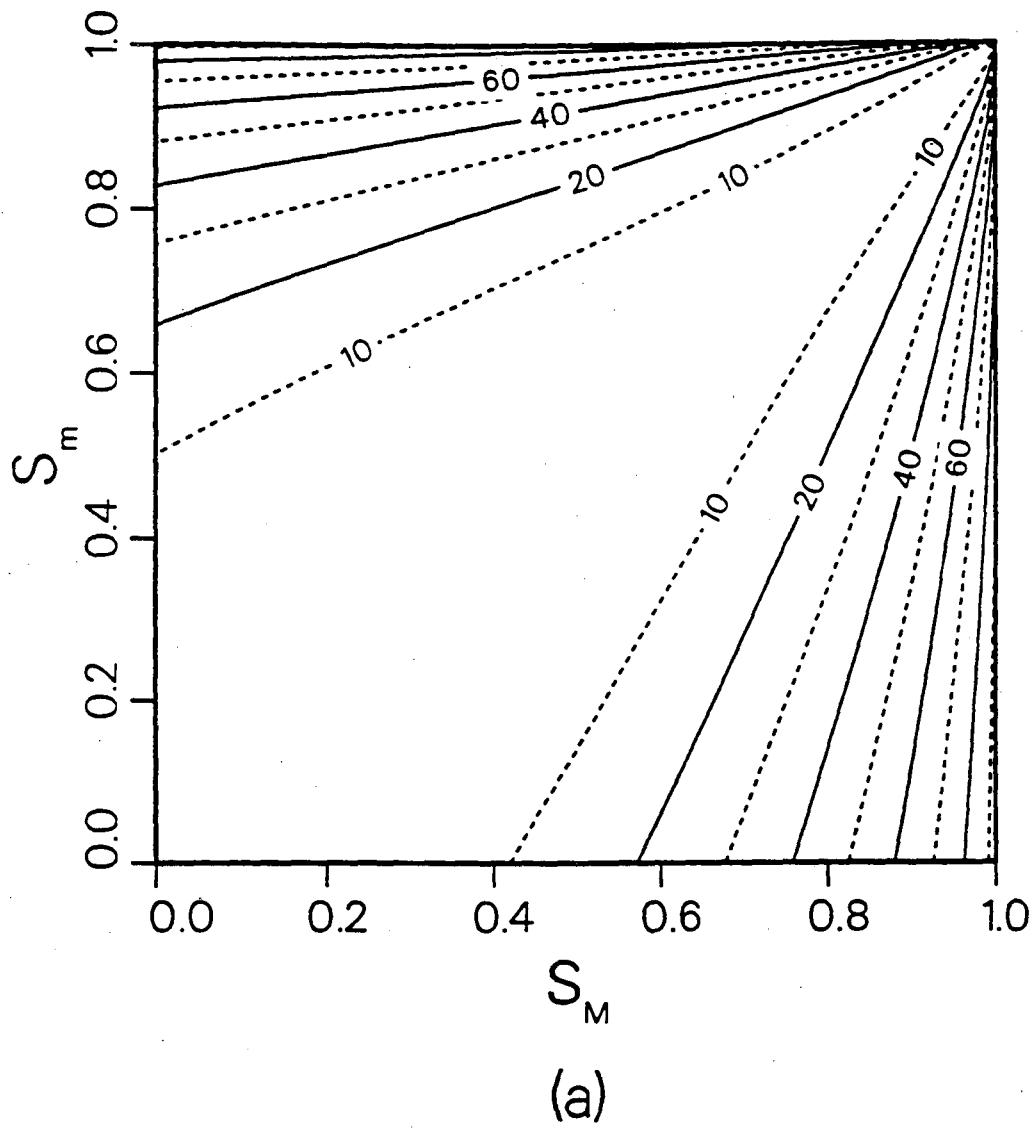
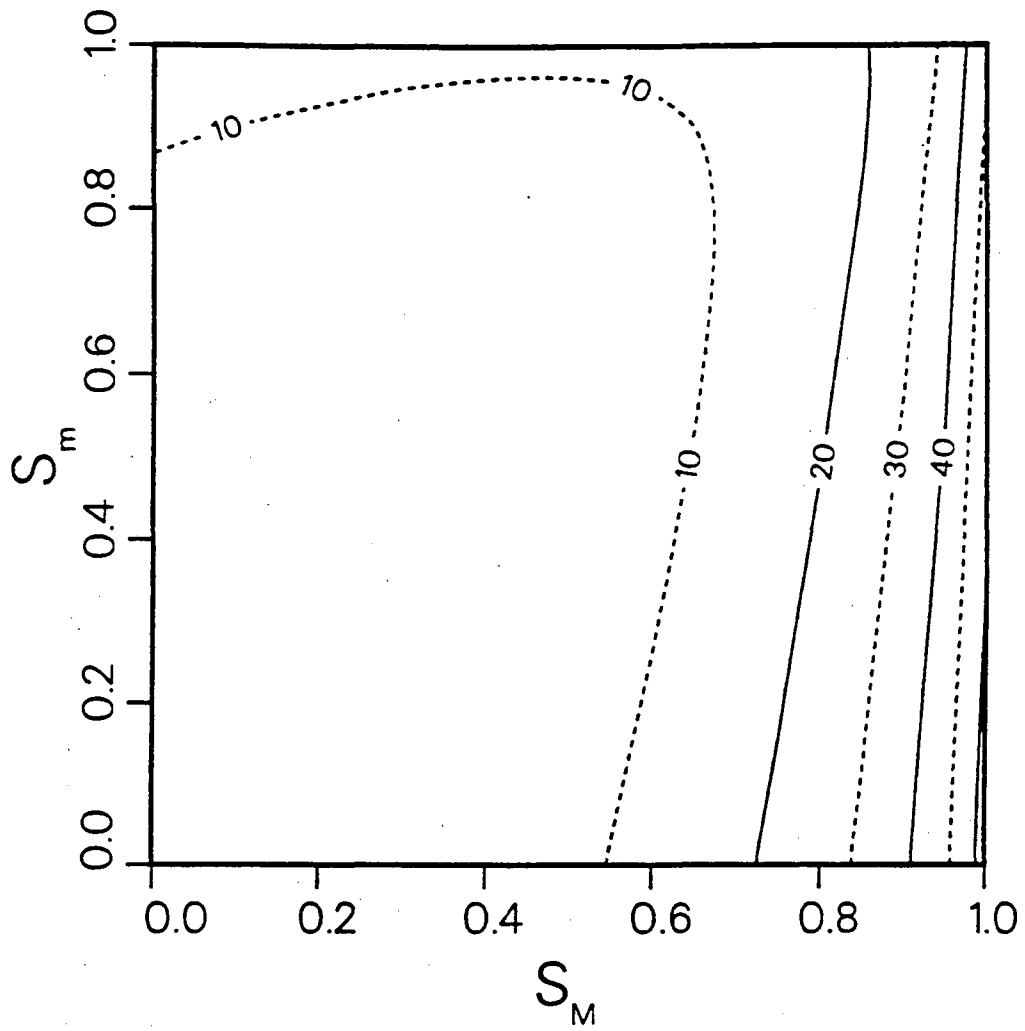


Fig. 6



(b)

Fig. 6

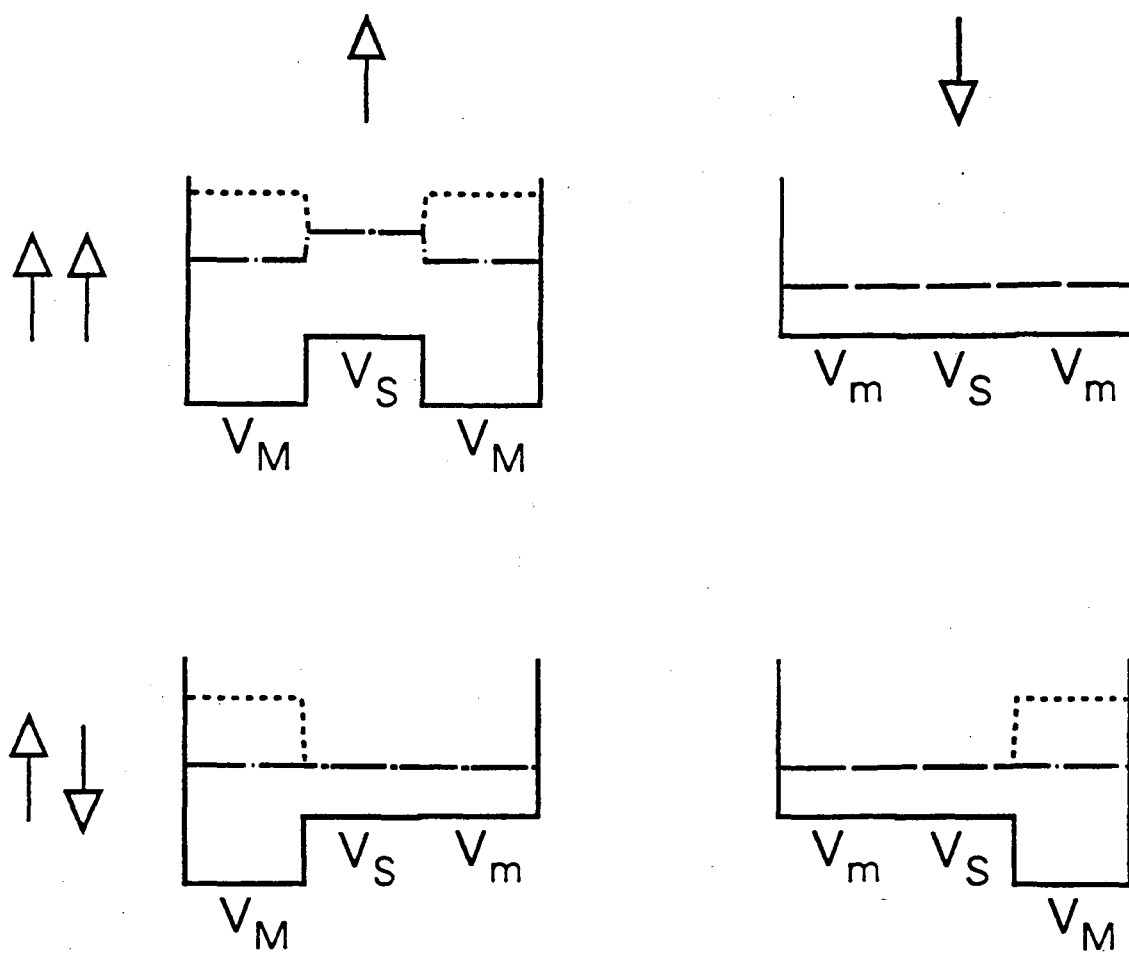


Fig. 7

LAWRENCE BERKELEY LABORATORY  
UNIVERSITY OF CALIFORNIA  
TECHNICAL INFORMATION DEPARTMENT  
BERKELEY, CALIFORNIA 94720

AAS992



LBL Libraries